# Computational Investigation of Solvation Phenomena at Metal-Electrolyte Interfaces

Oskar Cheong

JÜLICH
Forschungszentrum

# Computational Investigation of Solvation Phenomena at Metal-Electrolyte Interfaces

Oskar Cheong

# Abstract

The interplay between metal catalyst surfaces and its surrounding solvent environment has a considerable impact on interfacial electrochemical processes, affecting both activity and selectivity of electrochemical reactions, e.g., the carbon dioxide ($CO_2$) reduction reaction. While atomistic simulations are useful to gain advanced insight into the metal-electrolyte interface, many challenging problems exist for a realistic, computational description of the complex electrochemical interface. Especially, a computationally feasible scheme for description of solvation effects at the metal-electrolyte interface has yet to be established.

This thesis explores several computational improvements that enable accounting for solvation effects when modelling a metal-electrolyte interface. The first part of the thesis focuses on testing the ability of a classical molecular dynamics (CMD) simulation approach based on the interface force field (IFF) to efficiently model water structures on metal surfaces, using the lead (Pb) surface as a test case. While *ab initio* molecular dynamics (AIMD) calculations are considered to be more accurate than CMD calculations, the latter allows for exploration of much longer time- and length-scales, which results in better equilibrated water structures. This work demonstrates the potential of using IFF-based CMD simulations for statistically complete sampling water structures on metal surfaces. In the second part of the thesis the impact of different solvation models on the $CO_2$ reduction reaction on both silver (Ag) and lead (Pb) catalysts towards formic acid (HCOOH) and carbon monoxide (CO) products are investigated. The systematic analysis indicates that accounting for explicit solvation has a crucial impact on the $CO_2$ reduction reaction, correctly predicting primary products on both metal catalysts, which was not achieved by simplified computation assuming vacuum environment. Furthermore, the performance of implicit, explicit and hybrid solvation schemes are discussed in that subproject. Another problem investigated in this thesis is to account for solvation entropy effects on surface

chemical reactions. In that context, the Two Phase Thermodynamic (2PT) model is applied and tested to evaluate solute entropy effects in bulk solvent and at the metal-electrolyte interface. Since entropy contributions to Gibbs energies of chemical reactions at the metal-solvent interface are usually either neglected or modeled using the ideal gas approximation, solvent effects on the reaction free energies are often insufficiently or incorrectly accounted for. The 2PT method offers a solution to obtain computationally efficient and accurate estimates of solvent entropy effects, resulting in a more realistic description of chemical reactions at metal-electrolyte interfaces.

The presented research aims to pave the way towards efficient computation of electrochemical interfaces under realistic conditions, which is an essential ability in the context of accelerating computer-aided design of novel and efficient electrocatalysts.

# Kurzfassung

Die Wechselwirkungen zwischen Metallkatalysatoroberflächen und der umliegenden Lösungsmittelumgebung haben erhebliche Auswirkungen auf elektrochemische Prozesse an der Grenzfläche und beeinflussen sowohl die Aktivität als auch die Selektivität elektrochemischer Reaktionen, wie z. B. bei der $CO_2$-Reduktion. Während atomistische Simulationen nützlich sind, um einen tieferen Einblick in die Metall-Elektrolyt-Grenzfläche zu gewinnen, herrschen zurzeit noch viele Herausforderungen für eine realistische, rechnergestützte Beschreibung der komplexen elektrochemischen Grenzfläche. Insbesondere muss noch ein rechnerisch effizientes Schema zur Beschreibung von Lösungsmitteleffekten an der Metall-Elektrolyt-Grenzfläche entwickelt werden. In dieser Arbeit werden mehrere atomistische Modellierungsmethoden untersucht, die es ermöglichen, Lösungsmitteleffekte bei der Modellierung einer Metall-Elektrolyt-Grenzfläche zu berücksichtigen. Der erste Teil der Arbeit konzentriert sich auf die effiziente Anwendbarkeit der klassischen Molekulardynamik (CMD) Simulation für Wasserstrukturen auf Metalloberflächen mithilfe des interface force field (IFF) Kraftfelds, wobei die Oberfläche von Blei (Pb) als Testfall dient. Ab-Initio Molekulardynamik (AIMD)-Berechnungen sind grundsätzlich akkurater als CMD-Berechnungen, letztere ermöglichen jedoch die Erforschung von viel längeren Zeit- und Längenskalen, was zur besseren Equilibrierung der Wasserstrukturen führt. Diese Arbeit demonstriert das Potenzial von IFF-basierten CMD-Simulationen für Wasserstrukturen auf Metalloberflächen. Im zweiten Teil der Arbeit werden die Auswirkungen verschiedener Wassermodelle auf die $CO_2$-Reduktion an Silber (Ag) und Blei (Pb) Katalysatoren zu Ameisensäure (HCOOH) und Kohlenmonoxid (CO) untersucht. Die systematische Analyse zeigt, dass die Berücksichtigung von expliziten Wassermolekülen einen entscheidenden Einfluss auf die $CO_2$-Reduktion hat und die Primärprodukte an beiden Metallkatalysatoren korrekt vorhergesagt werden können, im Gegensatz zur vereinfachten Annahme einer Vakuumumgebung. Darüber hin-

aus wurden die verschiedenen Wassermodelle (implizit, explizit und hybrid) untereinander verglichen und analysiert. Eine weitere Herausforderung, welche in dieser Arbeit untersucht wird, ist die Berücksichtigung von Lösungsmittelentropieeffekten auf Oberflächenreaktionen. In diesem Zusammenhang wird das Zwei-Phasen-Thermodynamik-Modell (2PT) angewandt und getestet, um die Entropieeffekte an der Metall-Elektrolyt-Grenzfläche zu bewerten. Da Entropiebeiträge zur Berechnung von Gibbs-Energien für chemische Reaktionen an der Metall-Lösungsmittel-Grenzfläche in der Regel entweder vernachlässigt oder mit Hilfe des idealen Gasgesetzes modelliert werden, werden Lösungsmitteleffekte für die Berechnung von Gibbs-Energien häufig unzureichend oder falsch berücksichtigt. Die 2PT-Methode bietet eine Lösung für eine rechnerisch effiziente und genaue Schätzung der Lösungsmittelentropieeffekte, was zu einer realistischeren Beschreibung der chemischen Reaktionen an Metall-Elektrolyt-Grenzflächen führt. Die präsentierte Abschlussarbeit soll den Weg zu einer effizienteren und akkurateren Berechnung elektrochemischer Grenzflächen ebnen, um die Forschung und Entwicklung von neuartigen und effizienten Elektrokatalysatoren mithilfe atomistischer Simulationen zu beschleunigen.

# Acknowledgements

The success of this dissertation was made possible by the invaluable contributions of numerous individuals. I acknowledge that without substantial support I got from different parties, especially in the challenging times of the pandemic, this thesis would not have been achievable.

First, I would like to thank Prof. Michael Eikerling, the director of IEK-13 institute for giving me the opportunity to perform the dissertation research at Forschungszentrum Jülich, serving as "Doktorvater" and providing scientific advice through the time of the studies, crucial support, encouragement, motivation and trust, which was essential for conduction of this dissertation studies. It is not very common that institute directors are available 24/7, which I really do appreciate. Equally, I would like to acknowledge the substantial time and effort of my direct supervisor, Dr. Piotr Kowalski, head of the Computational Materials Modeling division (CMM) at IEK-13, who provided day-to-day supervision, guided me through the last three years, teaching the art of scientific research, introducing the art of scientific networking and helping with shaping scientific papers, conference presentations as well as this thesis. I am especially thankful for critical feedback he has given me and various opportunities for contributing to other projects, resulting in co-authorship of several papers and connection to other researcher on the campus and beyond. Professional support of the two senior researchers was key for finalization of my dissertation research.

I am especially thankful for the continuous support, help and friendship of members and associates of the CMM divison. I would like to especially thank Dr. Zhengda He for being a patient office mate and providing continuous support and advice. Many thanks to Thomas Bornhake, who as a master student in CMM division, performed joint research and contributed substantially to the research presented here. Working with him on challenging scientific projects was really an enjoyable experience.

I would like to thank all members of IEK-13 for making the research experience

# Declaration

I hereby declare in lieu of an oath that I have completed the dissertation entitled

*Computational Investigation of Solvation Phenomena at Metal-Electrolyte Interfaces*

independently and without illegitimate assistance from third parties. I have used no other than the specified sources and aids. I have complied with the principles for ensuring good scientific practice at RWTH Aachen University. The publication of the thesis does not breach any existing trade secrets.
I agree to the internal use of this thesis in the libraries of RWTH Aachen University as well as in Forschungszentrum Jülich GmbH.

# Eidesstattliche Versicherung

Ich versichere hiermit an Eides Statt, dass ich die vorliegende Dissertation mit dem Titel

*Computergestützte Untersuchung von Lösungsmitteleffekten an*
*Metall-Elektrolyt-Grenzflächen*

selbstständig und ohne unzulässige fremde Hilfe erbracht habe. Ich habe keine anderen als die angegebenen Quellen und Hilfsmittel benutzt. Die Grundsätze zur Sicherung guter wissenschaftlicher Praxis der RWTH Aachen habe ich eingehalten. Die Veröffentlichung verletzt keine bestehenden Betriebsgeheimnisse.
Mit der internen Verwendung dieser Arbeit in den Bibliotheken der RWTH Aachen sowie im Forschungszentrum Jülich GmbH bin ich einverstanden.

---

City, Date                                                                    Signature

# List of Acronyms

| Acronym | Definition |
|---------|------------|
| 2PT | Two-phase thermodynamic |
| AIMD | Ab initio molecular dynamics |
| AMBER | Assisted Model Building with Energy Refinement |
| ASE | Atomic simulation environment |
| CCS | Carbon capture and storage |
| CHARMM | Chemistry at Harvard Macromolecular Mechanics |
| CHE | Computational hydrogen electrode |
| CI-NEB | Climbing nudged elastic band |
| CMD | Classical molecular dynamics |
| CO2R | Carbon dioxide reduction |
| DFT | Density functional theory |
| DOS | Density of states |
| ESM-RISM | Effective screening medium-reference interaction site model |
| eV | Electron volt |
| GAFF | Generalized AMBER force field |
| GGA | Generalized gradient approximation |
| GTO | Gaussian type orbital |
| H-bond | Hydrogen bond |
| H-down | Hydrogen down |
| H-up | Hydrogen up |
| IFF | Interface force field |
| KBFF | Kirkwood-Buff force field |
| KS | Kohn-Sham |
| LDA | Local density approximation |

| | |
|---|---|
| LJ | Lennard-Jones |
| MEP | Minimum energy path |
| MM | Molecular mechanics |
| NEB | Nudged elastic band |
| OER | Oxygen evolution reaction |
| OPLS | Optimized Potentials for Liquid Simulations |
| PBE | Perdew-Burke-Ernzerhof |
| PCM | Polarizable continuum model |
| QM | Quantum mechanics |
| RD | Reference data |
| RDF | Radial distribution function |
| Ry | Rydberg |
| SCCS | Self-consistent continuum solvation |
| SPC | Simple point charge |
| STM | Scanning tunneling microscope |
| STO | Slater type orbital |
| TI | Thermodynamic integration |
| TraPPE | Transferable Potentials for Phase Equilibria |
| VACF | Velocity autocorrelation function |
| VASP | Vienna ab initio simulation package |
| XC | Exchange-correlation |
| ZPE | Zero-point energy |

# Contents

# Preface

This thesis is based on the computational works carried out by me between October 2019 and June 2023, with the main goal of filling out missing aspects related to the computation of solvation phenomena at metal-electrolyte interfaces. The research is highly relevant in the fields of computational and experimental electrochemistry and electrocatalysis. Due to the relevance of the research topic, several chapters are based on works that have either been published or accepted.

**Chapter 3**: **O. Cheong**, M. H. Eikerling, P. M. Kowalski, "Water structures on Pb(100) and (111) surface studied with the Interface force field", Appl. Surf. Sci. 589, 152838 (2022).

**Chapter 4**: **O. Cheong**, T. Bornhake, X. Zhu, M. H. Eikerling, "Stay hydrated! Impact of solvation phenomena on the $CO_2$ reduction reaction at Pb(100) and Ag(100) surfaces", ChemSusChem, e202300885 (2023).

**Chapter 5**: **O. Cheong**, F. Tipp, M. H. Eikerling, P. M. Kowalski, "Entropy effects on reactive processes at metal-solvent interfaces", accepted in J. Phys. Chem. C (2024).

Besides the main projects, I have also contributed to other research topics and publications conducted in the Computational Materials Modelling Division at IEK-13 and with external collaborators, which are listed in the Appendix.

Research reported in this thesis was performed in the Computational Materials Modeling division at IEK-13 institute for Theory and Computation of Energy Materials (Head: Prof. Michael Eikerling) at Forschungszentrum Jülich GmbH, under direct supervision of division's leader, Dr. Piotr Kowalski. This dissertation is one of the first PhD thesis submitted from IEK-13. The research has been performed on supercomputing resources provided within Jülich-Aachen Research Alliance, JARA-CSD partition. The JURECA and CLAIX supercomputers were used to performed the calculations.

# Chapter 1

# Introduction

## 1.1 Electrochemical $CO_2$ Reduction

Accelerating the energy transition for a more sustainable future has become a top priority in recent years [1]. With carbon dioxide ($CO_2$) emissions increasing continuously since the beginning of the industrial revolution, leading to serious climate change-related problems, such as droughts, flooding and extreme heat, to name a few [2, 3, 4], many countries have set a goal of curtailing $CO_2$ emissions to limit global warming well below 2°C relative to pre-industrial levels [5]. Drastic measures have to be taken to reduce $CO_2$ emissions in the future, such as moving to cleaner and renewable energy technologies (e.g., by utilizing solar or wind resources) [6]. Other approaches to reduce $CO_2$ emissions in the atmosphere include carbon capture and storage (CCS) [7, 8], where $CO_2$ is captured from the atmosphere and stored in underground repositories. Alternatively, $CO_2$ can be "recycled" and converted directly to other valuable products, by using electricity (preferably from renewable sources), in a process known as electrochemical $CO_2$ reduction ($CO_2$R) [9].

Electrochemical $CO_2$R takes place in a so-called $CO_2$ electrolyzer cell (Figure 1.1), where an external power source supplies electrical energy to the cell to drive chemical reactions in both compartments of the cell. In one of the compartments the oxygen evolution reaction (OER) occurs at the metal electrode, which is a conducting material immersed in the electrolyte solution. During the OER, molecular oxygen, electrons and protons are generated. Electrons and protons move to the other electrode located in the other compartment of the cell, on which $CO_2$ is reduced to value-added chemical products. The electrolyte is a conductive solution that facili-
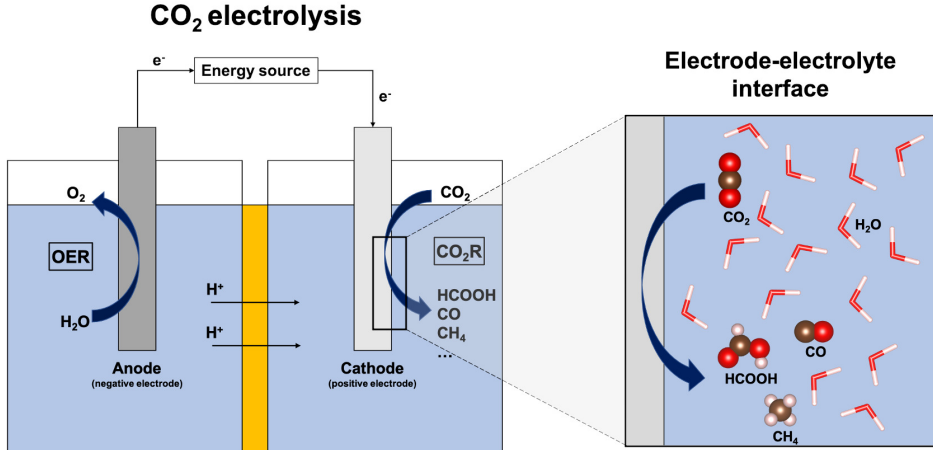
## $CO_2$ electrolysis



Figure 1.1: Schematic figure of a $CO_2$ electrolyzer cell and the electrode-electrolyte interface.

tates the movement of ions, i.e., protons and other ions, between the two electrodes. Different types of products can be generated during $CO_2$ reduction: methane ($CH_4$), formic acid (HCOOH), carbon monoxide (CO) or ethanol ($C_2H_5OH$), to name but a few. The type of product for a given electrolyzer depends on the applied electric potential and the number of electrons provided by the OER (Table 1.1). For instance, the $CO_2$ reduction towards CO requires an applied potential of -0.52 V (vs. SHE) to initiate the 2-electron transfer reaction, while the conversion of $CO_2$ towards $CH_4$ requires a potential of -0.24 V (vs. SHE) for an 8-electron transfer reaction.

Table 1.1: Possible $CO_2R$ half-cell reactions and the corresponding potential, V, derived using the standard hydrogen electrode (SHE) as a reference.

| $CO_2R$ reaction | V vs. SHE |
|---|---|
| $CO_2 + 2\,H^+ + 2e^- \rightarrow HCOOH$ | -0.61 |
| $CO_2 + 2\,H^+ + 2e^- \rightarrow CO + H_2O$ | -0.52 |
| $CO_2 + 8\,H^+ + 8e^- \rightarrow CH_4 + 2H_2O$ | -0.24 |
| $CO_2 + 12\,H^+ + 12e^- \rightarrow C_2H_5OH + 3H_2O$ | -0.33 |

During the 1980s, in the earlier stages of electrochemical $CO_2R$, Hori and co-workers have conducted a comprehensive experimental study of $CO_2R$ on different types of metal electrodes [10, 11], observing different main products for different metal electrodes (Figure 1.2). Lead (Pb), mercury (Hg), thallium (Tl), indium (In),

tin (Sn), cadmium (Cd), and bismuth (Bi) metal electrodes produced mainly formic acid (HCOOH), while gold (Au), silver (Ag), zinc (Zn), palladium (Pd), and gallium (Ga) metals generated mainly carbon monoxide (CO). Other metal electrodes (nickel (Ni), iron (Fe), platinum (Pt), and titanium (Ti)) showed very little $CO_2R$ activity, primarily due to the more dominant and competing hydrogen evolution reaction (HER). On the other hand, copper (Cu) metal catalyst material is capable of reducing $CO_2$ even further to products requiring more than 2 electron transfers. These include hydrocarbons or alcohols.
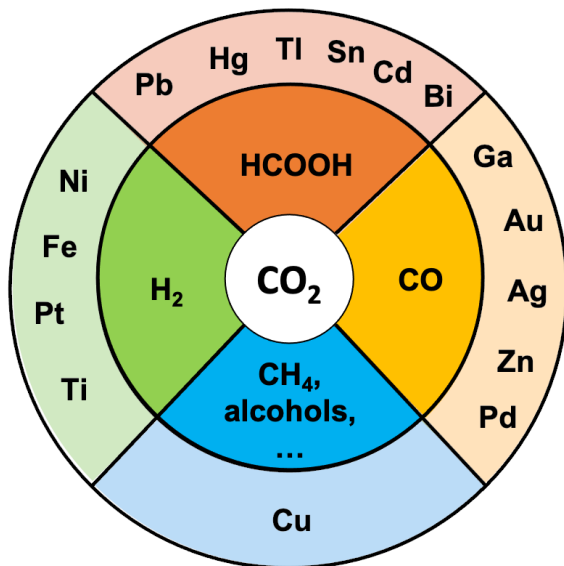


Figure 1.2: Primary $CO_2R$ reaction products (inner circle) on selected metal catalysts (outer circle). The data is based off experimental work of Hori [10].

The pioneering experimental work of Hori and co-workers laid a foundation for the further discovery of more active and selective electrochemical $CO_2R$ electrode materials. The quest to increase the selectivity of certain $CO_2R$ products and activity of an electrolyzer is driven by economic feasibility, market demand and necessity of energy transition. While on the one hand, there is a need for mass production of clean hydrogen [12] to facilitate the transformation to a large-scale hydrogen economy, on the other hand, there is high market demand for some $CO_2R$ products, e.g., ethanol or methane [13]. However, from an economic feasibility standpoint, focusing

on $CO_2$ reduction towards formic acid is the most attractive route [9]. Regardless of the motivation, significant experimental effort has been devoted to optimizing performance and cost of existing $CO_2R$ electrocatalysts. These include for instance surface modification, nanostructuring, alloying or doping [9, 14, 15, 16, 17, 18]. However, a deep, basic understanding of the catalytic properties of an electrocatalyst, such as selectivity and activity, is of foremost importance for a time- and cost-effective design of new electrocatalysts. As catalytic properties of electrocatalysts are determined by electronic structure of the applied electrodes, quantum mechanics-based atomistic simulation methods, such as Density Functional Theory (DFT), can play a fundamental role in facilitating the design of electrocatalysts. Due to the steady increase of supercomputing power and growing capability of simulating larger and more complex systems, simulation-based design of electrocatalysts is foreseen to take a leading role in the decades to come [19, 20, 21].

## 1.2   Atomistic Simulation of Metal-Electrolyte Interface

### 1.2.1   From Gas-phase Simulations to Solvation-based Simulations

Due to the complexity and associated high computational cost of atomistic simulations of chemical reactions on the solid-liquid interface, a majority of DFT-based surface chemistry studies have been conducted assuming simplified metal-gas interfaces, instead of the more realistic metal-electrolyte interfaces [22, 23, 24, 25]. However, those proved that even with such a simplified approach, valuable insight into the catalytic performance of materials can be delivered. With the groundbreaking works by Sabatier [26] and later extended by Norskøv and co-workers [22, 23], a correlation between theoretical molecule adsorption energy on the metal surface ($E_{ads}$), a simple descriptor calculated using DFT at the metal-gas interface, and experimental catalytic activity of the metal electrode ($J$) was established and is often applied in the analysis of performance of electrocatalysts. The graphical representation of this correlation, as shown in Figure 1.3 for pure metal surfaces, is also known as the volcano plot [24, 27, 28, 29, 30].
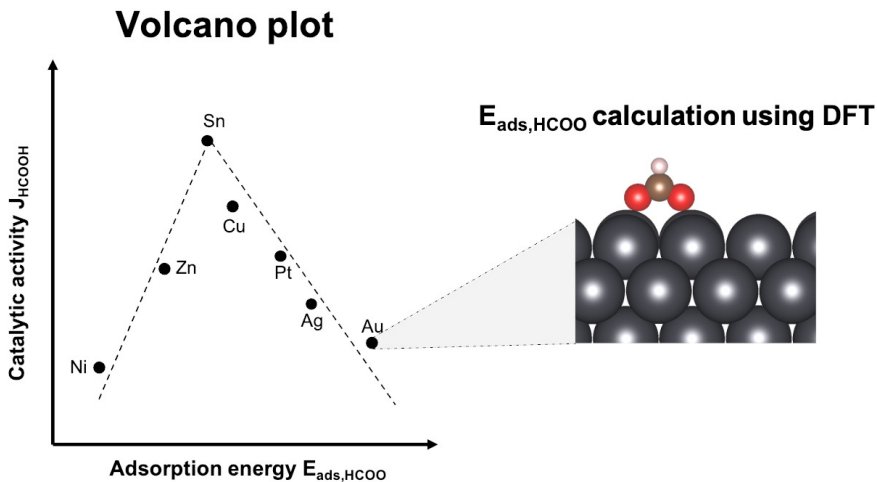
Figure 1.3: *Volcano plot showing HCOO reaction intermediate adsorption energy* $(E_{ads,HCOO})$ *as a descriptor of measured catalytic activity towards HCOOH product* $(J_{HCOOH})$. *The presented volcano plot is based on data adopted from Feaster et al. [27].* $E_{ads,HCOO}$ *for different metals were obtained using DFT calculations by Peterson and Nørskov [31].*

With the volcano plot, computed and measured data can be put into relation, which provides enhanced insight into the electrochemical performance of materials and guidance for their optimization. DFT data can also be useful for efficient screening of multiple electrocatalytic materials and selecting promising electrode materials for experimental follow-up [25, 32, 33, 34, 35, 36, 37]. Other DFT-based approaches involve computation of the whole $CO_2R$ pathways at the metal-gas interface. These provide key insights into reaction mechanisms that govern the behavior and selectivity of electrocatalytic materials. [38, 39, 40, 41, 42].

While computational studies of $CO_2R$ at the gas-metal interface provide valuable insight into the reaction mechanism, a more realistic description of the metal-electrolyte interface, including electrochemical conditions under applied voltage or accounting for solvation phenomena, is desirable for reliable computation of interface chemistry. Solvation effects can have an effect on the favorability of particular reaction pathways or reaction intermediates [43, 44, 45, 46, 47]. DFT studies of metal surfaces in the presence of solvation by Neurock et al. [43], Garcia-Ratés et al. [44] and Zhao et al. [45] show a clear change in active intermediates, compared to

studies neglecting solvent effects. These studies led to validation of experimentally observed products, providing precious insight and guidance for further experimental studies. Nie et al. [46] studied solvation effects on the $CO_2R$ at the Cu metal surface, identifying a different reaction-determining intermediate compared to the gas-phase prediction, confirming the experimentally observed reaction mechanism. By conducting a combined DFT/experimental work, Fan et al. [47] were able to match the measured onset potential for $CO_2$ reduction towards formate on the Pb surface. This was achieved by explicit computation of solvent water molecules.

To summarize, in the past computational gas-phase DFT has been a popular method to perform preliminary screening of the performance of catalysts. However, numerous DFT studies have shown that solvation effects play a fundamental role for a correct prediction of chemical reaction pathways at electrochemical interfaces, which helps to accelerate the understanding and design of more active and selective electrocatalytic materials. With the rapid and steady increase in availability of supercomputing power, DFT studies of complex models of electrochemical interfaces that, for instance, include solvation effects, will be possible in the decades to come.

## 1.2.2   Brief Review of Solvation Models at Interfaces

In the following, a brief review of noteworthy computational works dealing with solvation effects at interfaces are provided in order to highlight the contributions and shortcomings of the applied methodologies and pinpoint unresolved questions that remain in the computational treatment of solvation phenomena at the electrochemical interface.

In the 1980s, Doering and Madey [48] experimentally showed the existence of an ice-like water bilayer on the close-packed (0001) surface of ruthenium, where explicit water molecules are arranged on the surface in a hexagonally ordered manner. Subsequently, due to its simplicity, the static and computationally cheap ice-like water model was quickly adopted and applied in several computational works [45, 49, 50, 51]. However, as experimental measurements of water structures on metal surfaces became more abundant [52, 53], the simplistic concept of an ice-like water bilayer was more and more abandoned. High-resolution scanning tunneling microscope (STM) measurements by Nie et al. [52] have shown that the water bilayer is in fact unstable and distorted from its original hexagonal form. These experimental observations have

been confirmed by Groß et al. [49, 50, 54, 55, 56, 57] who performed significant computational works of water structures at metal surfaces using *ab initio* molecular dynamics (AIMD) simulations observing large fluctuations of the water bilayer at ambient temperatures. These findings underline the limitations of using static simplified water models. Given the dynamic nature of water, static water models are limited in reproducing structural charge rearrangements at the interface and are unable to describe entropic effects stemming from the dynamic behaviour of water [58]. While, in principle, AIMD can be an appropriate scheme to model solvation effects at the electrochemical interface [55], oftentimes the computed trajectories are too short to guarantee adequate statistical sampling of interface configurations due to the high computational cost of AIMD [59, 60]. Thus, other alternative solvation methods such as classical molecular dynamics (CMD) and quantum mechanics/molecular mechanics (QM/MM) have emerged to circumvent the computational expense of AIMD simulations.

In contrast to AIMD, CMD simulations describe atoms in a classical manner, which means that the interactions between atoms are approximated using a set of empirical equations, also known as the force field. This allows us to compute much larger systems in a computationally efficient manner. In QM/MM simulations only the region of interest is described by quantum mechanics, while the surrounding environment is also described by classical force fields. From a historic point of view, both CMD and QM/MM methods have gained popularity in the simulation of biological systems resulting in the development of various classical force fields, e.g., CHARMM [61], AMBER [62] and GROMOS [63], which are tailored to biological applications. Especially, the huge success of QM/MM simulations in biomolecular systems led by the three theoretical chemists Martin Karplus, Michael Levitt and Arieh Warshel resulted in the award of the Nobel Prize in Chemistry in 2013 [64]. While these two methods have attained state-of-the-art status in the field of biomolecular simulation, CMD and QM/MM simulations have only received limited attention in interface studies [65]. In contrast to "local" chemical bonds in biomolecular systems, bonds forming at metal-electrolyte interfaces are delocalised, resulting in a much more complex force field development and a less well-defined distinction of the QM and MM region [66, 67]. Furthermore, the main focus in biological systems has been in the investigation of structure and dynamics, e.g., protein folding, for which MD simulations are well-suited, whereas the focus of electrocatalysis was centered around chemical

reactions on surfaces, often utilizing DFT calculations in gas phases for this purpose [68, 69]. Since solvation effects at the electrochemical interface have gained more attention in past years, several research groups have devoted significant contributions to the advancement of CMD and QM/MM methods at the water-metal interface [70, 71, 72]. While Heinz et al. [71] have developed a classical force field, also known as the interface force field (IFF), to simulate solid-solvent interfaces, Steinmann et al. [70] and Clabaut et al. [72] introduced additional parameters for interactions with noble metal surfaces (GAL17 and GAL19 force field), which were effectively employed within the QM/MM approach. Preliminary results showed that adsorption energies of benzene and phenol at the Pt surface calculated within the QM/MM framework are in better quantitative experimental agreement than vacuum and implicit solvent calculations.

In contrast to the above mentioned explicit solvation methods, implicit solvation models treat the solvent as a polarizable continuum, without explicitly considering solvent molecules and thus reducing computational cost. However, recent studies have shown that hydrogen bonding near reaction intermediates plays a vital role in adsorbate stabilization, which cannot be captured using implicit solvation [44, 73, 74]. In a comprehensive benchmark study, Heenen et al. [73] compared adsorption energies derived from implicit solvation with reference AIMD simulations. Not only did they observe a notable disparity of up to 0.6 eV between the adsorption energies of implicit solvation method and AIMD simulations, but the implicit solvation approach yielded no significant improvement in adsorption energies compared to calculations *in vacuo*. Nonetheless, implicit solvation approaches continue to hold significance in the modeling of the electrochemical solid-liquid interface, primarily due to their flexibility in the use of counter charges at the electrified interface, which play a relevant role in the computation of the interface under applied potential [28].

The computation under applied potential, apart from solvation effects, is another important challenge in the complete computational description of the electrochemical interface [75]. However, since the scope of this dissertation only covers solvation effects at uncharged interfaces, I would like to refer the reader for further reading to a comprehensive review by Schwarz and Sundararaman [75], summarizing important works dealing with the computation of the electrified interface, or a recent publication by my colleagues Tesch et al. [76] applying state-of-the art hybrid DFT-classical molecular mechanics schemes to investigate properties of the Pt(111)/electrolyte electrochemical

interface under applied potential. More details about the different solvation methods are provided in Chapter 2.3.

In conclusion, after providing a brief overview of solvation effects at the interface, it is evident that there exist various solvation methods to treat the electrolyte environnment at the metal-electrolyte interface, from classical methods to hybrid methods and pure quantum mechanical-based methods. However, it is still not clear which method is universally applicable for an accurate description of the electrochemical interface. While quantum mechanical-based solvation methods suffer from computational inefficiency, classical methods are heavily reliant on suitable force fields to generate accurate results. As the predominant emphasis in first-principles electrocatalysis research over the past few decades has been at the electrode side, the computational description of the electrolyte side is a comparatively new research field. This opens up research questions to tackle in this thesis, whether it is advancing a more efficient simulation approach to compute solvation at the interface or pursuing a more accurate computational description of the electrochemical interface.

## 1.3   Scope and Outline of Work

Considering the large potential and challenges of the atomistic simulation-based description of solvation effects at metal-electrolyte interfaces, the main goal of this thesis is to perform systematic studies of different aspects of solvation phenonema, with the aim to improve different aspects of the computational description of metal-electrolyte interfaces and make related simulations feasible. Figure 1.4 illustrates three main topics covered in this thesis: interfacial water structure, impact of solvent on interfacial chemistry and importance of solvent-solute entropy effects on thermodynamical parameters of surface chemical reactions. With these three topics, the focus will be laid on obtaining a more complete description of the metal-electrolyte interface and providing more realistic, molecular level insight into interfacial processes, including testing of efficiency of existing solvation approaches.

This work is organized as follows:

- Chapter 2 introduces the computational methodologies applied in this thesis, followed by the basic concepts of atomistic free energy calculations on metal surfaces. In addition, different solvation schemes used to model adsorbates at metal-electrolyte interfaces will be presented.
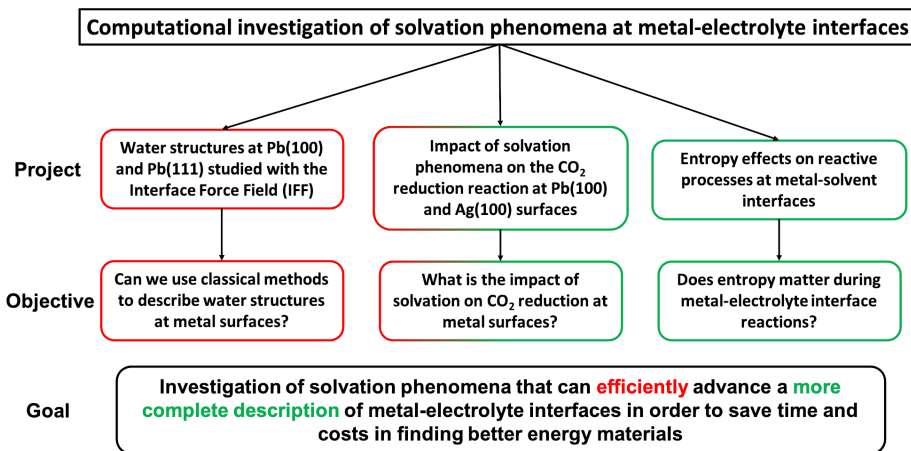
*Figure 1.4: Approach taken in this thesis and the main scientific questions tackled in a quest to investigate the role of solvation phenomena in determining the properties of metal-electrolyte interfaces. Colour of frames indicate the focus of the work: red colour focuses on efficiency of solvation approaches and green colour focuses on insights into a complete description of the metal-electrolyte interface.*

- Chapter 3 deals with the first project regarding simulation of water structures at the Pb metal surface. The correct description of the solvent structure at the interface is of key importance for accurate studies of electrochemical interfaces. A computationally efficient classical approach which uses the classical interface force field (IFF) to model water structures on the Pb surface is compared to a computationally intensive *ab initio* method, with the aim of testing the feasibility of using classical methods to describe water structures at metal surfaces. Results show that classical simulations permitted effective sampling of water structure and enabled exploration of ns time scales, not accessible to *ab initio* molecular dynamics (AIMD) simulations. Different equilibriated structures of interfacial water are obtained, proving that simulations using the IFF are capable of providing interfacial structures beyond the DFT level.

- Chapter 4 focuses on the second main project dealing with the evaluation of different solvation approaches to compute the metal-electrolyte interfaces. Here, the $CO_2R$ reaction on Pb(100) and Ag(100) metal surfaces is used as a test case. By accounting for solvation effects, the predicted and measured selectivity of both surfaces can be reconconiled, solving the long standing "puzzle" of different

behavior of Pb(100) and Ag(100) surfaces in that respect.

- Chapter 5 presents the third main project focusing on the investigation of entropy effects on surface reactions at metal surfaces. The two-phase thermodynamic (2PT) model together with classical force field simulations was applied to evaluate the feasibility of this computationally efficient approach to calculate entropy contributions of chemical reactions at metal-electrolyte interfaces. As for the aqueous electrolyte, this approach demonstrated good estimation of the entropy effects, which, when coupled with DFT calculations of reaction pathways, enables more realistic calculations of thermodynamic parameters at electrochemical interfaces.

- Lastly, Chapter 6 provides a summary of the thesis and a future outlook.

# Chapter 2

# Theory and Methodology

In this chapter, the main computational methodologies utilized in this thesis are summarized. Initially, the basic concepts of DFT and force-field-based molecular dynamics are introduced, followed by a brief summary of solvation schemes at metal-electrolyte interfaces and basic concepts of reaction energy calculations.

## 2.1 Density Functional Theory

### 2.1.1 Pre-DFT: The Path to Density Functional Theory

Modern quantum mechanical calculations aim to determine the electronic structure of molecules and materials in order to obtain relevant properties, e.g., bond lengths, bond angles, bond energies, and to provide a profound understanding of the chemical and physical behaviour of these systems. The electronic structure of a material is usually described well by the time-independent, non-relativistic Schrödinger equation [77, 78],

$$\hat{H}\Psi(\vec{r}, \vec{R}) = E\Psi(\vec{r}, \vec{R}). \tag{2.1}$$

Here $E$, $\Psi$ and $\hat{H}$, represent the total energy, the wave function and the Hamiltonian of the whole system, including the spatial vectors of both nuclei ($\vec{R}$) and electrons ($\vec{r}$), respectively. The Hamiltonian of the system comprises different energy terms

(Eq.(2.2)),

$$\hat{H} = \hat{T}_n + \hat{T}_e + \hat{V}_{nn} + \hat{V}_{ee} + \hat{V}_{en} \tag{2.2}$$

which consist of the kinetic energy of $M$ nuclei,

$$\hat{T}_n = -\frac{\hbar}{2m_A} \sum_{A=1}^{M} \nabla_A^2, \tag{2.3}$$

the kinetic energy of $N$ electrons,

$$\hat{T}_e = -\frac{\hbar}{2m_e} \sum_{i=1}^{N} \nabla_i^2, \tag{2.4}$$

the potential due to nucleus-nucleus interactions,

$$\hat{V}_{nn} = \sum_{A=1}^{M} \sum_{B>A}^{M} \frac{Z_A Z_B}{R_{AB}}, \tag{2.5}$$

the potential due to electron-electron interactions ,

$$\hat{V}_{ee} = \sum_{i=1}^{N} \sum_{j>i}^{N} \frac{1}{r_{ij}}, \tag{2.6}$$

and the potential from electron-nucleus interaction,

$$\hat{V}_{en} = \sum_{i=1}^{N} \sum_{A=1}^{M} \frac{Z_A}{r_{iA}} \quad . \tag{2.7}$$

Here, $m_A$, $Z_A$, $Z_B$, $R_{AB}$ are the mass of nucleus A, the charge of nucleus A, the charge of nucleus B and the distance between nucleus A and B, respectively. Similarly, $m_e$, $r_{ij}$ and $r_{iA}$ represent the mass of an electron, the distance between electron $i$ and electron $j$, and the distance between electron $i$ and nucleus A, respectively. $\hbar$ is the Planck constant. By considering both electrons and nuclei, the given system becomes increasingly large and difficult to solve. This is due to the presence of $3(N + M)$ spatial degrees of freedom, with $M$ and $N$ being the number of nuclei and electrons, respectively. With that being said, approximations to simplify the

Schrödinger equation are highly desirable.

One significant approximation to simplify the Schrödinger equation is the Born-Oppenheimer approximation [79], which takes into account that a nucleus is significantly heavier and slower than an electron leading to the assumption that nuclei can be considered relatively stationary in space. With this assumption the nuclei kinetic energy term $\hat{T}_n$ becomes zero and the potential due to nucleus-nucleus interaction $\hat{V}_{nn}$ can be considered a constant. Consequently, the Hamiltonian in Eq.(2.2) is reduced to the remaining terms shown in Eq.(2.8), also known as the electronic Hamiltonian (considering now $3N$ degrees of freedom),

$$\hat{H}_{elec} = \hat{T}_e + \hat{V}_{ee} + \hat{V}_{en} = -\frac{\hbar}{2m_e}\sum_{i=1}^{N}\nabla_i^2 + \sum_{i=1}^{N}\sum_{j>i}^{N}\frac{1}{r_{ij}} + \sum_{i=1}^{N}\sum_{A=1}^{M}\frac{Z_A}{r_{iA}}, \qquad (2.8)$$

where $\hat{T}_e$, $\hat{V}_{ee}$ and $\hat{V}_{en}$ are terms already explained in Eqs.(2.4), (2.6) and (2.7), respectively.

Additional attempts to simplify the Schrödinger equation encompass the Hartree product wavefunction [77], which assumes that the total electronic wave function $\Psi(r)$ is the product of $N$ separate one-electron wave functions where $x_N$ is defined as the position of the $N$-th electron and its spin state (Eq.(2.9)),

$$\Psi(x_1, x_2, ..., x_N) = \Psi_1(x_1) * \Psi_2(x_2) * ... * \Psi_N(x_N). \qquad (2.9)$$

In the applied approximation, it is assumed that the movement of the electrons are independent from each other and only interact with neighboring particles in an average manner. This approximation, also known as the Hartree approximation, disentangles the complex total electronic wave function into $N$ independent one-electron wave functions and is only useful for systems that have weak electron-electron interactions, since electron correlation effects are not adequately described by the mean-field approximation. The Hartree-Fock method extends the Hartree model by combining these product wave functions into a so-called Slater determinant [80] (Eq.(2.10)) that satisfies the Pauli exclusion principle [81], which states that two electrons cannot occupy the same quantum state.

$$\Psi(x_1, x_2, ..., x_N) = \frac{1}{\sqrt{N!}} * \det \begin{bmatrix} \Psi_1(x_1) & \Psi_2(x_1) & ... & \Psi_N(x_1) \\ \Psi_1(x_2) & \Psi_2(x_2) & ... & \Psi_N(x_2) \\ : & : & & : \\ \Psi_1(x_N) & \Psi_2(x_N) & ... & \Psi_N(x_N) \end{bmatrix} \quad (2.10)$$

Thus, on top of the Hartree potential, which describes the interaction of an electron with its average surrounding electron environment, a new type of potential also known as the exchange potential is included in the Hartree-Fock method [78], caused by the Pauli exclusion principle. While the Hartree Fock method manages to account for exchange potential effects, electron interactions are still described in an average manner, as electrons move in the average potential field due to all other electrons.

## 2.1.2 DFT Methodology

With the introduction of the electron density $n$ as a basic variable, obtained as a sum over $N$ one-electron density contributions (Eq.(2.11))

$$n(r) = 2 * \sum_{i=1}^{N} |\Psi_i|^2, \quad (2.11)$$

solving the Schrödinger equation has become less computationally demanding, as the complicated wave function with $3N$ spatial variables is reduced to a simpler and more intuitive quantity with 3 spatial variables.

In the mid-1960s Hohenberg and Kohn [82] laid the foundation of DFT by deriving two central theorems introducing the electron density $n$ as a basic variable instead of the many-electron wave function:

- Theorem 1 states that the ground-state energy of the Schrödinger equation is a unique functional of the electron density $n$.

- Theorem 2 states that the full solution of the Schrödinger equation can be found by the electron density that minimizes the energy of the overall functional.

Essentially, rather than solving the Schrödinger equation directly, the problem is transformed into minimizing the energy functional with respect to the electronic

density. Kohn and Sham [83] postulated and proved the existence of an auxiliary non-interacting system with the same ground state density as the interacting system. Consequently, by solving the Kohn-Sham equations,

$$[-\frac{\hbar}{2m_e}\nabla^2 + V(r) + V_H(r) + V_{XC}(r)]\Psi_i(r) = \epsilon_i\Psi_i(r), \tag{2.12}$$

with

$$V_H(r) = \int \frac{n(r')}{|r - r'|}dr', \tag{2.13}$$

and

$$V_{XC}(r) = \frac{\delta E_{XC}[n]}{\delta n(r)}, \tag{2.14}$$

it becomes possible to find the electronic density that minimizes the total energy of the interacting system. The first two terms in Eq.(2.12) are similar to the terms in the electronic Hamiltonian (Eq.(2.8)) with $-\frac{\hbar}{2m_e}\nabla^2$ and $V(r)$ representing the electron kinetic energy and the interaction between an electron and atomic nuclei, respectively. Similar to the Hartree-Fock formalism, $V_H(r)$ represents the Hartree potential, which considers the Coulomb repulsion between an electron and the total electron density of all electrons. More importantly, $V_{XC}(r)$ includes both exchange and correlation effects, accounting for self-interaction errors caused by the Hartree potential as well as other effects not covered by non-interacting electrons such as the electron-electron repulsion. While the introduction of the exchange and correlation contribution leads to a more complete description of electronic effects, a primary objective of DFT remains the development of advanced approximations for exchange-correlation (XC) functionals to improve the prediction of molecule and materials properties.

In order to solve the KS equations, provided in Eq.(2.12), an iterative approach is required, since the Hartree potential term (Eq.(2.13)) in the KS equation depends on the electron density $n(r)$, which itself depends on the single-electron wave function $\Psi_i(r)$ from the KS equation. Figure 2.1 illustrates the iterative cycle to solve the KS equation. After initializing a trial electron density of a given system, the single-electron wave function is calculated by solving the KS equation, as shown in Eq.(2.12). After that, the new electron density is obtained from Eq.(2.11) and compared to

the initial electron density. The iterative procedure is repeated until the difference between the new electron density and the previous electron density is small enough, indicating convergence. Once the iteration is converged, output properties such as energy or forces are computed.
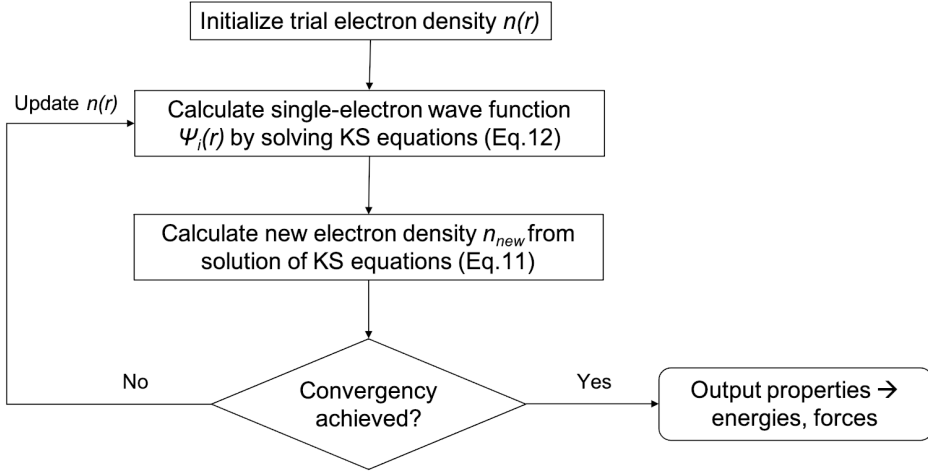


*Figure 2.1: Simple illustration of iteration cycle applied to solve the KS equations.*

### 2.1.3 Approximations of DFT

In the pursuit of finding the "exact" exchange-correlation (XC) functional, numerous approximations have emerged. These differ in computational cost and accuracy. The development follows the so-called Jacob's ladder of XC functionals described by Perdew et al. [84] (Figure 2.2). Jacob's Ladder metaphorically represents a series of ascending theoretical levels to approximate the XC functional. In this picture, the Local Density Approximation (LDA) is the simplest functional form and serves as basis for development of other approximations. It assumes that the XC energy dependence on the density has the same form as an uniform electron gas. While the LDA functional works quite well for bulk solids, where the electron density varies slowly, it performs quite poorly in the prediction of atomic and molecular properties due to the presence of non-local interactions. Thus, further improvements have been made by adding a density gradient correction to the LDA approximation, based on the premise that electron densities are not uniform in reality. Such functionals are

categorized as Generalized Gradient Approximation (GGA) functionals. GGA approximations such as PBE [85] are widely used to study metals and also applied in this thesis. Hybrid functionals such as B3LYP [86] are located higher up the ladder and combine the GGA functional with the exact Hartree-Fock exchange. This hybridization enhances the precision of DFT predictions in determining properties of small molecules, such as bond lengths or formation energies [77].

| XC functional | Examples |
|---|---|
| Fully Nonlocal Functionals | vdW-DF2 |
| Hybrid Functionals | B3LYP |
| Meta-GGA | TPSS |
| Generalized Gradient Approximation (GGA) | PBE |
| Local Density Approximation (LDA) | PW |

Computational cost
Accuracy

*Figure 2.2: Overview of Jacobs's ladder of XC functionals with common examples for each level. PW [87], PBE [85], TPSS [88], B3LYP [86] and vdW-DF2 [89] represent cases of LDA, GGA, meta-GGA, hybrid functionals and fully nonlocal functionals, respectively.*

As shown in Figure 2.2, by going up the ladder more complexity to the functionals are added. In general, the obtained approximations become more accurate but at the expense of computational cost. Going beyond GGA and hybrid functionals, however, may only yield minor improvement in the DFT results and can give rise to issues regarding the transferability of the functional [90]. So to say, a functional which works for the system on which it was tested, often does not perform well for other systems. Also, improvement in description of one property (e.g., lattice parameters) often leads to worsening of prediction of other parameters. Thus, the final choice of the functional depends on the type of system to which it is applied. In terms of universal applicability, PBE exchange-correlation functional is commonly applied to study reactions on metal surfaces [90].

Apart from approximations for the XC functionals, the single-electron wave functions $\Psi(r)$ are also described on a set of so-called basis functions. This allows to solve KS equations in a computationally efficient manner. Basis sets are composed of a set of mathematical functions that either mimic atomic orbitals, such as Slater Type Orbitals (STOs) or Gaussian Type Orbitals (GTOs) [91], or represent delocalized orbitals in periodic solids. For the latter case, the plane waves basis set is usually applied. I have applied this approach in this thesis. According to Bloch's theorem [92], the one-electron wave function in a periodic system can be written as:

$$\Psi(r) = \sum_G c_G e^{i(\vec{k}+\vec{G})\vec{r}} \tag{2.15}$$

where $\vec{k}$, $\vec{r}$ are the position vectors in reciprocal and real space, $\vec{G}$ is the reciprocal lattice vector and $c_G$ represent the plane-wave expansion coefficients. The description of the wave-function in the plane wave basis set requires the selection of the total number of plane waves, which corresponds to the size of the basis set. Increasing the number of plane waves improves the accuracy of wave function representation and related solutions for energy and forces, but at the expense of greater computational time. An upper limit for $G$, $G_{cut}$, is thus applied to cutoff the number of plane wave functions to represent the wave function. $G_{cut}$ is dependent on the plane wave energy cutoff, $E_{cut}$,

$$E_{cut} = \frac{\hbar}{2m_e} G_{cut}^2, \tag{2.16}$$

which is a common value reported in DFT calculations. In DFT calculations performed throughout this work, the energy cutoff value of 50 Ry is applied, unless a different value is indicated.

Lastly, the utilization of plane wave basis sets to describe wave functions in the close vicinity of nuclei can become cumbersome due to strong oscillations of the wave function, requiring a large number of plane waves to describe these oscillations. Thus, so-called pseudopotentials can instead be efficiently used to approximate the effects of core electrons, but still capturing important physical properties of the true electron density [77].

## 2.2   Force Field-based Molecular Dynamics

### 2.2.1   Molecular Dynamics Algorithm

When it comes to the computation of metal-water interfaces, studying the time evolution of the system using the molecular dynamics (MD) method is of significant importance. Sufficiently long MD trajectories and a representative set of possible

water configurations are required to reliably assess the effects for hydration [49, 70]. For a given description of interatomic interactions, MD relies on solving Newton's equations of motion for position and velocity vectors of all atoms, which are required for the time evolution of the investigated system.

Figure 2.3 shows an illustration of a standard MD algorithm. The iteration cycle
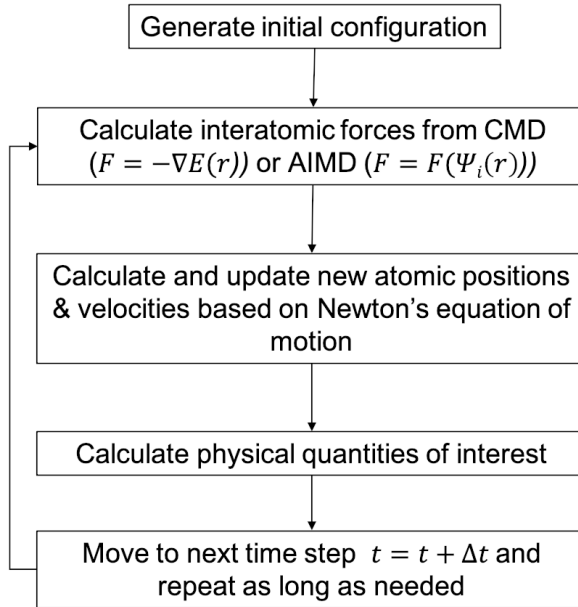


*Figure 2.3: Simplified illustration of standard MD algorithm. $E(r)$ and $\Psi_i(r)$ stand for the classical interatomic potential and the electronic wavefunction, respectively.*

starts with the generation of an initial atomic configuration of the investigated system, followed by the calculation of the forces acting on the atoms, which are obtained by calculating the gradient of the interaction potential energy ($F = -\nabla E$). While *ab initio* molecular dynamics (AIMD) uses methods of quantum chemistry to calculate the forces acting on atoms (as shown in Chapter 2.1), classical molecular dynamics (CMD) relies on so-called force fields, which are a set of empirical equations to describe particle interactions. AIMD is generally more accurate compared to CMD. However, being computationally intensive, AIMD has limitations for the system sizes and time scales that could be simulated. These limitations can be overcome by using the CMD approach, since particle interactions are calculated using computationally less

demanding empirical equations, allowing simulations of longer time and bigger system size scales. More on the types of force fields are presented in the next section.

Once the forces acting on the atoms are known, new atomic positions and velocities are calculated in the next iterative loop of solving Newton's equations of motion. Other physical parameters of interest can also be computed, e.g., the total energy of the system at a given time instance. This reported procedure is repeated $n$ time steps. There is no clear guidance of how many number of time steps are needed in a MD simulation and it really depends on what property is studied. For instance, for the calculation of the self-diffusion coefficient of bulk water, the number of time steps in the time range of ps have been sufficient to match experimental data [93]. Thus, the time step ($\Delta t$) separating the iterations has to be carefully chosen. A too small value may significantly increase the computational effort without any noticeable gain in accuracy. On the other hand, a too large time step may result in inaccurate solution of Newton's equations of motion and poor quality MD simulations [94].

### 2.2.2 Force Field for CMD

The type of force fields applied in CMD simulations depends both on its applicability to a specific system and availability. Widely used force fields such as CHARMM [61], AMBER [62] and GROMOS [63] force fields were originally developed for simulations of biomolecular systems. The OPLS force field [95] was developed for condensed matter applications [96]. More recently developed force fields allow for simulation of solvated metal systems, e.g., Interface Force Field (IFF) [71]. This type of force field is widely utilized in this thesis for the study of metal-solvent interfaces, see Chapters 3 and 5.

In general, the functional form of the different force fields are similar and include the sum of all bonded and non-bonded atomic interactions [97], as shown in Figure 2.4 and Eq.(2.17), with bonded interaction energies associated with the bonding between two atoms ($E_{bonds}$), the bending of an angle ($E_{angle}$), the torsion of a dihedral angle ($E_{dihedral}$), and improper interaction ($E_{improper}$), and non-bonded interaction energies associated with Coulomb ($E_{Coulomb}$) and van der Waals ($E_{vdW}$) interactions:

$$E_{pot} = E_{bond} + E_{angle} + E_{dihedral} + E_{improper} + E_{Coulomb} + E_{vdW} \qquad (2.17)$$
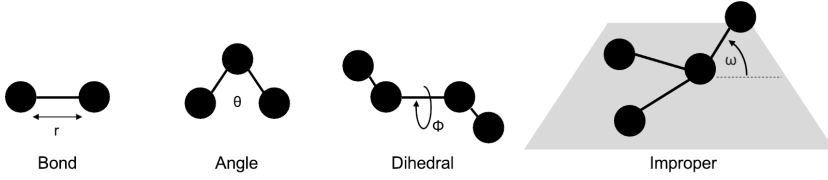
*Figure 2.4: Simplified illustration of bonded and non-bonded interactions that constitute classical force fields.*

In case of the Interface Force Field, the bonded and non-bonded atomic interaction terms are described by

$$E_{VdW}(r_{ij}) = 4\epsilon[(\frac{\sigma}{r_{ij}})^{12} - (\frac{\sigma}{r_{ij}})^6], \qquad (2.18)$$

also known as the Lennard-Jones (LJ) potential, with $\epsilon$ and $\sigma$ representing empirical constants describing the depth of the potential well and the van der Waals radius, respectively. The Coulomb electrostatic interaction is decribed by

$$E_{Coulomb}(r_{ij}) = \frac{Cq_i q_j}{\epsilon r_{ij}}, \qquad (2.19)$$

with $C$, $q_i$, $q_j$ and $\epsilon$ representing the energy-conversion constant, the charge on atom $i$, the charge on atom $j$ and the dielectric constant. The bonded interactions are described by

$$E_{bond}(r) = \frac{k}{2}(r - r_0)^2, \qquad (2.20)$$

with $k$, $r$ and $r_0$ representing the spring constant of the specific bond, the distance between the atoms and the equilibrium bond distance, respectively,

$$E_{angle}(\theta) = \frac{k}{2}(\theta - \theta_0)^2, \tag{2.21}$$

with $\theta$ and $\theta_0$ representing the angle of the molecule and the equilibrium value of the angle, respectively,

$$E_{dihedral}(\phi) = k[1 + dcos(n\phi)], \tag{2.22}$$

with $\phi$ representing the angle of torsion and $d$ and $n$ being empirical coefficients, and

$$E_{improper}(\omega) = k[1 + dcos(n\omega)], \tag{2.23}$$

with $\omega$ describing the angle of the molecule relative to a given plane.

## 2.2.3    Statistical Ensembles

In addition to simulating the dynamic behaviour of specific systems, MD is capable of keeping specific state variables constant, e.g., temperature $T$ and pressure $p$, mimicking realistic conditions. Depending on which state variables are kept constant, different so-called statistical ensembles are generated. The microcanonical ensemble, also known as NVE, keeps the number of particles ($N$), the volume ($V$) and the total energy of the system ($E$) constant. NVT, also referred to as canonical ensemble, and NPT, also referred to as isothermal-isobaric ensemble, allow to keep the temperature and/or pressure of the system constant by applying so-called "thermostats" and "barostats" [98]. As an example, Nose-Hoover thermostat [99] maintains a desired temperature in a given system by introducing a "virtual" heat reservoir that interacts with the system. When the actual temperature is too high/low, this reservoir interacts with the system to decelerate/accelerate the particles and bring the temperature to the desired value. More details on temperature and pressure control schemes are given in [98].

## 2.3   Solvation Schemes of Adsorbates at Metal-Electrolyte Interfaces

Solvation effects significantly influence chemistry on metal-electrolyte interfaces reactions. However, an optimal computational scheme for solvation is needed for accurate and computationally efficient calculations of such systems. Here, different solvation schemes are discussed that are widely used for modeling solvated adsorbates at metal surfaces. These approaches are summarized in Figure 2.5. In particular, implicit, explicit and hybrid solvation approaches are discussed, which have been applied in all three main projects of this thesis (as outlined in Chapter 1.3).

### 2.3.1   Implicit Solvation

The implicit solvation scheme treats the solvent environment as a continuous, polarizable medium. This allows bypassing expensive computation of explicit solvent molecules, making simulations more efficient and at the same time allows for capturing essential aspects of interactions of the computed system with the solvent environment [28, 75]. The commonly used implicit solvation inplementations in DFT, e.g., Environ [100] or VASPsol [101, 102], are based on the polarizable continuum model (PCM) [103], characterized by a dielectric permittivity function $\epsilon$. In the self-consistent continuum solvation (SCCS) model used in the Environ package, the dielectric function $\epsilon$ of the solvent environment depends on the electronic density of the solute, $n^{solute}$ (Eq.(2.24)):

$$\epsilon = f(n^{solute}) \tag{2.24}$$

Using the case shown in Figure 2.5(d) as an example, the electronic density of the solute is given by the electronic density of the HCOO molecule adsorbed on the metal surface. The dielectric function is set up in a way to ensure that the dielectric permittivity value equals 1 (vacuum value) inside the solute. In this region, the electron density of the solute is present and the solvent itself is absent. Moving away from the solute, the value of the dielectric permittivity smoothly increases to the value of the bulk solvent, $\epsilon_s$, in the region where $n^{solute}$ decays to 0. This SCCS
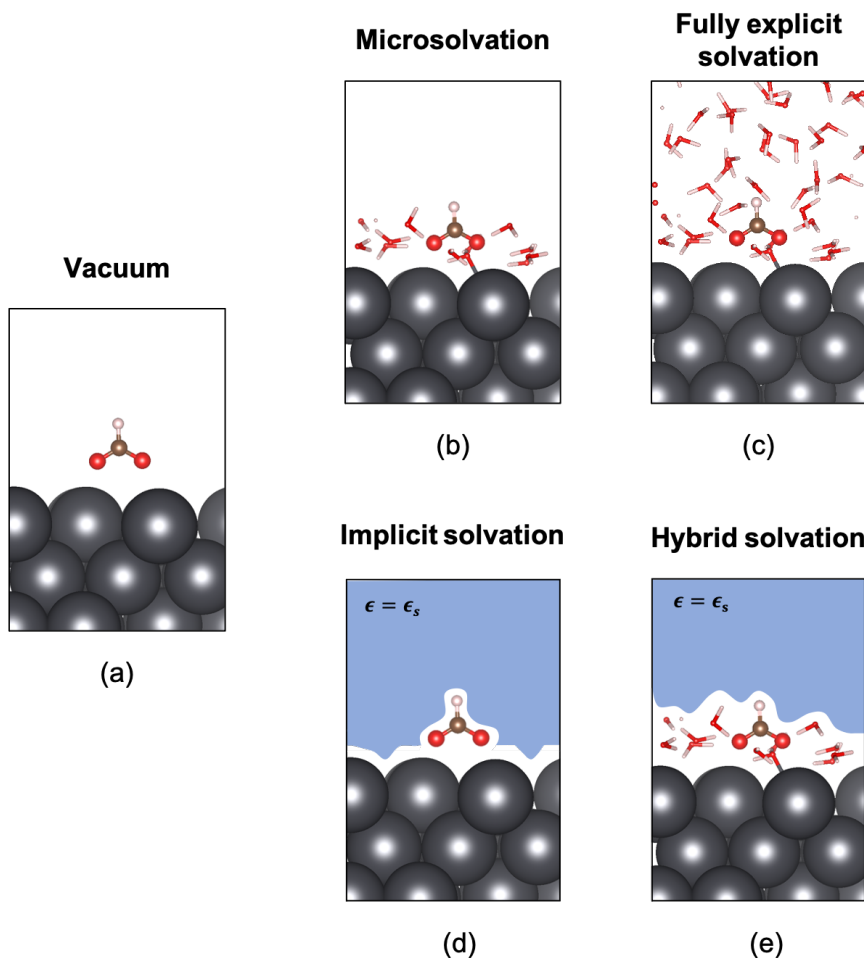
*Figure 2.5: Illustration of common solvation schemes using HCOO adsorbate at a metal surface as an illustration case. The approaches span from explicit solvation, such as (b) microsolvation and (c) fully explicit solvation, to (d) implicit solvation and (e) hybrid solvation cases. $\epsilon = \epsilon_s$ represents the dielectric bulk constant of the continuous, solvent medium.*

method, in which the region occupied by the solvent is determined by the electronic charge density of the solute, is employed in the VASPsol and ENVIRON packages. An alternative model is the soft-sphere continuum solvation (SSCS) [104], which instead uses the sum of atomic positions to describe the dielectric function.

In simple terms, the implicit solvation scheme adds an additional density term, also known as the polarization density ($n^{pol}$), on top of the density defined in the vacuum case $n^{solute}$, as already demonstrated in Figure 2.1.

Thus, the new electronic density is defined as the following,

$$n^{new} = n^{solute} + n^{pol}[\epsilon, \nabla\phi^{total}], \tag{2.25}$$

where $n^{solute}$ and $n^{pol}[\epsilon, \nabla\phi^{total}]$ represent the electronic density of the solute and the density effects from the continuous solvent environment, respectively. $n^{pol}[\epsilon, \nabla\phi^{total}]$ depends on the dielectric function, $\epsilon$, as defined in Eq.(2.24), and on the total electrostatic potential of the system $\phi^{total}$, which is derived from the Poisson equation,

$$\nabla^2\phi^{total} = -4\pi(n^{solute} + n^{pol}). \tag{2.26}$$

As the total electrostatic potential of the system $\phi^{total}$ is itself also dependent on $n^{pol}$, the inclusion of the implicit solvation scheme requires an iterative procedure. While implicit solvation is a computationally efficient method to mimic an ensemble representation of the solvent molecules, it has been shown that in some cases continuum solvation is not capable of adequately capturing solute-solvent interaction effects in the way as explicit solvation methods for strongly solvated solutes/adsorbates do [73, 105]. Moreover, for some cases, adding implicit solvation to the vacuum system might not substantially improve the adsorption energy of molecules adsorbed on the surface [74].

## 2.3.2   Explicit Solvation

The explicit solvation approach is capable of capturing chemical interactions in the direct vicinity of the adsorbate, by computing water molecules explicitly in a given system. However, every additional explicit water molecule computed at the quantum mechanical level increases the computational effort. So far, it is computationally unfeasible to simulate solid-solvent interfaces using thick solvent layers (Figure 2.5(c)), and such an approach is only sporadically applied. Instead, in most studies only a few, key explicit water molecules in the vicinity of the relevant adsorbate are computed [47,

106, 107, 108, 109, 110]. These so-called microsolvation approaches (Figure 2.5(b)), whether they consider only one water molecule or a full layer of water molecules explicitly, improved the description of the solid-electrolyte interface in various studies [47, 106]. In case of the aqueous solvent, a static hexagonal ice-like water bilayer structure is often utilized to represent the water structure at close packed metal surfaces [107, 108, 109, 110].

However, the microsolvation approach has also unavoidable shortcomings. For instance, a good statistical sampling of the water structure is required to correctly capture the dynamics of aqueous solvent. While this issue can be overcome with AIMD and CMD, as discussed in Chapter 2.2.1, these methods have also limitations, which are tested and discussed in Chapter 3 of this thesis.

### 2.3.3 Hybrid Solvation

In order to find a balance between accuracy and computational efficiency, a combination of implicit and explicit solvation schemes can be applied [105, 76, 72, 74, 111]. Such hybrid solvation schemes describe the solvent environment in proximity of the adsorbate explicitly, while computing the rest of the system either with implicit solvation or using classical force-fields (Figure 2.5(e)). While some prior studies have successfully adopted this hybrid approach to metal-electrolyte interfaces [72, 76, 105], it is unclear how the obtained results compare to the microsolvation approach and whether the additional implicit solvation has any significant improvement in comparison to simulations *in vacuo* [74, 111].

To conclude, there is no consensus regarding which of these methods is the best choice for the computation of metal-electrolyte interfaces. The results of this thesis contribute towards resolving this issue.

## 2.4 Calculation of Reaction Free Energy

### 2.4.1 Computational Hydrogen Electrode (CHE)

Accurate calculation of the free energy of surface reactions is of utmost importance in computational electrochemistry. It enables the assessment of electrocatalyst performance for specific chemical pathways, e.g., the $CO_2$ reduction reaction towards different products (see Table 1.1). In order to determine the reaction free energy

change of a reaction, also denoted as $\Delta G_r$, the free energies of both products and educts of the reaction are required. Taking the $CO_2$ reduction reaction towards adsorbed formate (HCOO*) as an example,

$$CO_2(g) + H^+ + e^- \rightarrow HCOO^*, \tag{2.27}$$
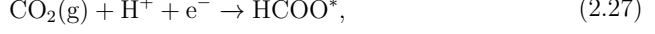
the Gibbs free energy change, $\Delta G_r$, is computed as

$$\Delta G_r = G_{HCOO^*} - G_{CO_2} - G_{H^+} - G_{e^-}, \tag{2.28}$$

where $G_{HCOO^*}$, $G_{CO_2}$, $G_{H^+}$ and $G_{e^-}$ represent the Gibbs free energies of adsorbed formate, $CO_2$, a proton and an electron, respectively. Nørskov and co-workers simplified the Gibbs free energy calculation by replacing the Gibbs free energy of $H^+$ and $e^-$ with the Gibbs free energy of a $H_2$ molecule in the gas phase ($G_{H_2}$), which is more straightforward to compute. This theoretical framework, also known as the computational hydrogen electrode (CHE) approach [22], is commonly used in description of electrochemical reactions at the electrode-electrolyte interface. The CHE framework is based on the assumption that under standard conditions, there exists an equilibrium between the exchange of proton-electron pairs and hydrogen molecules in gas phase, described by the reaction

$$0.5\ H_2 \leftrightarrow H^+ + e^-. \tag{2.29}$$

Under this assumption, the $G_r$ of reaction (2.27) changes to

$$\begin{aligned} \Delta G_r &= G_{HCOO^*} - G_{CO_2} - 0.5 * G_{H_2} \\ &= H_{HCOO^*} - TS_{HCOO^*} - (H_{CO_2} - TS_{CO_2} + 0.5 * (H_{H_2} - TS_{H_2}))), \end{aligned} \tag{2.30}$$

where the Gibbs free energy terms of both products and educts is further divided into enthalpic ($H$) and entropic contributions ($TS$). The enthalpy term ($H$) consists of the adsorption energy of the product/educt on the surface ($E$), i.e., the adsorption energy of $CO_2$ on the catalyst surface, and the zero-point energy (ZPE). Both $E$ and

ZPE as well as the vibrational entropic contribution term can be calculated using DFT. More details on the calculations of these terms will be discussed in Chapter 4, where reaction energy calculations are conducted for $CO_2$ reduction reactions on Pb and Ag catalysts. The computation of entropy in presence of solvent phase is also an important part of this thesis and will be discussed in Chapter 5.

Figure 2.6 illustrates a Gibbs free energy diagram of $CO_2$ reduction to HCOO by the addition of a proton and an electron, as shown in Eq.(2.27). The reaction energy
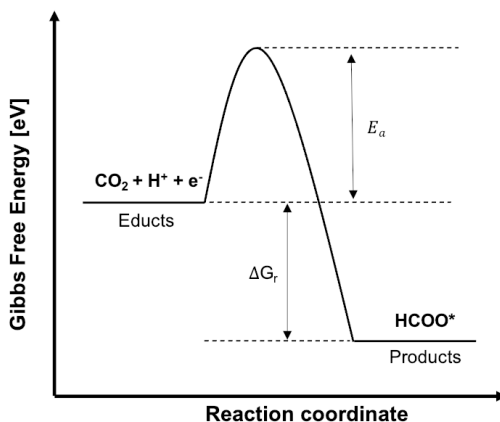


*Figure 2.6: Simple illustration of Gibbs free energy diagram of $CO_2$ reaction step to adsorbed HCOO. Thermodynamic reaction free energy change ($\Delta G_r$) is the free energy difference between the products and educts, while activation barrier ($E_a$) is determined by the energy difference between transition state and educts.*

diagram shows a reduction in Gibbs free energy when $CO_2$ reacts to adsorbed HCOO on the catalyst surface, indicated by $\Delta G_r$. While the calculation of $\Delta G_r$ is related to the thermodynamics of the electrochemical reaction, calculation of the activation barrier, $E_a$, which is the energy required to reach the transition state, plays a crucial part in understanding the kinetics of a chemical reaction. A high activation barrier indicates a higher energy needed to trigger the reaction and thus corresponds to slow reaction kinetics. In order to determine the minimum energy path (MEP) and the transition states along the reaction pathway, so-called Nudged Elastic Band (NEB) calculations are utilized, which are explained in more detail in the next section.

## 2.4.2 Nudged Elastic Band (NEB) Method

The NEB method is a commonly used computational method for obtaining the activation barrier, $E_a$, for the MEP of a chemical reaction [112, 113]. The MEP is obtained by constructing a set of images between the initial state and the final state of the considered chemical reaction. By adding a virtual, spring-like interaction between neighbouring images or states, imitating elastic bands, continuity of the reaction path is ensured. During the MEP search process, the positions of the different images are optimized and "nudged" along the band towards the MEP. The calculation of the total force acting on each atom ($F_i$) in the NEB method involves not only the atomic force ($F^a$), obtained from standard DFT calculations, but also the spring forces ($F^s$) connecting the neighbouring images

$$F_i = F^s_\parallel + F^a_\perp = F^s_\parallel - \nabla V(R_i)_\perp, \tag{2.31}$$

where $F^s_\parallel$ is the parallel component of the spring force and $F^a_\perp$ is the perpendicular component of the atomic force obtained from the potential energy gradient $\nabla V(R_i)_\perp$. Figure 2.7 illustrates the MEP of $CO_2$ to adsorbed HCOO on the Pb(100) surface calculated with the NEB method using 5 intermediate images connected via springs. These images include the initial state, $CO_2$, and the final state, HCOO.

A widely used modification of the NEB method is the climbing imaged nudged elastic band (CI-NEB) approach [114]. In this scheme, a climbing image is added to the NEB path, pushing that image towards the highest energy point and ensuring a more accurate location of the transition state of the reaction pathway. The CI-NEB scheme is applied through the thesis.
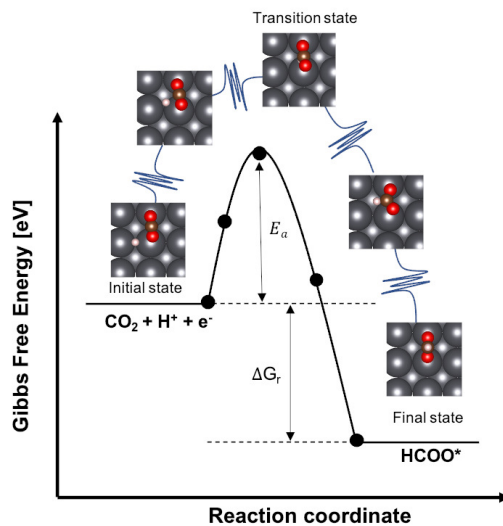
*Figure 2.7: Illustration of MEP for $CO_2$ reaction step to adsorbed HCOO using NEB with 5 images. All images are connected by virtual, elastic springs. The activation barrier ($E_a$) is determined by the energy difference between the transition state and the intial state.*

# Chapter 3

# Water Structures on Pb(100) and (111) Surface Studied with the Interface Force Field (IFF)

**Note:** Since the following chapter is based on the publication "O. Cheong, M. H. Eikerling, P. M. Kowalski, Water structures on Pb(100) and (111) surface studied with the Interface force field, Appl. Surf. Sci. 589, 152838 (2022)", the personal pronoun "we" is used throughout this chapter to refer to the group of researchers that were part of this specific study. In this study, my main contributions involve simulating and analyzing water structures at the Pb(100) and (111) surfaces as well as composing the manuscript. The co-authors mentioned above played a supervisory role in this research.

As mentioned in Chapter 1.3, the first aspect in advancing the computational description of the metal-electrolyte interface deals with the feasibility of using computationally efficient classical methods to describe water structures at metal surfaces. We performed classical molecular dynamics (CMD) simulations of water structures on Pb(100) and (111) surfaces. The main objective was to test the capability of the classical interface force field (IFF) to reproduce water structures obtained from more computationally intensive *ab initio* molecular dynamics (AIMD) simulations. At the same length and time scales we find good agreement between water structures obtained with both approaches. However, much longer trajectories (ns vs. ps scale) that can be simulated with CMD led to the formation of different, more stable wa-

ter structures, which were validated by supplementary *ab initio* calculations. CMD simulations performed for interface models with larger surface size revealed significant surface cell size effects, implying that the small simulation cells permitted by AIMD could be insufficient to obtain properly equilibrated water structures. These results will show how useful and advantageous CMD simulations with the IFF can be for the rapid sampling of more realistic time and length scales in simulations of metal-aqueous solution interfaces.

## 3.1   Introduction

Interactions between solvents and metal surfaces play a significant role in interfacial electrochemical processes [19]. They strongly affect the activity and selectivity of surface electrochemical processes, including oxygen and hydrogen evolution or $CO_2$ reduction reactions [45, 55, 115, 116]. While significant efforts have focused on understanding the formation of water structures on metal surfaces, both computationally [54, 56, 108, 117] and experimentally [118, 119, 120], no conclusive model has emerged. For instance, Doering and Madey [48] experimentally showed the existence of an ice-like water bilayer on the close-packed (0001) surface of ruthenium. This bilayer structure was initially adopted in first principle calculations of various metal surfaces [45, 49, 50, 51]. However, as more results on interfacial water structures became available, both experimentally and theoretically, the idea of an ice-like water bilayer was gradually abandoned [53, 56, 119, 121]. Low-energy electron diffraction (LEED) measurements [119] and density functional theory (DFT) calculations [53] have shown the relative instability of the bilayer water structure compared to a more stable water monolayer. More comprehensive discussion of models of water layers on metal surfaces can be found in the recent literature [107, 122, 123].

The dynamics of water layers on metal surfaces can be simulated with the *ab initio* molecular dynamics (AIMD) or classical molecular dynamics (CMD) techniques. While AIMD provides higher accuracy than CMD, it is computationally much more demanding and the resulting trajectories are usually too short to ensure sufficient statistical sampling of interface configurations [59, 60]. CMD simulations allow simulating longer times and larger systems, although often at the expense of accuracy [124]. The classical force fields-based approach has been also applied in some advanced hybrid DFT-classical molecular mechanics schemes applied to metal-electrolyte inter-

faces, including the DFT/ESM-RISM (Effective Screening Medium-Reference Inter-action Site Model) method [76, 125]. Simple force field-type approaches, or even the classical mean-field-type treatment, correctly capture some key interfacial properties like surface charging, alignment effects, dipole fields and variation in the dielectric constant of water at the interface, to name but a few [76, 126]. The accuracy of CMD and other force field-based approaches depends sensitively on the force field applied to describe interactions between molecules and atoms in the modeled system. The interface force field (IFF) developed by Heinz et al. [71] is specifically designed to simulate solid-solvent interfaces; it includes interactions between certain metals and interfacial water molecules. However, studies of Berg et al. [117] and Steinmann et al. [70] revealed deficiencies of the IFF due to, for instance, neglecting Au-H and Pt-H interactions. It is thus worth further testing and improving the IFF parametrization for two reasons: (1) the IFF has not yet been widely tested for metal-water interfaces; (2) CMD is much more computationally efficient than AIMD and allows for simula-tion of larger systems and longer trajectories, and thus enables improved statistical sampling.

Here we focus on the investigation of the lead-water interface, an electrocatalytic system for $CO_2$ reduction [9, 10, 14, 25, 45, 47, 127, 128, 129], with formate as a product that is of significant value for various industrial uses, e.g. as a fuel in direct fuel cells or for the synthesis of pharmaceutical and crop protection products, to name but a few [130, 131, 132]. CMD results are compared to a previous AIMD study of water structures on lead [57]. Performing these studies serves two goals: (1) testing whether IFF-based CMD simulations could reproduce results of AIMD simulations and (2) testing the importance of time- and length-scales beyond those permitted by AIMD for the sampling of thermalized water structures at interfaces.

## 3.2    Computational Details

### 3.2.1    Classical Molecular Dynamics (CMD) Computations

CMD simulations were performed with the LAMMPS software package [133]. The interatomic interactions were described by the interface force field (IFF) developed by Heinz et al. [71] and the SPC water model [134]. The interaction cutoff distance was set to 12 Å. Initial configurations of water on 2x2, 4x4, 6x6 and 8x8 Pb(100)

surface unit cells were obtained by either DFT geometry optimization calculations (previously published or computed here) or random placement of water molecules, using the PACKMOL package [135]. More details on the configuration of water on the Pb surface will be given in the next section. MD simulations of a single water layer were performed at a temperature of 140 K under NVT conditions, using a timestep of 1 fs and a Nose-Hoover thermostat with temperature dumping parameter of 100 fs. This temperature was selected because it represents the desorption temperature of a single water layer [50] and was applied in the reference AIMD simulations [57]. For multiple water layers we performed CMD simulations at ambient temperature (300 K). In order to fully equilibrate the simulated systems, we produced 1000 ps long trajectories.

## 3.2.2 Density Functional Theory (DFT) Computations

Periodic DFT calculations of the 2x2 Pb(100) surface were performed using the Quantum-ESPRESSO package [136]. In order to allow direct comparison of our results with the DFT-AIMD study of Lin et al. [57], which we call here reference data (RD), we initially applied a similar computational setup with the PBE exchange correlation functional [137] and the plane wave cut-off energy of 50 Ry. We notice that our value is larger than the value of 30 Ry that had been used by Lin et al. [57], but we found that the higher value is required to assure proper convergence of the electronic ground state energy. This difference may be a reason for some disagreements between our results and those of Lin et al. [57], which we discuss in Section 3.3.1. The projector augmented wave (PAW) method was used to describe the core electrons [138]. The 2x2 Pb(100) surfaces represented by a five-layers slab were created using the atomic simulation environment (ASE) [139]. To preserve the bulk-like environment, the two bottom Pb layers were kept fixed during the geometry optimization, while the other three layers were allowed to relax. A 20 Å vacuum space was created between the periodically repeated slabs to avoid any undesired interactions between them. A Monkhorst–Pack [140] 4x4x1 k-point grid was used. The calculated bulk Pb lattice constant of 5.03 Å is comparable to the measured value of 4.95 Å [47], and the observed overestimation of the lattice parameter is a usual feature of the PBE exchange-correlation functional [141].

## 3.3   Results and Discussion

### 3.3.1   DFT Calculations

We constructed the initial structures for CMD simulations using standard DFT calculations. For this purpose, we performed DFT calculations with gradually increasing number of $H_2O$ molecules added on the Pb(100) 2x2 surface unit cell. The adsorption energy per water molecule, $E_{ads}$, was calculated for each configuration as,

$$E_{ads} = (E_{tot} - E_{surf} - n * E_{water,iso})/n, \tag{3.1}$$

where $E_{tot}$, $E_{surf}$ and $E_{water,iso}$ are the energies of the Pb-water system, the bare Pb(100) surface, and an isolated water molecule; $n$ is the number of water molecules. A negative value of $E_{ads}$ indicates stable adsorption.

The results for the most stable configuration with up to five surface water molecules are presented in Figure 3.1. A single water molecule adsorbs preferentially on the surface hollow site with one of its hydrogen atoms orientated toward the four-fold hollow site. The computed adsorption energy of a single water molecule is -0.09 eV, which indicates weak water-surface interaction. This is consistent with the weakly hydrophilic character of the Pb surface [142].

For $n = 2$, one of the water molecules is located near the top Pb site, while the second water molecule is located at the four-fold hollow site. The adsorption energy per water molecule is -0.22 eV, because of the stabilizing hydrogen bonding between the two water molecules. Up until this point, both water structures and adsorption energies are in good agreement with the RD study. However, when adding the third adsorbed water molecule on the Pb(100) surface, a different configuration is found. Instead of the RD isolated triangular structure, we obtained a stripe-like structure. The average distance between water molecules remains at $2.74\,\text{Å}$, which is slightly smaller than in the water dimer configuration and in good agreement with the RD. $E_{ads}$ is -0.37 eV, while Lin et al. [57] obtained a weaker adsorption energy of -0.27 eV. For a water coverage of four water molecules, we obtained a water structure that shows a decamer network ($E_{ads}$ = -0.40 eV), while RD show a stripe-like structure ($E_{ads}$ = -0.36 eV).

For a configuration with 5 water molecules we looked more closely at the difference between our water structure and that of RD (Figure 3.1(b)), as this configuration is
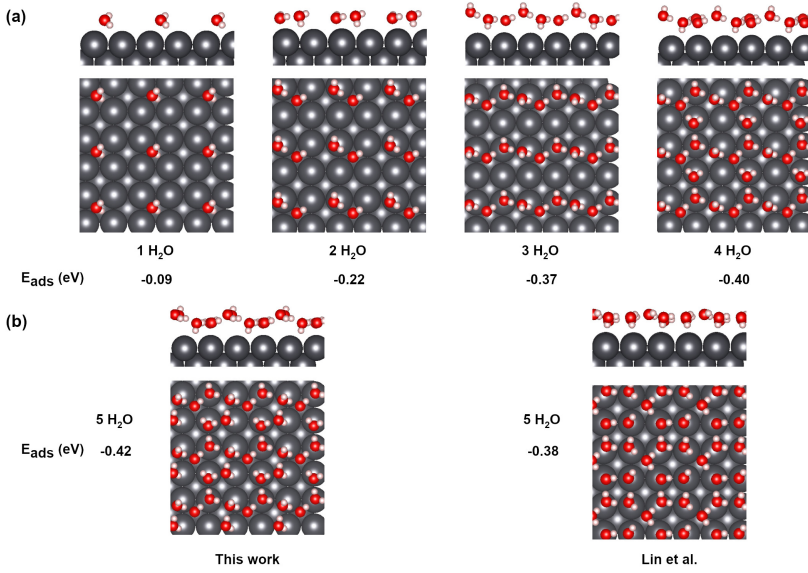
Figure 3.1: *Top and side views of the computed water structures on Pb(100) surface ranging from a water coverage (in number of* $H_2O$ *per unit surface) of (a) 1.25 to 1.00 and (b) 1.25. For comparative reasons, we also displayed the RD water structure of Lin et al. [57]. The corresponding DFT adsorption energies per water molecule are also provided. The relevant adsorption energies computed with the IFF are compared to the reported DFT values in Table S9. Red, white and grey colors mark oxygen, hydrogen and lead atoms, respectively.*

later used as the initial configuration for the classical MD simulations. While RD show a water network consisting of rectangles and distorted hexagons, our water structure consists of a mixture of pentamers and nonamers. We replicated the RD structure and compared it to our most stable structure. In addition to the different water network, the adsorption energy of our structure is $E_{ads} = -0.42\,\mathrm{eV}$, while our calculations of the RD structure gave a slightly smaller adsorption energy of $-0.38\,\mathrm{eV}$. The difference in $E_{ads}$ can be explained by the larger number of hydrogen bonds in our water network (6 hydrogen bonds per unit cell) than in the RD network consisting of rectangles and distorted hexagons (5 hydrogen bonds per unit cell). In the analysis we assumed formation of hydrogen bonding when the intermolecular O-H distance is smaller than 2.1 Å. The configurations with 6 or more water molecules could not be

stabilized, with additional molecules being pushed up out of the surface water layer. The corresponding water adsorption energies computed with the IFF for all the cases discussed above are provided in Table 3.1. These are very similar to the reported

Table 3.1: *Adsorption energy per $H_2O$ molecule for different no. of $H_2O$ molecules on the 2x2 Pb(100) surface computed with IFF and DFT (Water configurations are illustrated in Figure 3.1). Adsorption energies are calculated according to Equation 5.18 of the paper.*

| No. of $H_2O$ | Adsorption energy per $H_2O$ molecule [eV] | |
|---|---|---|
| | IFF | DFT |
| 1 $H_2O$ | -0.15 | -0.09 |
| 2 $H_2O$ | -0.32 | -0.22 |
| 3 $H_2O$ | -0.40 | -0.37 |
| 4 $H_2O$ | -0.45 | -0.40 |
| 5 $H_2O$ (Lin et al.) | -0.43 | -0.38 |
| 5 $H_2O$ (This work) | -0.50 | -0.42 |

DFT values and both sets of results show an identical trend with increasing number of water molecules.

To summarize our *ab initio* investigation, we have observed some differences from RD studies [57] for local stable water network configurations using unit cells with 3, 4 and 5 water molecules. This led us to two different initial configurations for classical MD simulations, which shows that it is not trivial to find a correct water structure with the applied *"by hand"* method. In that respect, MD simulations could be valuable for finding an equilibrium water structure. We thus selected the two obtained structures at $n = 5$ (ours and RD) as the initial structure for CMD simulations of a full water monolayer on the Pb(100) surface.

### 3.3.2   CMD Simulations of Single Water Layer

To evaluate the feasibility of IFF-based CMD for the investigation of water structures on the Pb(100) surface, we selected the two water structures with $n = 5$, computed with DFT as the initial configurations (ours and RD, see Section 3.3.1). As CMD allows for much longer simulation times than AIMD, we ran simulations for 1000 ps (compared to 8 ps AIMD runs [57]). We will show that such a long simulation time is necessary to ensure well equilibrated surface water structures. The CMD simulation results are presented in Figure 3.2 and Figure 3.3.   Using the RD water
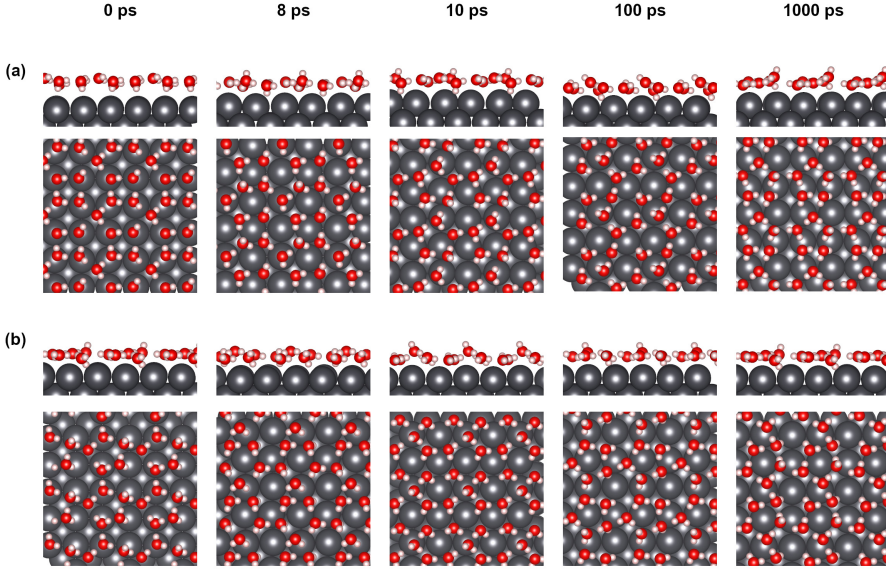
*Figure 3.2: Snapshots of CMD simulations of single water layer on Pb(100) surface using (a) RD structure [57] and (b) our DFT structure as initial conditions, in side and top views at different time steps. The water coverage is 1.25/unit surface. Red, white and grey colors represent oxygen, hydrogen and lead atoms, respectively.*

structure as the initial configuration, we obtained a good agreement between CMD simulations and the AIMD data. At 8 ps, AIMD and CMD simulations show a water network consisting of rectangles and distorted hexagons (Figure 3.2 (a)). This water network comprises of one H-up water (one hydrogen of the water molecule pointing away from the surface) and one H-down water (one hydrogen of the water molecule pointing towards the surface). However, detailed analysis of the structural evolution along the MD trajectory, as represented by Figure 3.3(a) (and related Figures 3.3 (b)-(d) obtained from simulations with larger surface cells) clearly shows that 8 ps is too short to ensure equilibration; the equilibrium is reached only after a few hundred picoseconds. Thus, the water network that consists of rectangles and distorted hexagons transformed substantially after short simulation time. At 10 ps, a network consisting of pentamers and nonamers formed, agreeing well with our DFT-based initial configuration (Figure 3.2 (b)). While the water network of pentamers and
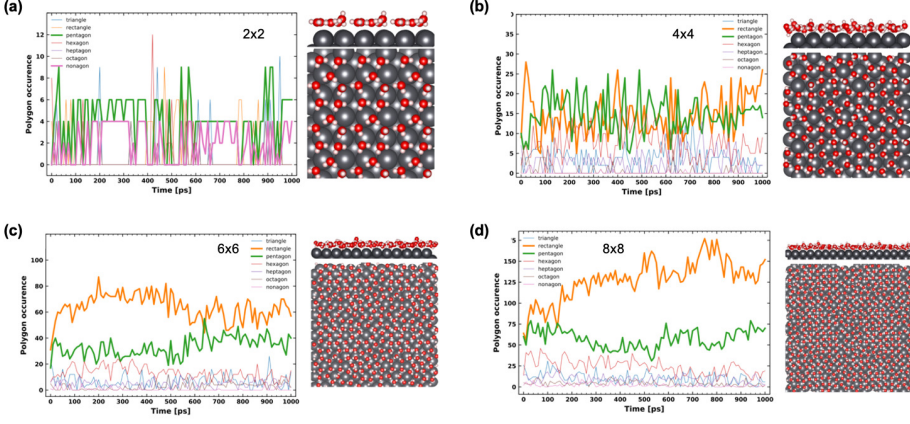
Figure 3.3: *The time evolution of the polygon water structure on Pb(100) surface for a) 2x2 b) 4x4 c) 6x6 and d) 8x8 surface size. The two most frequently detected polygons are marked with thick lines. The examples of most frequent water structure configuration for the corresponding surface sizes are shown on the right figures. The code used to detect polygons is that from [143].*

nonamers transforms into a more disordered structure at 100 ps, it is restored at 1000 ps. The time evolution (Figure 3.3(a)) shows that this structure is dominant, with an occurrence level at $\sim 50\%$ (Table 3.2). Thus, based on these findings we conclude the following: (1) CMD simulations are capable of recreating the same water structure as the AIMD simulations at the same simulation time scale, (2) a few ps long AIMD simulations are not sufficient to attain equilibrated water structures and (3) our DFT-based water structure closely resembles the final structure obtained with CMD at 1000 ps.

In order to test further the thermal stability of the proposed structure, we ran the CMD simulations taking our DFT-based structure as the initial configuration. Figure 3.2 (b) shows snapshots of classical MD simulations for this case. After 1000 ps the initial structure was preserved, indicating its stability. Interestingly, at 10 ps we observe a transition from the mixed pentamer and nonamer water structure to a rectangular and distorted hexagonal water network (i.e., the RD structure). This indicates that the RD water network is an intermediate or a metastable state. The analysis of the structural evolution along the entire CMD trajectory indicates that such a structure occurs with a probability of only 8% (Table 3.2). This is a

consequence of the energy difference (0.04 eV) between the two structures (Figure 3.1(b)), as already discussed in the previous section.

Table 3.2: *Statistical occurrence of different water network polygons at the Pb(100) surface simulated with single water layer and different surface unit cells. Analysis was performed on equilibrated parts of trajectory (from 500ps to 1000ps). The most frequently occuring polygons are marked in bold. The errors are computed as standard error of the mean (confidence level of 68%).*

| Surface size | Relative occurrence of polygons [%] | | | | | | |
|---|---|---|---|---|---|---|---|
| | Triangle | Rectangle | Pentagon | Hexagon | Heptagon | Octagon | Nonagon |
| 2x2 | $4.8 \pm 1.9$ | $8.0 \pm 2.5$ | **$39.5 \pm 4.0$** | $4.0 \pm 2.3$ | $0.0 \pm 0.0$ | $8.0 \pm 2.8$ | **$35.7 \pm 4.4$** |
| 4x4 | $5.5 \pm 0.6$ | **$28.5 \pm 1.4$** | **$33.8 \pm 1.1$** | $19.0 \pm 1.4$ | $11.2 \pm 1.4$ | $1.5 \pm 0.5$ | $0.5 \pm 0.3$ |
| 6x6 | $3.6 \pm 0.4$ | **$41.2 \pm 0.8$** | **$32.1 \pm 0.9$** | $11.3 \pm 0.6$ | $6.0 \pm 0.5$ | $5.2 \pm 0.5$ | $0.6 \pm 0.2$ |
| 8x8 | $2.4 \pm 0.2$ | **$52.3 \pm 0.8$** | **$26.3 \pm 0.7$** | $10.2 \pm 0.5$ | $5.5 \pm 0.4$ | $2.0 \pm 0.2$ | $1.3 \pm 0.2$ |

We also ran CMD simulations using a random initial water configuration generated with the aid of PACKMOL package (see Figure 3.4). Even starting with a random
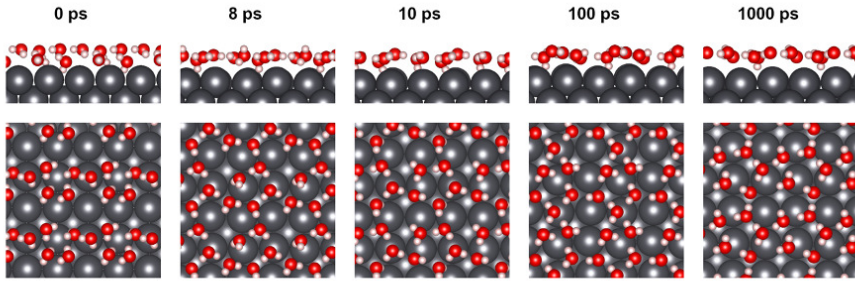


Figure 3.4: *Snapshots of classical MD simulations of water layers on Pb(100) surface using random structure generated through PACKMOL in side view and top view at different time steps. The water coverage is 125% (5 H$_2$O) per 2x2 surface.*

initial water configuration, after 1000 ps we obtained a mixed pentamer and nonamer water structure. This observation strengthens our finding that the mixed pentamer and nonamer network is the most stable water structure in the equilibrium state at the 2x2 surface unit cell.

To further quantify the differences in the obtained water structures, we analyzed the distance of the water layer to the Pb(100) surface as presented in Table 3.3. The

first row in Table 3.3 ("DFT") represents the stable water structure obtained in our DFT calculation (Figure 3.2 (b) at 0 ps). The first oxygen atom is located at $3.34\,\text{Å}$ above the Pb surface, while the maximum Pb-O distance is at $4.51\,\text{Å}$. Optimization with the IFF, initialized with that structure, places the water layer in closer proximity to the surface, with the Pb-O distance ranging from $2.55\,\text{Å}$ to $3.38\,\text{Å}$.

*Table 3.3: Comparison of first layer water molecules-Pb(100) surface distance simulated with the 2x2 surface unit cell using different computational methods. The first two rows show results for water configurations obtained with DFT and DFT+D3 (dispersive corrections). The last row shows the result for the water structure arrived at via IFF optimization that started from an initial geometry optimized by DFT.*

| Computational method | Range of Pb-O distance $[\text{Å}]$ | Average Pb-O distance $[\text{Å}]$ |
|:---:|:---:|:---:|
| DFT | 3.34 - 4.51 | 3.81 |
| DFT + D3 | 3.20 - 4.21 | 3.63 |
| IFF (DFT) | 2.55 - 3.38 | 3.09 |

From our analysis of the water-metal distance we conclude that, even though we are able to find identical water structures in MD and DFT calculations (mixed pentamers and nonamers water structure), the Pb-O distances found with the IFF differ significantly from those found with DFT. It is known that adding dispersion correction to DFT may be crucial to assure the stability of water structures on metal surfaces [144]. However, adding dispersion corrections in our case ("DFT + D3") does not change the structure of the water network (Figure 3.5). Adding dispersion correc-
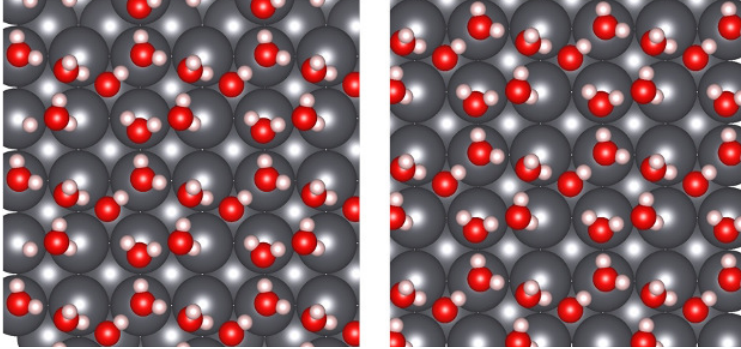


*Figure 3.5: DFT optimized water structures without D3 corrections (left) and with D3 corrections (right) on the 2x2 Pb(100) surface. Both structures show a pentagonal and nine-fold water network indicating a negligible effect of dispersion corrections.*

tions shift the Pb-O distances slightly to lower values (Table 3.3), yet not enough to reconcile CMD and DFT Pb-O distances. The main reason for the deviation between our IFF-based and DFT simulations is an inadequate or incomplete description of water-surface interactions. Berg et al. [117] and Steinmann et al. [70] discussed the difficulty of the IFF to correctly capture the Pb-H interactions. Polarization effects, which are crucial for the correct description of metal surface-adsorbate interactions [145], are not accounted for in the IFF applied here. Nevertheless, the water structure is determined mainly by the applied water model and the distribution of surface Pb atoms is determined by the lattice parameter, to which water layer tries to accommodate. It should not be affected by the strength of direct interactions between surface atoms and water molecules, which determines mainly the distance of the water layer from the surface.

### 3.3.3 Surface Size Effect of Water Structure on Pb(100) Surface

Another aspect that we test here is the effect of the size of the surface cell model on water structures at the Pb(100) surface. For larger surface cells, we have to resort to CMD simulations since the AIMD approach becomes prohibitively expensive. Figure 3.6 shows geometry snapshots at different CMD timeframes for 4x4, 6x6 and 8x8 surface unit cells, using as the initial water structure the configuration obtained with the 2x2 surface unit cell model (Figure 3.2 (b) at 0 ps). For all three surface sizes, we observe a quick destabilization of the mixed pentamer and nonamer water structure. Interestingly, no ordered structure is obtained after 1000 ps in all the cases. Instead, a large cavity is formed, indicating that more water molecules are needed for a full first water layer. The cavity can be easily filled out with additional water molecules, which indicates more denser water layer than the one obtained when simulating the 2x2 surface.

To derive such a structure, we filled up the water cavity with additional water molecules until a full monolayer of $H_2O$ is formed. The procedure we applied to fill up the water cavity is described in more detail in Figure A.1 in Appendix A. After filling up the first water layer, we ran CMD simulations to equilibrate the structures. Figure 3.7 shows the variation of the water density along the normal to the Pb surface for the computed surface unit cells. It is evident that in case of the
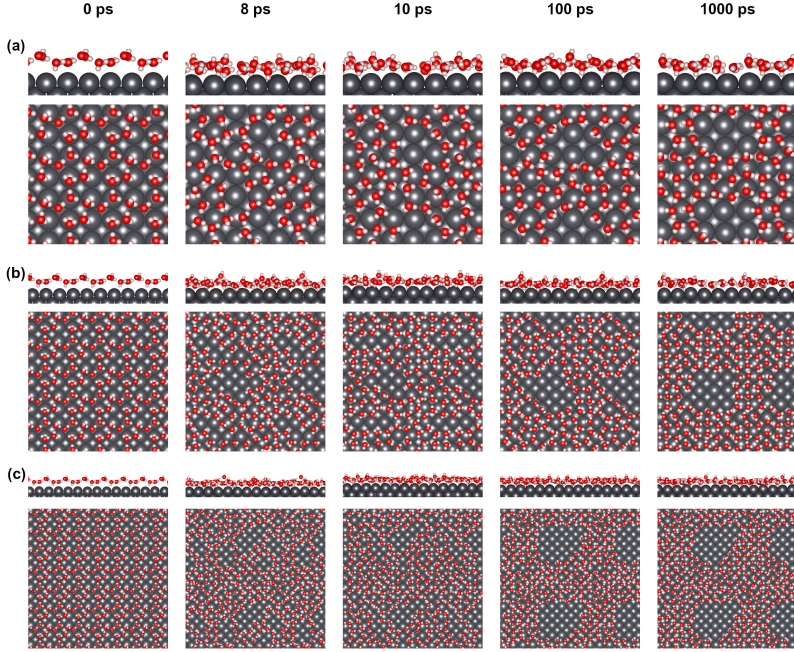
*Figure 3.6: Snapshots of CMD simulations of single water layer simulated with the (a) 4x4, (b) 6x6 and (c) 8x8 Pb(100) surface unit cells, in side and top views at different time steps. The water coverage for all configurations is 1.25/unit surface. Red, white and grey colors represent oxygen, hydrogen and lead atoms, respectively.*

2x2 surface unit cell the first density peak (at 3 Å) is sharper and shifted slightly to the left, as compared to the broader peaks obtained for larger simulated surface cells. The sharper peak indicates overstructuring of the water layer. It is clear that for a realistic description of water structures, at least a 4x4 surface unit cell should be used. Table 3.4 compares the number of $H_2O$ molecules in the first layer for each surface configuration. We found that the 4x4, 6x6 and 8x8 structures incorporate $\sim 1.5$ $H_2O$ molecules/unit surface area, while the 2x2 surface unit cell allows for only 1.25 $H_2O$ molecules/unit surface area. This shows a clear limitation of using the small 2x2 surface unit cells for investigation of water structure on metal surfaces.
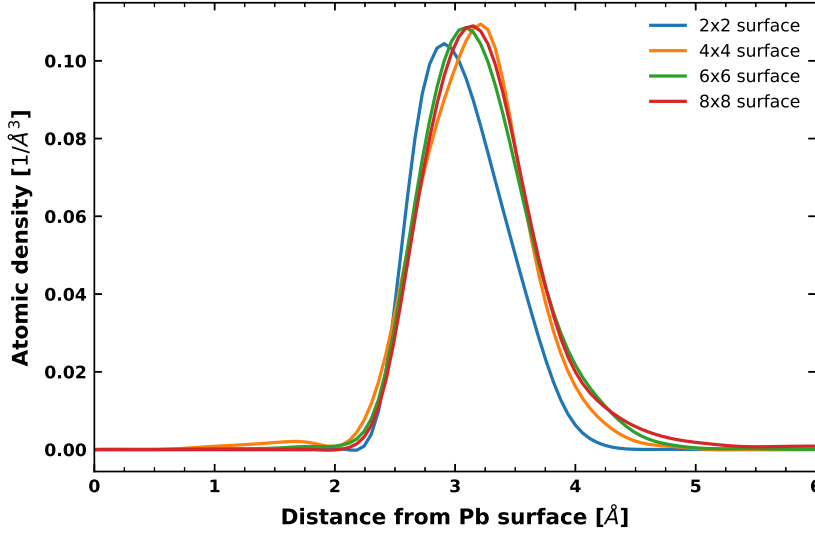
Figure 3.7: *Water density distribution of first layer $H_2O$ molecules on Pb(100) surface obtained with 2x2, 4x4, 6x6 and 8x8 surface unit cells. The results are from simulations of single water layer.*

Table 3.4: *Number of $H_2O$ molecules (per surface unit cell) in the surface water layer at Pb(100) for different surface unit cells. A single water layer was considered.*

| Surface size | No. of $H_2O$ molecules |
|:---:|:---:|
| 2x2 | 1.25 |
| 4x4 | 1.56 |
| 6x6 | 1.56 |
| 8x8 | 1.53 |

### 3.3.4 CMD Simulations of Thick Water Slab

In order to obtain the most realistic water structure we filled up the entire vacuum space with $H_2O$ molecules and ran the MD simulations at a temperature of 300 K. We fixed the water density to 1 g/L for all simulations. Figure 3.8 shows the obtained atomic density profile for oxygen along the normal to the Pb surface.

As in simulations with a single water layer, we observe a slight deviation of the wa-

46

Figure 3.8: *Water density distribution obtained with different surface unit cells for the Pb(100) surface. The results are from simulations with thick water slab.*

ter density profile obtained with the 2x2 surface unit cell. While there is a good agreement in the height and location of first peak (at $\sim 3\,\text{Å}$), the second peak is slightly higher. In addition, the remaining peaks are on average much more "sharp-edged" than the density profiles obtained with larger surface unit cells show. This strengthens the argument that the 2x2 surface is too confined for simulations of "realistic" water structures. Nevertheless, the water density profiles are in good agreement with the density profiles at water-metal interfaces found in other simulations [73, 117, 145]. Table 3.5 shows the obtained density in the first layer of water molecules.

For all surface cell sizes the number of first layer water molecules per surface unit cell is very similar ($\sim 1.5$), and consistent with that obtained from the single layer studies with large surface cells (Table 3.4). Results of the statistical analysis of structural evolution of the surface water layer are provided in Table 3.6. It qualitatively resembles the one obtained with a single water layer and shows the appearance of rectangle-pentagon structure. This validates the computational approaches that employs a surface water layer to simulate the effect of surface hydration [107, 123].

Table 3.5: *Comparison of the number of first layer $H_2O$ molecules at Pb(100) surfaces obtained from simulations of different surface unit cell sizes. The results are from simulations with thick water slab.*

| Surface size | No. of $H_2O$ molecules |
|:---:|:---:|
| 2x2 | 1.52 |
| 4x4 | 1.48 |
| 6x6 | 1.48 |
| 8x8 | 1.45 |

Table 3.6: *Statistical occurrence of different water network polygons at Pb(100) surface simulated with thick water slab at different surface unit cells. Analysis was performed on equilibrated parts of trajectory (from 500ps to 1000ps). The most frequently occuring polygons are marked in bold. The errors are computed as standard error of the mean (confidence level of 68%).*

| Surface size | Relative occurrence of polygons [%] | | | | | | |
|:---:|:---:|:---:|:---:|:---:|:---:|:---:|:---:|
| | Triangle | Rectangle | Pentagon | Hexagon | Heptagon | Octagon | Nonagon |
| 2x2 | $8.5 \pm 3.5$ | $5.9 \pm 2.6$ | **$46.7 \pm 6.8$** | $0.0 \pm 0.0$ | $0.0 \pm 0.0$ | $1.7 \pm 1.8$ | **$37.2 \pm 6.8$** |
| 4x4 | $9.4 \pm 1.0$ | **$16.9 \pm 1.2$** | **$24.7 \pm 1.7$** | **$21.2 \pm 1.5$** | $12.0 \pm 1.2$ | $6.6 \pm 1.0$ | $9.2 \pm 1.2$ |
| 6x6 | $9.5 \pm 0.6$ | **$17.3 \pm 0.8$** | **$27.5 \pm 1.2$** | **$20.7 \pm 1.0$** | $11.0 \pm 0.8$ | $6.8 \pm 0.5$ | $7.2 \pm 0.7$ |
| 8x8 | $8.1 \pm 0.4$ | **$17.1 \pm 0.6$** | **$25.7 \pm 0.7$** | **$19.3 \pm 0.7$** | $11.5 \pm 0.6$ | $9.6 \pm 0.5$ | $8.7 \pm 0.6$ |

### 3.3.5    CMD Simulations of Water Structure on Pb(111)

We have conducted CMD simulations with a single layer of $H_2O$ and the cell filled completely with $H_2O$ of 1g/L density for the Pb(111) surface. Comparison of the equilibrated water layer structures at Pb(111) and Pb(100) surfaces reveals the formation of a water bilayer on the Pb(111) surface, which was not seen at Pb(100). This agrees with the RD [57]. As illustrated in Figure 3.9, in the case of the inter-slab space completely filled with water, the density profile of water on the Pb(111) surface shows some differences in the height of the first two peaks compared to the Pb(100) surface. The first peaks are more pronounced in the case of the Pb(111) surface, indicating the greater distance between first two water layers. This was also observed in the RD AIMD simulations [57]. Furthermore, the interfacial density of $H_2O$ varies between both Pb surfaces, with the Pb(100) and Pb(111) surfaces having the surface water layer density of 1.50 and 1.25 per unit surface, respectively. In general, the Pb(111) surface exhibits a weaker Pb-water interaction than the Pb(100) surface, which is consistent with AIMD RD [57].
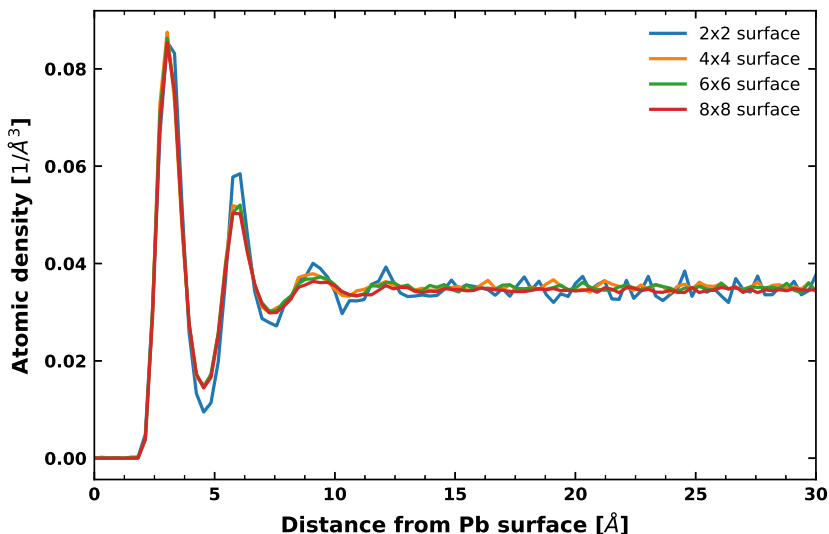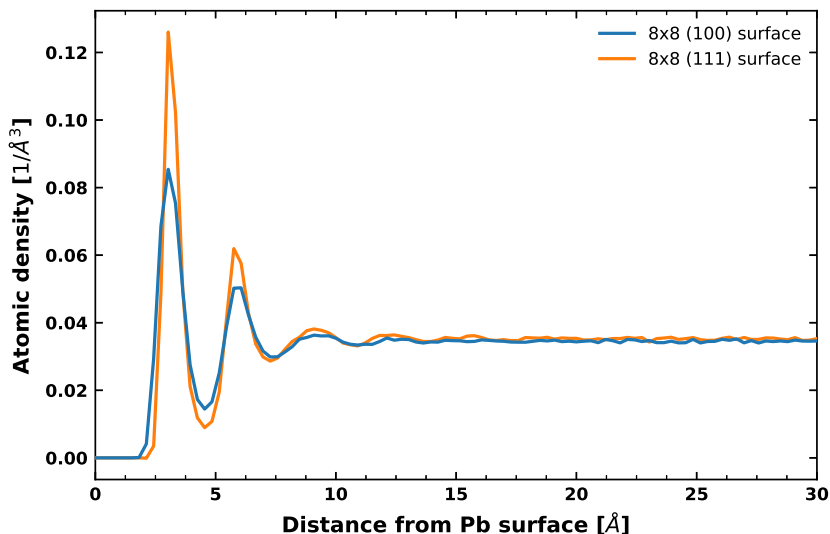
Figure 3.9: *Water density distribution obtained with 8x8 surface unit cell for the Pb(100) and Pb(111) surfaces. The results are from simulations with thick water slab.*

## 3.4 Summary

With the IFF-based CMD simulations we have performed a comprehensive investigation of water structures on the Pb(100) and (111) surfaces and found water structures that are consistent with those obtained with AIMD simulations, when applying similar simulation time and length constrains. However, we found that the limited simulation time (up to a few ps) and small surface unit cells permitted by AIMD simulations cannot guarantee obtaining equilibrated water structures. We obtained well-equilibrated water structures with much longer CMD simulations (ns and longer vs. ps) and noticed that at least 4x4 surface unit cells must be used to produce realistic water structures. We observed that the water-equilibrated Pb(100) and (111) surfaces have 1.50 and 1.25 water molecules per unit surface, respectively. On the other hand, although the IFF can correctly capture the water structure, the water-surface distance is significantly underestimated due to an incomplete description of metal-adsorbate interactions. Nevertheless, the fact that the surface water structure

49

can be correctly reproduced by IFF is an important result, given the superior computational efficiency of CMD as compared to the AIMD approach, which is a crucial factor for realistic equilibration and statistical sampling.

# Chapter 4

# Impact of Solvation Phenomena on the $CO_2$ Reduction Reaction at Pb(100) and Ag(100) Surfaces

**Note:** Since the following chapter is based on the publication "O. Cheong, T. Born-hake, X. Zhu, M. H. Eikerling, Stay hydrated! Impact of solvation phenomena on the $CO_2$ reduction reaction at Pb(100) and Ag(100) surfaces, ChemSusChem, e202300885 (2023)", the personal pronoun "we" is used throughout this chapter to refer to the group of researchers that were part of this specific study. In this study, all calculations and analyses were performed by me, with the exception of the microkinetic simulation performed by Xinwei Zhu. Thomas Bornhake provided assistance during the DFT calculations, while Michael H. Eikerling took on a supervisory role throughout this project.

In this chapter, we continue the study of solvation on metal surfaces with the additional consideration of the $CO_2$ reduction reaction. We have performed a comprehensive computational study of the impact of solvation on the reduction reaction of $CO_2$ to formic acid (HCOOH) and carbon monoxide (CO) at Pb(100) and Ag(100) surfaces. Results further the understanding of how solvation phenomena influence the adsorption energies of reaction intermediates, highlighting the significant impact of explicit solvation. We applied the explicit solvation scheme using a combined density functional theory (DFT)/microkinetic modeling approach for the $CO_2$ reduction reaction. This approach reveals high selectivities for CO formation at Ag and HCOOH

formation at Pb, successfully reconciling the disparity between *ab initio* calculations and experimental observations. Applying IFF-based CMD simulations, as introduced in Chapter 3, in combination with subsequent DFT calculations, we assess the degree of "uncertainty" that comes along with introducing explicit solvation effects. Furthermore, the detailed analysis of adsorption energies of relevant reaction intermediates shows that the total number of hydrogen bonds formed by HCOO play a primary role for the adsorption strength of intermediates and the electrocatalytic activity. Results emphasize the importance of explicit solvation for adsorption and electrochemical reaction phenomena on metal surfaces.

## 4.1   Introduction

As stated in Chapter 3, for realistic atomistic simulations of electrochemical reaction at electrode/electrolyte interfaces, it is of utmost importance to account for solvation phenomena involving chemisorbed reaction intermediates. These phenomena can have a significant impact on the energetics of different reaction pathways [43, 44, 46, 47]. Different approaches to treat solvation on metal surfaces have been considered in the past, ranging from implicit over explicit to hybrid solvation models [43, 44, 46, 47, 54, 72, 73, 74, 106, 146, 147, 148, 149, 150, 151, 152]. Implicit solvation models treat the solvent as a polarizable continuum and thereby minimize computational cost. However, recent studies have shown that H-bonding in the vicinity of solvated reaction intermediates play a crucial role in the stabilization of adsorbates [44, 73, 74]. Heenen et al. [73] compared adsorption energies of several adsorbates on different metal surfaces obtained using an implicit treatment of solvation effects with adsorption energies calculated from *ab initio* molecular dynamics (AIMD) simulations. They found that the adsorption energies derived by the continuum solvation method and AIMD simulations differed by up to 0.6 eV. Furthermore, they found no significant improvement of computed adsorption energies compared to vacuum calculations when the implicit solvation scheme was applied.

Explicit solvation models can be divided into static and dynamic approaches. Within the realm of static water approaches, the number of water molecules considered explicitly ranges from several molecules [44, 74, 150] to static ice-like water bilayers [49, 51]. An alternative microsolvation approach, proposed by Rendon-Calle et al. [106], involves quantifying the required number of water molecules in the first

solvation shell of adsorbates by taking into account the additional stabilization of hydrogen bonding interactions with the adsorbate. This approach predicted onset potentials of CO$_2$ reduction reactions to CO, CH$_4$, and CH$_3$OH on Cu, Ag, Au, and Zn, in reasonable agreement with experimental values. However, the main challenge of static microsolvation approaches is the difficulty to identify a representative structure from the vast number of configurations possible within the adsorbate-solvent system as well as the negligence of solvation effects that extend beyond the first solvation shell of the adsorbate. Even if we adapt the convenient static hexagonal ice-like water layer, the transferability of these static structures becomes more difficult when accounting for surface facets other than (111) and metal lattice parameters that deviate from those of the frequently investigated Cu or Pt.

Explicit dynamic approaches such as classical MD (CMD) and AIMD can overcome the lack of sufficient statistical sampling of relevant configurations. However, AIMD simulations lack the computational efficiency to sample a sufficient number of configurations over a long enough time scale [59, 60, 153]. On the other hand, CMD simulations of water structures on metal surfaces rely on the accurate parametrization of force fields [70, 117, 153]. Hybrid approaches such as the quantum-mechanical/molecular mechanics (QM/MM) method, in which surface-adsorbate interactions are described at the quantum mechanical level and adsorbate-solvent interactions are modeled using classical molecular mechanics, have yielded promising results for the calculation of adsorption energies of benzene and phenol at the Pt(111)/water interface for which experimental data are available to compare with [72]. As this approach also relies on the force field parameters for adsorbate-solvent and solvent-surface interactions, it can be stated that while a lot of research works of different solvation approaches on metal surfaces have been published, there is still no consistent approach to treating solvation of adsorbates on metal surfaces. Specifically, there is still no clear guidance on how to account for explicit solvation in the CO$_2$ reduction reaction.

In the latter context, Pb is a promising electrocatalyst for CO$_2$ reduction [9, 10, 127, 129] to formic acid (HCOOH), which has many uses in the fields of fuel cells, pharmaceuticals and crop protection [130, 131, 132], while CO$_2$ reduction at Ag mainly produces CO, which serves as an industrial feedstock for a wide range of chemicals [154]. While it has been experimentally shown that CO$_2$ reduction generates mostly HCOOH on Pb catalyst and CO on Ag catalyst [10, 27, 47, 155], these

experimental observations have so far not been demonstrated conclusively with *ab initio* simulations [25]. DFT calculations *in vacuo* allow for fast screening of selective catalytic materials [25, 27, 34, 156]. However, in the case of CO$_2$ reduction to HCOOH or CO, solely evaluating the adsorption energies of reaction intermediates *in vacuo* can be insufficient to correctly predict product selectivities. In particular, adsorption energy calculations of Yoo et al. [25] have suggested that HCOOH is the main product for CO$_2$ reduction on both Ag and Pb surfaces, contradicting experimental results. In recent years, there have been several attempts to resolve this Ag/Pb selectivity issue [157, 158, 159, 160]. Morrison et al. [157] have tried to explain the selectivity for CO formation on Ag and HCOOH formation on Pb by coverage-dependent adsorption energies of HCOO and COOH intermediates. Other computational works based on DFT found CO to be the main product during CO$_2$ reduction on Ag. These conclusions were reached with different reasoning: (1) based on the inclusion of lateral interactions of reaction intermediates [158], (2) based on the discovery of new reaction intermediates [159] and (3) based on the incorporation of one extra solvent molecule [160]. However, it remains unclear whether the aforementioned explanations can be extended to HCOOH-selective catalytic materials such as Pb. We thus expect that further refined consideration of solvation effects for the CO$_2$ reduction reaction on both Pb(100) and Ag(100) surfaces could improve the consistency with experimental findings.

Realizing the lack of understanding of solvation effects during reaction energy calculations, we provide comprehensive insights into how different solvation approaches affect adsorption energies of certain reaction intermediates as well the overall CO$_2$ reduction reaction pathway towards HCOOH or CO on Pb(100) and Ag(100) surfaces. We combine our DFT calculations with microkinetic modeling to re-evaluate product selectivities of the CO$_2$ reduction reaction on Pb(100) or Ag(100) surfaces. Based on these results, we follow up with an examination of various critical aspects of the explicit solvation approach by carrying out an uncertainty analysis for the explicit solvation effect of reaction intermediates HCOO or COOH on Pb(100). Additionally, we explore crucial properties that affect the adsorption energy of these reaction intermediates.

## 4.2   Computational Details

### 4.2.1   Density Functional Theory (DFT) Computations

Density functional theory (DFT) calculations were performed for different adsorbates on Pb(100) and Ag(100) slabs using periodic boundary conditions with the PBE exchange correlational functional [137] in the Quantum-ESPRESSO package [136]. We used the projector augmented wave (PAW) method for the core electrons [138]. The plane wave cutoff energy was set to 50 Ry. We used the atomic simulation environment (ASE) to create 3x3 surfaces represented by five-layer slabs [139]. The two bottom layers were kept fixed during the geometry optimization, while the other three layers were allowed to relax. In order to avoid undesired interactions between periodically repeated slabs a 20 Å vacuum space was inserted between them. A Monkhorst–Pack [140] 4x4x1 k-point grid was used for structure relaxations. The calculated lattice constants of bulk Pb and Ag are 5.03 Å and 4.15 Å, respectively, which are comparable to the measured values of 4.95 Å for Pb [47] and 4.09 Å for Ag [161]. Explicit solvation structures were modeled using up to 12 explicit water molecules and implicit solvation calculations were performed with the soft-sphere continuum solvation (SSCS) approach using the Environ software package [100, 162]. During implicit solvation calculations, we assumed a dielectric constant of $\epsilon$=80 for the bulk solvent value. A hybrid solvation approach was also applied by adding implicit solvation on top of the optimized explicit water configurations.

Adding dispersion corrections, using for instance the D3 dispersion correction scheme of Grimme [96, 163], can correct for the over-structuring of water molecules in the bulk environment typically seen with the PBE functional [164]. On the other hand, dispersion effects have a negligible impact on the relative stability, adsorption sites, and adsorption geometries of water adstructures [165, 166]. Romeo et al. [167] have additionally shown that dispersion corrections are generally not needed when water-adsorbate interactions are predominant. To assess the need of dispersion corrections for our given system, we have incorporated additional calculations that include D3 dispersion corrections.

## 4.2.2 Classical Molecular Dynamics (CMD) Computations

CMD simulations to sample explicit water molecules on Pb surface were performed with the LAMMPS software package [133]. The interatomic interactions were described by the interface force field (IFF) Heinz et al. [71] and the SPC water model [134], similar to Chapter 3. The interaction cutoff distance was set to 12 Å and initial water molecule configurations on the Pb(100) surface were obtained by random water molecule placement using the PACKMOL package [135]. MD simulations were performed under NVT conditions at a temperature of 300 K, with a timestep of 1 fs and a Nose-Hoover thermostat with a temperature damping parameter of 100 fs.

## 4.2.3 Explicit Solvation Configuration Setup

Regarding the representative configuration used for the case of 1-12 explicit H$_2$O molecules, we initially generated and conducted geometry optimizations of 5 different random configurations for the case of 1 explicit H$_2$O molecule. We selected the most energetically stable configuration as the representative structure for the case with 1 explicit H$_2$O molecule. For the case of 2 explicit water molecules, we used the most energetically stable configuration with 1 explicit H$_2$O molecule as a basis to generate and optimize 5 further different random configurations. This procedure, as illustrated in Figure 4.1, was repeated up until 12 explicit water molecules have been added at the Pb(100) surface, which is approximately the amount of water molecules needed to form the first interfacial water layer [57]. Even though the described water configuration generation procedure does not sample the whole configurational space, this so-called "brute intuition" approach, originally mentioned by Peterson [168], to finding local minimal energy configurations follows a simple and reproducible protocol. Hence, we have applied this approach to determine the local minimum configuration of adsorbate-water structures on Pb(100).

## 4.2.4 Reaction Energy Calculations

The reaction or adsorption energy for the first reaction step of CO$_2$ to HCOO$^*$ or COOH$^*$ is calculated using the relation
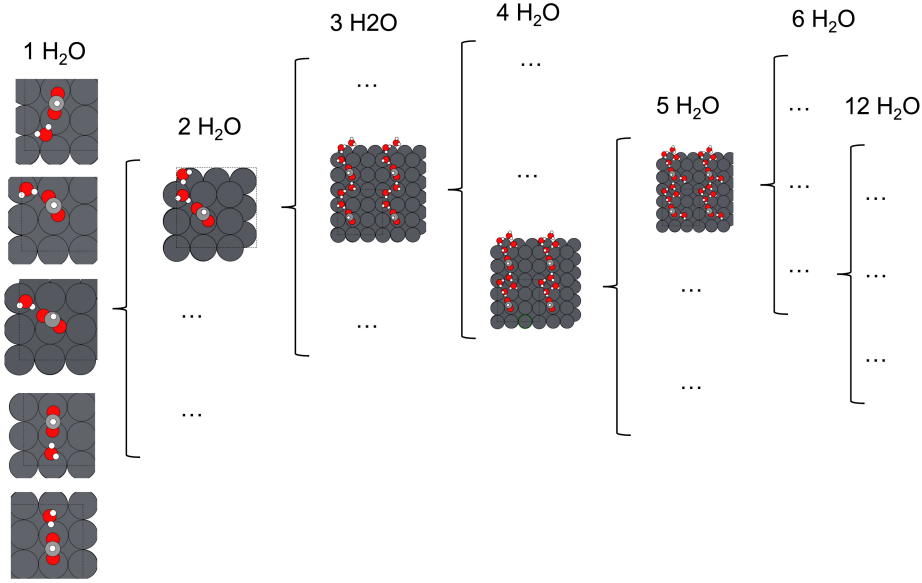
*Figure 4.1: Initialization of explicit water structures for 1-12 water molecules. Starting with one explicit water molecule, the most energetically stable configuration from geometry optimization is taken to use a basis for the initialization of two explicit water configuration. This procedure is repeated up until 12 explicit water molecules.*

$$E_{\text{ads}} = E_{\text{HCOO/COOH+surface}} - E_{\text{surface}} - E_{\text{CO}_2} - 0.5 * E_{\text{H}_2}, \qquad (4.1)$$

where $E_{\text{HCOO/COOH+surface}}$, $E_{\text{surface}}$, $E_{\text{CO}_2}$, $E_{\text{H}_2}$ correspond to the energy of adsorbed HCOO$^*$ or COOH$^*$ on the Pb(100) surface, the energy of the bare Pb(100) surface and the energies of isolated gas phase species CO$_2$ and H$_2$, respectively. In this study, the reaction energy and adsorption energy are used interchangeably, conveying the same underlying concept. According to the CHE method, the free energy of H$_2$ instead of the free energies of protons and electrons is employed.

In solvated environment, instead of the energies of adsorbed HCOO$^*$ or COOH$^*$, $E_{\text{HCOO/COOH+surface}}$, and of bare Pb(100) surface, $E_{\text{surface}}$, the energies of the solvated adsorbed HCOO$^*$ and COOH$^*$ on the Pb(100) surface, $E_{\text{HCOO/COOH+surface+nH}_2\text{O}}$, and of the solvated Pb(100) surface, $E_{\text{surface+nH}_2\text{O}}$, are included, with nH$_2$O representing

the number of explicit water molecules.

To construct reaction energy diagrams, the reaction Gibbs free energy of a electrochemical process was calculated according to the computational hydrogen electrode (CHE) method [22]. Reaction Gibbs free energy calculations include zero-point energy (ZPE) and entropic (TS) corrections, which are obtained through vibrational frequency calculations, as shown in Figure B.1 in Appendix B. The climbing image nudged elastic band (CI-NEB) method [169] with eight images was utilized to calculate the activation barriers for specific reaction steps.

### 4.2.5 Microkinetic Modeling

In the microkinetic model, the steady state rate equations for the changes of adsorbate coverages in vacuum environment are

$$\frac{d\theta_{\text{HCOO}*}}{dt} = \nu_1 - \nu_2 = 0 \tag{4.2}$$

$$\frac{d\theta_{\text{COOH}*}}{dt} = \nu_3 - \nu_4 = 0 \tag{4.3}$$

where $\theta_{\text{HCOO}*}$ and $\theta_{\text{COOH}*}$ are coverages for HCOO and COOH intermediates. $\nu_i$ is the reaction rate of the $i$-th elementary reaction step from Eq.(4.11)-(4.14) presented in the next section and is given by

$$\nu_1 = k_1 p_{\text{CO}_2} p_{\text{H}_2}^{\frac{1}{2}} \theta_0^2 - k_{-1}\theta_{\text{HCOO}*} \tag{4.4}$$

$$\nu_2 = k_2\theta_{\text{HCOO}*} p_{\text{H}_2}^{\frac{1}{2}} \tag{4.5}$$

$$\nu_3 = k_3 p_{\text{CO}_2} p_{\text{H}_2}^{\frac{1}{2}} \theta_0 - k_{-3}\theta_{\text{COOH}*} \tag{4.6}$$

$$\nu_4 = k_4\theta_{\text{COOH}*} p_{\text{H}_2}^{\frac{1}{2}} \tag{4.7}$$

with $\theta_0$ = 1 - 2$\theta_{\text{HCOO}*}$ - $\theta_{\text{COOH}*}$ being the coverage of free sites, and $p_{\text{CO}_2}$ and $p_{\text{H}_2}$ being the pressures of CO$_2$ and H$_2$, respectively. We use $p_{\text{CO}_2} = p_{\text{H}_2} = 1$ atm, corresponding to standard conditions. Rate constants, $k_{+\text{i}}$ and $k_{-\text{i}}$, are calculated

from transtion-state theory,

$$k_{\pm i} = \frac{k_b T}{h} \exp\left(-\frac{G_{a,\pm i}}{k_b T}\right) \tag{4.8}$$

where $G_{a,\pm i}$ are activation barriers of step $i$ for the forward and backward reactions obtained from our DFT calculations. $\theta_{\text{HCOO*}}$ and $\theta_{\text{COOH*}}$ can then be obtained by solving Eq.(4.2) and Eq.(4.3).

The selectivities of the two main products CO and HCOOH can then be calculated by

$$s_{CO} = \frac{\nu_4}{\nu_2 + \nu_4} \tag{4.9}$$

$$s_{HCOOH} = \frac{\nu_2}{\nu_2 + \nu_4} \tag{4.10}$$

## 4.3   Results

### 4.3.1   Solvation Effect on CO$_2$ Reduction Reaction to HCOOH or CO at Pb(100) Surface

To show the importance of solvation when evaluating electrochemical reactions, we have investigated the effect of explicit and implicit solvation on the CO$_2$ reduction reaction at the Pb(100) surface. The CO$_2$ reduction reaction on Pb(100) (also on Ag(100)) proceeds via two major pathways. Following the first pathway, CO$_2$ is transformed to HCOOH via the HCOO$^*$ reaction intermediate (Eq.(4.11)-(4.12)). The second pathway proceeds to CO and H$_2$O products via the COOH$^*$ reaction intermediate (Eq.(4.13)-(4.14)). The considered reaction pathways to form CO and HCOOH are thus given by

$$CO_2(g) + H^+ + e^- \rightarrow HCOO^* \tag{4.11}$$

$$HCOO^* + H^+ + e^- \rightarrow HCOOH(g) \tag{4.12}$$

$$CO_2(g) + H^+ + e^- \rightarrow COOH^* \tag{4.13}$$

$$COOH^* + H^+ + e^- \rightarrow CO(g) + H_2O \tag{4.14}$$
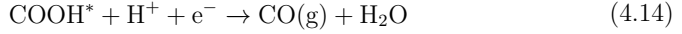
where adsorbed intermediates are indicated with $^*$.

Reaction energies for the first CO$_2$ reduction reaction step for the vacuum case and different solvation methods are summarized in Table 4.1. For the explicit solvation case, 12 explicit H$_2$O molecules have been used, equivalent to one water layer [57]. Similar calculations have been performed in our previous study [170], where instead

Table 4.1: *Adsorption energy of HCOO*$^*$, $E_{ads,HCOO}$, *and COOH*$^*$, $E_{ads,COOH}$, *on the Pb(100) surface for the vacuum case and different solvation case, including implicit, explicit and hybrid solvation case. 12 explicit H$_2$O are used for the explicit solvation case.*

| Method | $E_{ads,HCOO}$ [eV] | $E_{ads,COOH}$ [eV] |
|---|---|---|
| **Vacuum** | -0.37 | 0.75 |
| **Implicit** | -0.57 | 0.56 |
| **Explicit** | -1.11 | 0.53 |
| **Hybrid** | -1.18 | 0.48 |

the VASP [171, 172, 173] and VASPsol [101, 102] software packages had been used to perform DFT calculations in vacuum and in solvation. As observed in the previous study [170], applying implicit solvation stabilizes reaction energies of HCOO$^*$ and COOH$^*$ by around 0.2 eV relative to the vacuum case. Implicit solvation stabilizes these intermediates by an equal amount without incurring a change in their configuration relative to the vacuum case, as shown in Figure B.2 in Appendix B. Explicit solvation in the case of 12 explicit water molecules results in a different picture. HCOO$^*$ is stabilized by 0.74 eV, whereas COOH$^*$ is stabilized by only 0.22 eV in the explicit solvation environment. Overall, these results agree with our previous findings [170]. In addition to these findings, we explain the greater stabilization of HCOO$^*$ compared to COOH$^*$ by the fact that explicit water molecules have a significant impact on the orientation of HCOO$^*$ relative to the surface, as illustrated in Figure 4.2. HCOO$^*$ changes from perpendicular orientation towards the surface for vacuum and implicit solvation cases to a parallel orientation for the explicit solvation

case. COOH* on the other hand remains in perpendicular orientation for both cases. In addition, HCOO* undergoes H-bonding with four neighboring water molecules, while COOH* is only H-bonded to three neighboring water molecules. Lastly, we have found that the hybrid approach, i.e., adding implicit solvation on top of explicit solvation, incurs only a minor change in the reaction energies of the explicit solvation case, underlining the importance of including explicit water molecules for reaction energy pathway calculations.
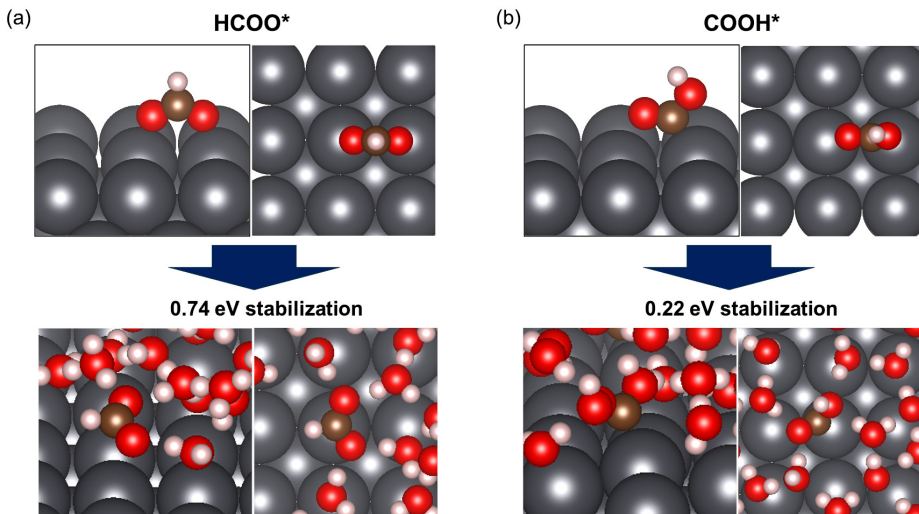


*Figure 4.2: Illustration of configurational change from vacuum to explicit solvation for (a) HCOO adsorbate and (b) COOH adsorbate on Pb(100) surface.*

In order to assess the results of our DFT calculations, Table 4.2 compares the onset potential for HCOOH formation, identified as the minimum potential required to initiate the electrochemical reaction, in the various computational set-ups used by us with the experimental HCOOH onset potential. While we observe a significant discrepancy between the experimental value and the computed values for the vacuum and implicit solvation cases, experimental and computed values are close for the explicit solvation case and even closer for the hybrid solvation case.

Realizing the importance of computing solvent effects with explicit water molecules, we have further evaluated the effect of the adsorption energies of both HCOO* and COOH* intermediates by systematically increasing the number of explicit water molecules. This gives us a more advanced understanding of how many

Table 4.2: Onset potential (V vs. RHE at pH = 0) for HCOOH formation on Pb for the vacuum case, the different solvation scenarios, encompassing implicit, explicit and hybrid solvation and the experimental case. The experimental onset potential for HCOOH formation is taken from Ref.[47].

| Method | HCOOH onset potential [V] |
|---|---|
| Vacuum | -0.24 |
| Implicit | -0.44 |
| Explicit | -0.98 |
| Hybrid | -1.05 |
| Experimental | -1.08 |

explicit solvent molecules are sufficient for capturing water-adsorbate interactions. 4.3(a) illustrates the adsorption energy of HCOO* with increasing number of up to 12 explicit water molecules (indicated in blue). While we initially calculated the adsorption energy of HCOO* to be around -0.7 eV for 1-2 explicit water molecules, the adsorption energy of HCOO* further stabilizes to -0.95 eV for 3-7 explicit water molecules and even up to -1.42 eV for 8-12 explicit water molecules.

This stabilization of HCOO* with increasing number of water molecules can be rationalized with the increasing number of H-bonds between HCOO* and water molecules as well as the transformation of the HCOO*-water system from a cluster for lower number of H$_2$O molecules to a connected water layer for higher number of H$_2$O molecules, due to the increased number of H-bonds (see Figure B.3 in Appendix B). Thus, for the specific case considered here, at least eight explicit water molecules are needed to capture the impact of explicit solvation on the solvated HCOO* adsorption energy. In general, to find the sufficient number of explicit water molecules, one has to ensure that the number of hydrogen bonds in the water-adsorbate system is saturated. For HCOO* it is four hydrogen bonds, with two hydrogen bonds between each oxygen of HCOO* and its surrounding water molecules. In the case of COOH* (Figure 4.3(b)), the trend is not as clear as for HCOO*. The adsorption energy of COOH* does not vary significantly with increasing number of explicit water molecules. The COOH* adsorption energy was determined to be 0.47 eV for the case of one explicit H$_2$O molecule, and it remained nearly the same, 0.53 eV, for the case of 12 explicit H$_2$O molecules. As mentioned earlier, the COOH* reaction intermediate forms fewer hydrogen bonds with surrounding water molecules and therefore maintains the same configuration as in the vacuum or implicit solvation case. This observation can be explained with the adsorbate-water interaction being weaker for COOH* than for
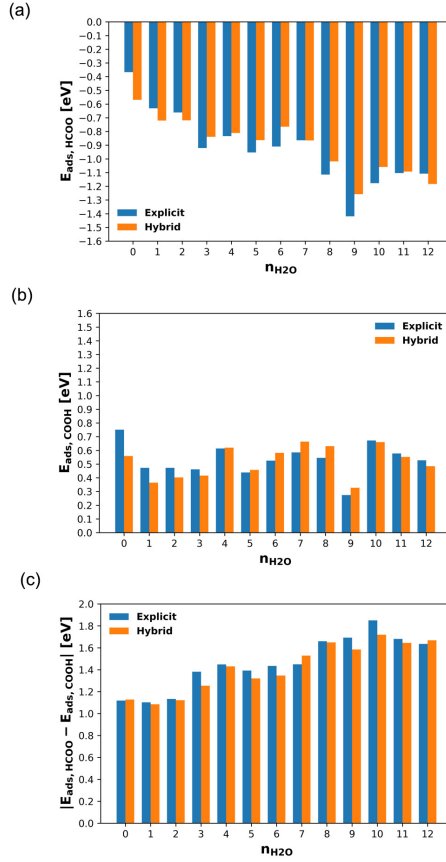
*Figure 4.3: Adsorption energy of (a) HCOO\* and (b) COOH\* on Pb(100) surface and (c) the difference of HCOO\* and COOH\* using explicit and hybrid solvation methods ranging from 0-12 water molecules. The hybrid case at 0 $H_2O$ shows the purely implicit solvation case.*

HCOO\*.

Figure 4.3(c) shows the difference of adsorption energies between HCOO\* and COOH\*, $|E_{ads,HCOO} - E_{ads,COOH}|$, with increasing $n_{H_2O}$. The difference increases from 1.12 eV in vacuo phase up to 1.85 eV in the explicit solvation environment, primarily due to the significant increase of $E_{ads,HCOO}$ in explicit solvation environment. As can be deduced from the direct comparison of results obtained in explicit and hybrid solvation schemes (denoted here as "hybrid"), adding additional implicit solvation

does not alter the reaction energies significantly.

We have also performed additional adsorption energy calculations with D3 corrections to assess the need of including dispersion effects in our work. Table 4.3 compares the adsorption energy differences of HCOO* and COOH*, |E$_{ads,HCOO}$ - E$_{ads,COOH}$|, for 0,1,6,11 and 12 explicit water molecules on Pb(100) surface with and without dispersion D3 corrections. For all cases, adding dispersion corrections does not lead to

Table 4.3: *Adsorption energy difference of HCOO* and COOH*, |E$_{ads,HCOO}$ - E$_{ads,COOH}$|, for 0,1,6,11 and 12 explicit water molecules on Pb(100) surface with and without dispersion D3 corrections. Results obtained without dispersion corrections are also illustrated in Figure 4.3(c).*

| Number of H$_2$O | |E$_{ads,HCOO}$ - E$_{ads,COOH}$| [eV] | |
| :---: | :---: | :---: |
| | **PBE** | **PBE+D3** |
| **0** | 1.12 | 1.11 |
| **1** | 1.10 | 1.14 |
| **6** | 1.43 | 1.45 |
| **11** | 1.68 | 1.66 |
| **12** | 1.64 | 1.64 |

significant differences compared to the case without dispersion correction, with variations <0.05 eV. Due to the small impact of dispersion corrections for our system, we have not included dispersion corrections in further calculations.

## 4.3.2 Reaction Energy Pathways for CO$_2$ Reduction Reaction at Pb(100) and Ag(100) Surfaces

In this section, we evaluate the effect of explicit solvation on reaction energies and selectivities of CO$_2$ towards formation of HCOOH and CO on both Pb(100) and Ag(100) surfaces compared to the vacuum case. The reaction pathways towards CO and HCOOH have been discussed in Section 4.3.1, where the HCOO* pathway (Reactions (4.11) and (4.12)) represents CO$_2$ reduction to HCOOH via HCOO* and the COOH* pathway (Reactions (4.13) and (4.14)) represents CO$_2$ reduction to CO via COOH*. For simulations in the explicit solvation scheme, we have incorporated 12 explicit water molecules on the Pb(100) surface and 8 explicit water molecules on the Ag(100) surface, which are equivalent to the formation of one complete water layer on each surface, respectively [57, 174].

Figure 4.4 illustrates HCOO* and COOH* reaction energy pathways on both Ag(100) and Pb(100) *in vacuo*. For the first reduction reaction step, CO$_2$ favours

Figure 4.4: Free energy diagram for CO$_2$ reduction towards CO and HCOOH via HCOO*
and COOH* reaction intermediate under vacuum environment on (a) Ag(100) surface and
(b) Pb(100) surface. Red lines and asterisk represent activation barrier (G$_a$) and adsorbed
solute state, respectively.

the HCOO* pathway towards the HCOO* intermediate on both Ag and Pb with acti-
vation energies of 0.64 eV and 0.29 eV, respectively; the first step of the COOH* path-
way exhibits activation energies of 1.76 eV and 1.62 eV, respectively. The stronger
preference for the HCOO* pathway and thus the reaction towards HCOOH as a prod-
uct is supported by HCOO* being more stable than COOH* by 1.05 eV and 1.19 eV
on the Ag and Pb surfaces, respectively. Thus, reaction energy pathway calculations
for the vacuum case indicate HCOOH as be the main product of CO$_2$ reduction on
both metal catalysts, in contradiction to experimental observations [10, 27, 47, 155].

Similar to the vacuum case, we obtain a significantly higher activation barrier for the formation of COOH* compared to the formation of HCOO* on the Ag surface using implicit solvation (Figure B.4 in the Appendix). Consequently, reaction energy calculations with implicit solvation reaffirm HCOOH as the primary product on Ag, consistent with the observations made in the vacuum case.

In order to determine whether explicit solvation effects can resolve this issue, we have repeated reaction energy pathway calculations, but now with the addition of explicit solvation (Figure 4.6). We have incorporated 12 explicit water molecules on the Pb(100) surface and 8 explicit water molecules on the Ag(100) surface, equivalent to one water layer. In the explicit solvation case, the protons required for hydrogenation reactions, e.g., in CO$_2$ + H$^+$ + e− → HCOO* or COOH*, originate from the hydronium ions (H$_3$O$^+$) in water, employed in previous computational works to elucidate the mechanism of the CO$_2$ reduction reaction in solvation environment [46, 175]. Figure 4.5 illustrates the H$_3$O$^+$-hydrogenation mechanism from HCOO* to form HCOOH* on Pb(100) surface, where the extra proton comes from the neighbouring hydronium ion to form HCOOH.



**HCOO* + H***          **HCOOH***

**Initial state**      **Transition state**      **Final state**
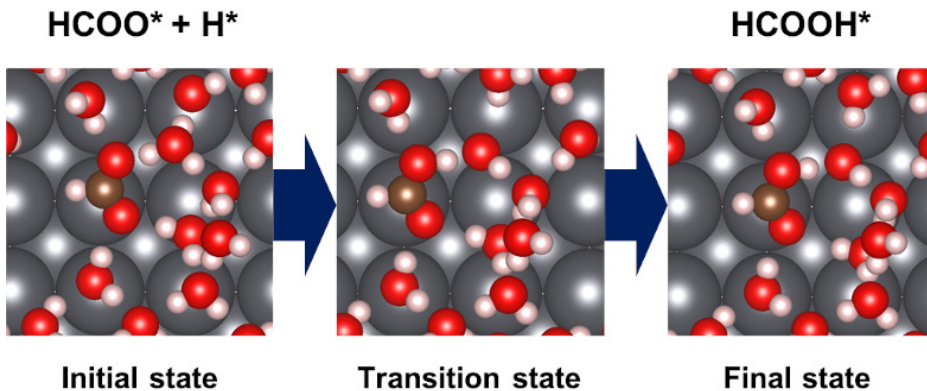
Figure 4.5: Illustration of H$_3$O$^+$-mechanism from HCOO* to form HCOOH* on Pb(100). H* indicates the presence of H$_3$O$^+$, which supplies a hydrogen to the HCOO* reaction intermediate.

In contrast to the the vacuum case, including explicit water molecules in simulations allows for explicit water-CO$_2$ interactions to be accounted for. By incorporating explicit water-CO$_2$ interactions, we are capable of modeling the CO$_2$ transformation
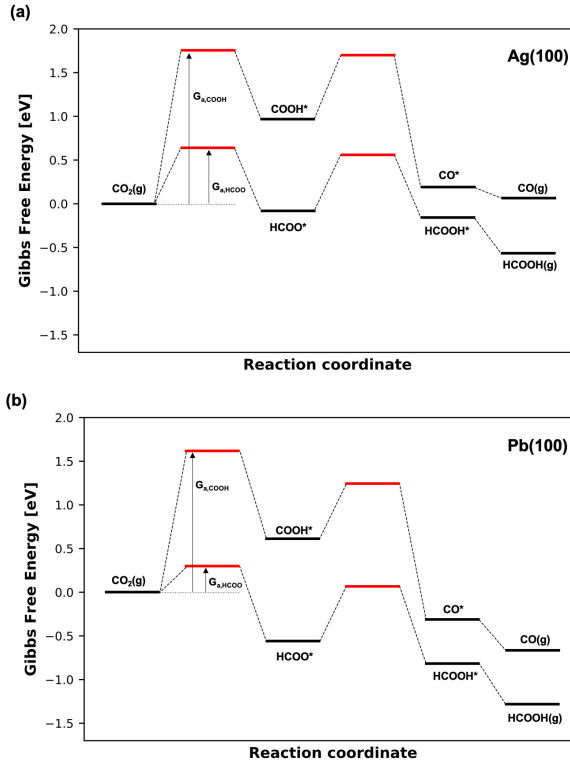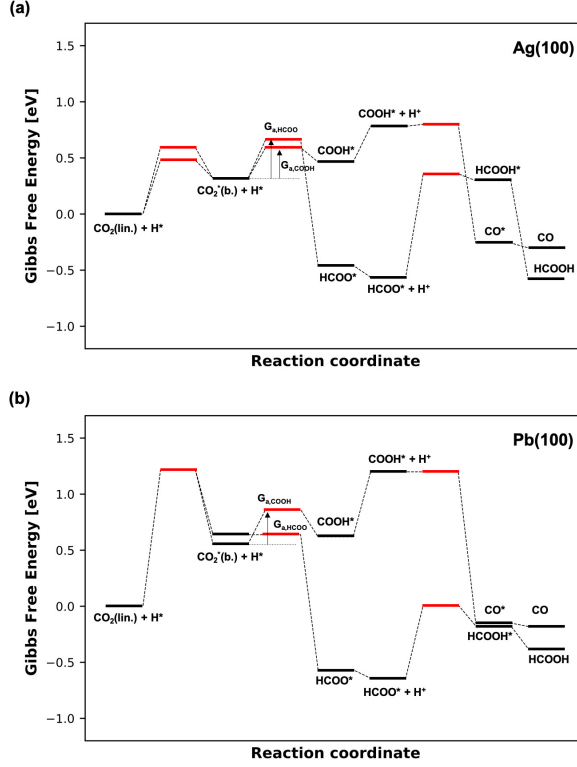
*Figure 4.6: Free energy diagram for CO$_2$ reduction towards CO and HCOOH via HCOO\* and COOH\* reaction intermediate under explicit solvation environment on (a) Ag(100) surface and (b) Pb(100) surface. Asterisk, lin. and b. represent transition states, adsorbed solute state, linear configuration and bent configuration, respectively. H\* represents the presence of $H_3O^+$-ion in the system, which is used for activation barrier calculation (indicated in red) of hydrogenation reactions.*

from linear to bent structure, which is a vital initial step of the CO$_2$ reduction reaction [176]. The transformation of CO$_2$ in linear configuration to CO$_2$ in bent configuration requires 1.21 eV on the Pb(100) surface, while <0.60 eV are needed on the Ag(100) surface. This observation aligns with experimental results, where Ag was observed to be more "CO$_2$-active" than Pb [47, 177, 178]. In addition, under explicit solvation conditions, the activation energy required for the transformation of CO$_2$ to HCOO\* and COOH\* is lower for HCOO\* on Pb, leading to HCOOH as the

product. Conversely, COOH* is more favourable on Ag leading to the production of CO. This finding agrees well with experimental observations. Simulations under vaccuum and implicit solvation conditions on the other hand predict HCOOH as the preferred product on both surfaces. For the explicit solvation case, the activation energy of $CO_2$ to HCOO* on the Ag(100) surface is 0.07 eV higher than the value for the reduction of $CO_2$ to COOH*, whereas the activation energy of the reaction of $CO_2$ to HCOO* on Pb(100) is 0.22 eV lower than the value of the reaction of $CO_2$ to COOH*. Regarding the reaction step from HCOO* to HCOOH, we observe the same activation energy of 0.64 eV on both Pb and Ag surfaces under vacuum conditions. In the explicit solvation case, the activation energy remains similar for Pb (0.65 eV), while it increases to 0.92 eV for Ag, limiting the further reaction to HCOOH product.

To further analyze the kinetics of the process, we have employed a microkinetic model to assess the product selectivity on both Ag and Pb surfaces using our calculated reaction and activation energies under vacuum environment and solvated environment. Microkinetic modeling has previously shown to be an essential tool for quantitative analysis of multiple-pathway reactions [179, 180, 181]. In the vacuum case, the microkinetic model results in selectivities of $s_{CO} \approx 0$ and $s_{HCOOH} \approx 1$ on both Ag(100) and Pb(100) surfaces, which contradicts experimental observations. The numerical results show that both Ag(100) and Pb(100) prefer the HCOOH pathway *in vacuo* since the coverage of HCOO* is much higher than that of COOH*, resulting in the high preference for the production of HCOOH. Also for the implicit solvation case, microkinetic modeling results in selectivities of $s_{CO} \approx 0$ and $s_{HCOOH} \approx 1$ on the Ag(100) surface, consistent with the findings of the vacuum case. Similar to the vacuum case, it fails to predict HCOOH as the primary product on the Ag(100) surface. For the explicit solvation case, we follow the same above procedure to obtain HCOOH and CO product selectivities from our microkinetic model. Details on the reaction mechanism and the rate equations used for the microkinetic model in the solvation case are given in the Appendix B. Given the reaction energies and activation barriers in Figure 4.6, we obtain $s_{CO} \approx 1$ and $s_{HCOOH} \approx 0$ for Ag(100) and $s_{CO} \approx 0$ and $s_{HCOOH} \approx 1$ for Pb(100), which matches experimental results. In solvated explicit environment, the coverage of HCOO* is also higher than that of COOH* on both Ag(100) and Pb(100). However, the desorption barrier of HCOO* to HCOOH on Ag(100), as shown in Figure 4.6, is too high to favor the HCOO* pathway, leading to a preference for the CO pathway, whereas the desorption barrier of HCOO* on

Pb(100) is moderate, enabling a preferential pathway for HCOOH.

It should be noted here that our DFT analysis and microkinetic modelling are relevant at 0 V vs. RHE. For the specific case considered in this work, microkinetic modeling under more negative potentials would be more accurate, since the theoretical equilibrium potentials for HCOOH and CO are -0.17 V vs. RHE and -0.12 V vs. RHE, respectively [25]. For consideration of other electrochemical conditions (i.e., different electrode potential), potential-dependent activation barriers from DFT calculation would be required, which goes beyond the scope of this work. During microkinetic modeling, we make a distinction in the proton source between the vacuum case and the explicit solvation case. In the explicit solvation case, the proton originates from the H$_3$O$^+$-ion present in water, as elaborated in the previous section. In the vacuum phase, the proton originates from hydrogen adsorbed on the metal surface, formed via the Tafel reaction.

## 4.4 Discussion

### 4.4.1 Explicit Solvation Uncertainty Analysis of HCOO$^*$ and COOH$^*$ Adsorption Energy

While we have shown in the previous section that explicit solvation has a considerable impact on adsorption energies of HCOO$^*$ and COOH$^*$ reaction intermediates on the Pb(100) and Ag(100) surface, a sufficient sampling of explicit water configurations is required to correctly assess the uncertainty of the solvated adsorption energy of reaction intermediates. In this section we used a combined MD/DFT approach to analyze the uncertainty of HCOO$^*$ and COOH$^*$ adsorption energies on the Pb(100) surface in the presence of n (n = 6, 12) explicit water molecules. Similar CMD/DFT procedures have been proposed in the past to study solvent effects for methanol electrooxidaation on gold [150] as well as important reaction species for ammonia synthesis on Pt [182]. We initially ran a 10 ns MD trajectory of 95 explicit water molecules on the Pb surface, equivalent to a water density of 1 g/L. We then picked out 19 different configurations equally spaced over this time span (1 ns, 1.5 ns, 2 ns ..., 10ns), removed all explicit water molecules except for 6 and 12 explicit water molecules closest to the Pb surface and optimized the obtained configurations using DFT to obtain a range of adsorption energies for HCOO$^*$ and COOH$^*$. The MD/DFT procedure is illustrated in Figure

4.7. The purpose of this combined MD/DFT procedure is to quantify the adsorption

## Combined MD/DFT simulation
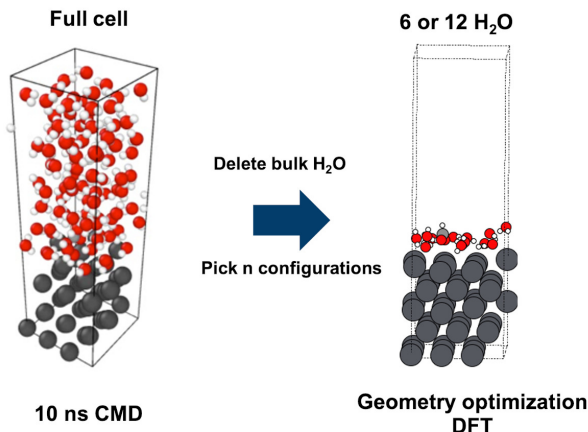


*Figure 4.7: Workflow of combined MD/DFT simulation procedure. After running a 10ns CMD simulation of a simulation cell filled completely with explicit water molecules, n different, independent configurations are selected from the CMD simulation. After that, all bulk water molecules from the system except the remaining 6 or 12 explicit water molecules closest to the Pb surface are removed. Lastly, DFT geometry optimizations from the given configurations are carried out.*

energy range of HCOO* and COOH* in explicit solvation and to assess the commonly overlooked uncertainty range that arises from analyzing stationary water-adsorbate configurations. Given that water structure equilibration could typically take several hundreds of picoseconds [153], using AIMD for this task would be computationally too expensive. Conversely, classical molecular dynamics (CMD) requires a suitable force field to obtain energies that closely resemble those obtained through quantum mechanical methods. Thus, with the combined MD/DFT method, water structures are equilibrated using CMD followed by the DFT optimization of the structures to obtain more accurate energies.

In Table 4.4, we have summarized the standard deviations (SD) for calculating solvated adsorption energies for both reaction intermediates HCOO* and COOH* on the Pb(100) surface in the explicit solvation environment. Regarding the adsorption energy of HCOO*, it is evident that increasing the number of explicit water molecules from 6 $H_2O$ to 12 $H_2O$ increases the standard deviation (SD) by 0.07 eV

Table 4.4: *Statistical mean, minimum (Min), maximum (Max) and standard deviation of the mean value (SD) of HCOO* adsorption energies, $E_{ads,HCOO}$, and COOH* adsorption energies, $E_{ads,COOH}$, on Pb(100) surface in the presence of 6 and 12 explicit water molecules from the combined MD/DFT method. The sample size is n = 19.*

| Pb(100) | $E_{ads,HCOO}$[eV] | | $E_{ads,COOH}$[eV] | |
|---|---|---|---|---|
| Variables | 6 H$_2$O | 12 H$_2$O | 6 H$_2$O | 12 H$_2$O |
| Mean | -0.89 | -1.01 | 0.42 | 0.40 |
| Min | -1.13 | -1.28 | 0.13 | 0.12 |
| Max | -0.60 | -0.48 | 0.70 | 0.58 |
| SD | 0.14 | 0.21 | 0.16 | 0.15 |

and the minimum-maximum range by more than 0.25 eV, indicating a growing degree of uncertainty and sensitivity with increasing number of H$_2$O molecules. While the HCOO* adsorption energy with 6 water molecules ranges from around -0.60 eV to -1.13 eV, for 12 water molecules the HCOO* adsorption energy ranges from -0.48 eV to -1.28 eV. In the case of COOH*, the adsorption energy ranges from 0.13 eV to 0.70 eV for six explicit water molecules and from 0.12 eV to 0.58 eV for 12 water molecules. Interestingly, for pure water structures the uncertainty ranges are much lower, as shown in Table 4.5, which means that the presence of adsorbates contribute significantly to a greater degree of possible configurations and uncertainty of adsorption energies. Furthermore, the mean adsorption energy of HCOO* for both cases

Table 4.5: *Statistical mean, minimum (Min), maximum (Max) and standard deviation (SD) of H$_2$O* adsorption energies, $E_{ads,H2O}$, on Pb(100) surface in the presence of 6 and 12 explicit water molecules from the combined MD/DFT method. The sample size is n = 19.*

| Pb(100) | $E_{ads,H2O}$[eV] | |
|---|---|---|
| Variables | 6 H$_2$O | 12 H$_2$O |
| Mean | -0.32 | -0.42 |
| Min | -0.35 | -0.43 |
| Max | -0.27 | -0.40 |
| SD | 0.02 | 0.01 |

ranges from around -1.01 eV to -0.89 eV, while the mean adsorption energy of COOH* ranges from only 0.40 eV to 0.42 eV, confirming our above observation that HCOO* in solvation tends to change its configuration more frequently leading to more degrees of freedom and ultimately a greater range of adsorption energies. We have also compared HCOO* adsorption energies on Pb(100) computed with 12 explicit water molecules with an increased sample size of n = 38 (Table 4.6). Apart from an increase in the Min-Max range by 0.09 eV, the mean and SD of the HCOO* adsorption energy

is comparable to the results of the smaller sample size of n = 19.

*Table 4.6: Statistical mean, minimum (Min), maximum (Max) and standard deviation (SD) of HCOO\* adsorption energy, $E_{ads,HCOO}$, on Pb(100) surface in the presence of 12 explicit water molecules from the combined MD/DFT method using a sample size of n = 19 and n = 38 configurations.*

| Pb(100) | $E_{ads,HCOO}[eV]$ | |
|---|---|---|
| **Variables** | n=19 | n=38 |
| **Mean** | -1.01 | -1.03 |
| **Min** | -1.28 | -1.37 |
| **Max** | -0.48 | -0.48 |
| **SD** | 0.21 | 0.22 |

The results in Table 4.4 show that HCOO* and COOH* adsorption energies with 12 explicit $H_2O$ molecules on Pb(100) surface vary with a SD of 0.21 eV and 0.15 eV, respectively. However, our initial computational predictions of product selectivities discussed in Section 4.3.2 are based on only one representative HCOO* and one representative COOH* configuration. Therefore, we have conducted a sensitivity analysis of our explicit solvation results from Section 4.3.2 retrospectively, to bolster the confidence of our initial computational predictions. By varying HCOO* and COOH* adsorption energies on both Pb(100) and Ag(100) surfaces, along with their corresponding SD from Table 4.7, selectivities towards HCOOH and CO over a range of adsorption energies can be generated. In this context, we make the assumption that altering the adsorption energies, $E_{ads,COOH/HCOO}$, will result in an identical change in the activation barrier, $G_{a,COOH/HCOO}$.

*Table 4.7: Statistical mean, minimum (Min), maximum (Max) and standard deviation (SD) of HCOO\* adsorption energy, $E_{ads,HCOO}$, and COOH\* adsorption energy, $E_{ads,COOH}$, on Pb(100) and Ag(100) surface in the presence of one explicit water layer. A sample size of n = 19 has been used.*

| | Pb(100) | | Ag(100) | |
|---|---|---|---|---|
| **Variables** | $E_{ads,HCOO}[eV]$ | $E_{ads,COOH}[eV]$ | $E_{ads,HCOO}[eV]$ | $E_{ads,COOH}[eV]$ |
| **Mean** | -1.01 | 0.40 | -0.71 | 0.35 |
| **Min** | -1.28 | 0.12 | -0.92 | 0.03 |
| **Max** | -0.48 | 0.58 | -0.50 | 0.63 |
| **SD** | **0.21** | **0.15** | **0.13** | **0.15** |

Figure 4.8 illustrates the HCOOH and CO selectivity of $CO_2$ reduction on both Pb(100) and Ag(100) surfaces over a range of activation barriers for HCOO*, $G_{a,HCOO}$, and COOH*, $G_{a,COOH}$. As shown in Figure 4.8, the reference case from Section 4.3.2
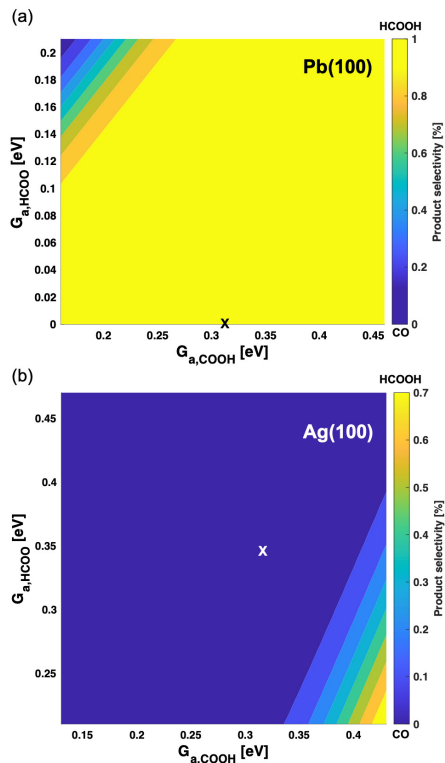
Figure 4.8: Contour graph showing HCOOH and CO product selectivity on (a) Pb(100) surface and (b) Ag(100) surface with varying $G_{a,HCOO}$ and $G_{a,COOH}$. x indicate the reference case that has been extracted from Figure 4.6 in Section 4.3.2.

(marked with x) gives high selectivity towards CO on Ag and high selectivity on HCOOH on Pb. Varying $G_{a,HCOO}$ and $G_{a,COOH}$ over a range of one SD does not change the initial trend. Only for the extreme cases of $G_{a,COOH}$<0.2 eV and $G_{a,HCOO}$>0.18 eV at Pb(100) surface and $G_{a,COOH}$>0.4 eV and $G_{a,HCOO}$<0.25 eV at Ag(100) surface we observe a reversed trend. The observation that the HCOOH and CO selectivities within the considered activation energy range largely align with the selectivities observed in the reference case, provides strong support for our computational predictions made in Section 4.3.2.

The two important lessons to take away from this section are: (1) it is of utmost importance to provide uncertainty ranges for solvated adsorption energies containing

static water structures in order to evaluate the confidence of subsequent computational predictions with respect to experimental observations and (2) the more explicit water molecules are incorporated in simulations, the bigger is the configurational space of the explicit water molecules, leading to a larger range of possible configurations. Consequently, the greater configurational space results in a higher uncertainty range of adsorption energies. Thus, we must exercise caution when interpreting computational results in explicit solvation environment.

## 4.4.2 Potential Descriptors that Affect HCOO$^*$ and COOH$^*$ Adsorption Energy in Solvation

As shown in the previous section, calculating exact HCOO$^*$ and COOH$^*$ adsorption energies in solvation environment can be challenging, owing to the large configurational space of the system. While the task of precisely identifying the properties that contribute to the variation in adsorption energies in solvation can become quite complex, we discuss potential descriptors that can affect the adsorption energy of HCOO$^*$ in solvation. For this, we have considered five different configurations of HCOO$^*$ in the presence of 12 explicit water molecules generated and optimized using the combined MD/DFT method (as described in Section 4.4.1). Figure 4.9 shows the comparison of the five different HCOO$^*$-water configurations based on properties such as total number of H-bonds, number of H-bonds with HCOO$^*$, average HCOO$^*$ distance from the Pb(100) surface, the cavitation energy E$_{cav}$ and the adsorbate insertion energy E$_{ins}$. While most of the descriptors are commonly understood, the cavitation energy E$_{cav}$ is defined here as the energy needed for the water structure to reorganize when the adsorbate is present compared to when it is not present and the adsorbate insertion energy E$_{ins}$ is defined as the energy difference between the adsorbate with its surrounding solvation shell compared to the non-interacting adsorbate and the solvation shell [60].

At first sight, the total number of hydrogen bonds in the system correlates well with the magnitude of the adsorption energies of our five representative configurations. The more hydrogen atoms exist in the system, the higher is the adsorption energy of HCOO$^*$ in solvated environment. Configuration 1 involves 20 H-bonds with an adsorption energy of -1.37 eV, while configuration 2 has 15 H-bonds with an adsorption energy of only -0.48 eV. However, on a quantitative level, the correlation with
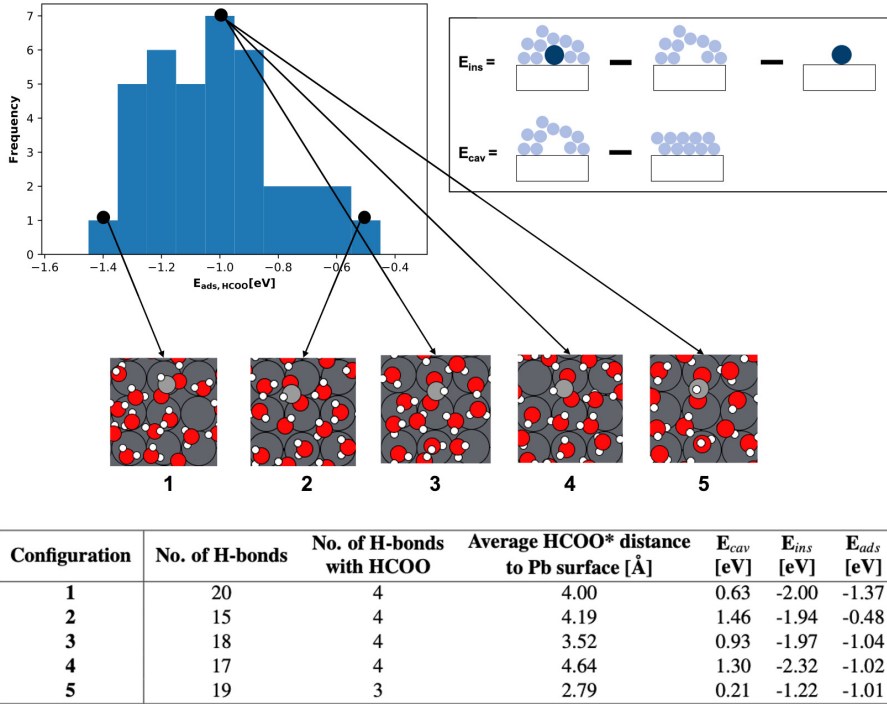
Figure 4.9: *Comparison of five different configurations of HCOO in the presence of 12 explicit water molecules based on number of H-bonds, number of H-bonds with HCOO, average HCOO distance from the Pb(100) surface, $E_{cav}$ and $E_{ins}$. The configurations are picked out from a sample size of n = 38.*

| Configuration | No. of H-bonds | No. of H-bonds with HCOO | Average HCOO* distance to Pb surface [Å] | $E_{cav}$ [eV] | $E_{ins}$ [eV] | $E_{ads}$ [eV] |
|---|---|---|---|---|---|---|
| 1 | 20 | 4 | 4.00 | 0.63 | -2.00 | -1.37 |
| 2 | 15 | 4 | 4.19 | 1.46 | -1.94 | -0.48 |
| 3 | 18 | 4 | 3.52 | 0.93 | -1.97 | -1.04 |
| 4 | 17 | 4 | 4.64 | 1.30 | -2.32 | -1.02 |
| 5 | 19 | 3 | 2.79 | 0.21 | -1.22 | -1.01 |

the number of H-bonds fails to explain why configurations 3,4 and 5 have the same adsorption energy with different number of hydrogen bonds. There must exist other descriptors that impact the adsorption energy apart from the number of hydrogen bonds, albeit not as significant.

While the number of hydrogen bonds of HCOO* with its surrounding solvation shell is mostly constant (4 hydrogen bonds) for most of the configurations, we can exclude it from being a potential descriptor. However, the average formate distance from the Pb(100) surface together with the total number of H-bonds from HCOO-H$_2$O and H$_2$O-H$_2$O interactions, are capable of explaining why configurations 3,4 and 5 have the same adsorption energy with different number of H-bonds. For the three
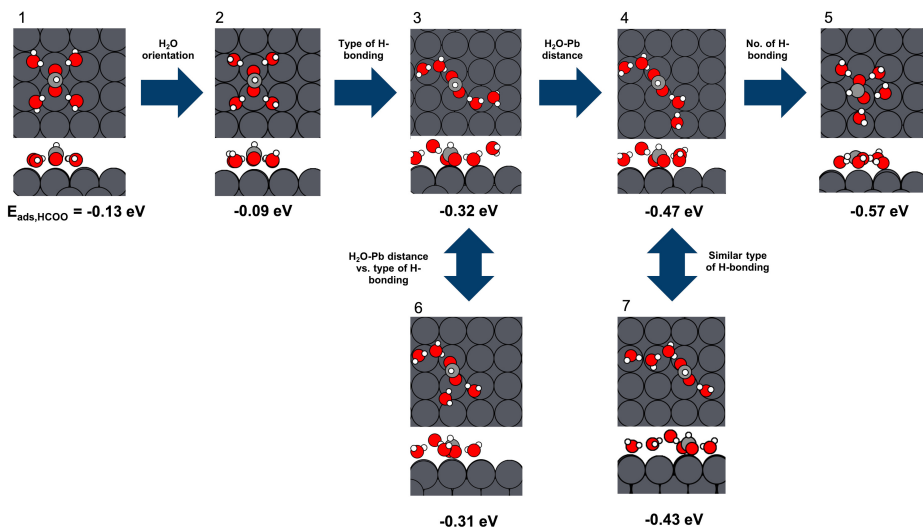
*Figure 4.10: HCOO\* adsorption energy comparison of different water configurations for 4 explicit H$_2$O.*

cases, an increasing number of hydrogen bonds is accompanied by a decreasing average distance of formate to the metal surface, which leads to comparable adsorption energies.

For the last two descriptors, $E_{ins}$ and $E_{cav}$, $E_{ins}$ is not capable of describing the adsorption trend, while $E_{cav}$ can only qualitatively explain the higher adsorption energy with decreasing cavitation energy. Considerations of $E_{ins}$ and $E_{cav}$ as descriptors, as proposed in the existing literature [60], fails to properly explain the adsorption trends observed for HCOO$^*$ in the presence of 12 explicit water molecules. So far only the total number of hydrogen bonds has shown to exert a significant impact on the HCOO$^*$ adsorption energy. It remains, however, difficult to find a global descriptor that captures all effects on the adsorption energy, let alone a system containing 12 explicit water molecules.

Therefore, we have attempted to disentangle different effects that govern the adsorption energy of solvated HCOO$^*$ by analyzing HCOO$^*$ in the presence of only four explicit molecules, which is equivalent to the number of hydrogen bonds in the first solvation shell of formate. Figure 4.10 shows the different configurations of formate

with four water molecules, starting with a reference configuration 1 and then changing its configurations slightly to observe the impact of different effects such as the number of H-bonds, the type of H-bonding, the water-metal distance as well as the orientation of the explicit water molecules. Configuration 5 has the highest adsorption energy with -0.57 eV, which is 0.44 eV more stable than the reference configuration 1. While the reference configuration consists of only four hydrogen bonds, configuration 5 has five hydrogen bonds leading to the higher adsorption energy. Apart from the total number of hydrogen bonds, the type of hydrogen bonding also affects the magnitude of the adsorption energy. While both configuration 2 and 3 contain 4 hydrogen bonds, their adsorption energies vary by 0.23 eV, which can be explained by the fact that configuration 3 has two H-bonds stemming from water molecules while the other two stem from formate with its surrounding water molecule. On the other hand, configuration 2 has all its H-bonds stemming from the interaction between formate and its surrounding water molecules, indicating that water-water H-bonding is more stable compared to formate-water H-bonding. We observe an additional stabilization of the solvated formate adsorption energy as captured in configuration 4 compared to configuration 3, attributed to the reduced water-metal distance. Lastly, the orientation of water molecules has a minor effect on the adsorption energy (configuration 1 vs. configuration 2).

In total, we have assessed four potential descriptors that govern the adsorption energy of solvated HCOO$^*$ on Pb(100) surface. We discovered that there is no single global descriptor that can fully account for the variation in adsorption energy. Instead, a combination of all four descriptors is essential to describe the change in adsorption energy, with the total number of hydrogen bonds per unit cell being the most significant one followed by the type of hydrogen bonding, the water-metal distance and lastly, the orientation of water molecules.

## 4.5 Summary

We have performed a systematic study on the role of solvation effects on the CO$_2$ reduction reaction towards HCOOH and CO at Pb(100) and Ag(100) surfaces. We have demonstrated how the number of explicit water molecules exerts a substantial effect on the adsorption energy of relevant reaction intermediates. Implicit solvation affects the adsorption energy in a much less pronounced manner than explicit

solvation. Using an explicit solvation scheme in combination with microkinetic modeling, we were able to identify CO as the main product on Ag and HCOOH as the main product on Pb, which is in agreement with experimental observations. To the best of our knowledge, this is the first computational demonstration of predicting the main products from CO$_2$ reduction reaction on both Ag and Pb catalyst, taking into account solvation phenomena.

When it comes to calculating adsorption energies of reaction intermediates in explicit solvation environment, assessment of the uncertainty of computed adsorption energies is a necessary step to evaluate the accuracy of the method. We have attempted to delineate factors affecting the computed adsorption energy of HCOO* on Pb(100) surface. The total number of H-bonds, originating from HCOO-H$_2$O and H$_2$O-H$_2$O interactions, emerged as the main factor determining the HCOO* adsorption energy. Other factors such as the type of H-bonding, the adsorbate-metal distance or the orientation of water molecules were found to play a less significant role in this regard.

Overall, this work provides valuable insight into the role of different solvation methods of adsorbates on metal surfaces, and it reveals explicit solvation as a vital effect to be included in the computation of pathways of the CO$_2$ reduction reaction.

# Chapter 5

# Entropy Effects on Reactive Processes at Metal-Solvent Interfaces

**Note:** Since the following chapter is based on an accepted manuscript "O. Cheong, F. Tipp, M. H. Eikerling, P. M. Kowalski, Entropy effects on reactive processes at metal-solvent interfaces", the personal pronoun "we" is used throughout this chapter to refer to the group of researchers that were part of this specific study. In this study, all calculations and analyses were performed by me as well as drafting the manuscript. Fabian Tipp provided assistance during the 2PT calculations, while the remaining co-authors mentioned above played a supervisory role in this research.

In this chapter, we extended our analysis of the metal-electrolyte interface by including and investigating entropy effects of molecules in solution and at metal surfaces. Reliable estimate of reaction entropies are of utmost importance to correctly predict reaction free energies of chemical transform at metal-electrolyte interfaces. In this realm, we demonstrate here the suitability of the two phase thermodynamic (2PT) model and classical molecular dynamics simulations for the accurate and computationally efficient determination of entropies of reactive species in a solvent environment. Systematic analysis of entropies of different alcohol species in bulk solution and at platinum (Pt), silver (Ag) and lead (Pb) surfaces are presented. A metal-dependent reduction of entropies at metal-electrolyte interfaces are observed in comparison to the results for bulk, aqueous or organic solvents. Entropies are seen to decrease by at

least 30 % relative to the bulk environment. This effect is attributed to the reduction in rotational and translational entropy contributions at metal-electrolyte interfaces. By comparing the results with the prediction of theoretical models, the origin of the cavitation entropy is deciphered. Overall, solvation effects exert a significant impact on reaction free energies, furthermore causing several orders of magnitude change in the reaction rates. The presented study provides valuable insight into solute entropies at metal-solvent interfaces, which is highly relevant in view of deciphering electrochemical processes.

## 5.1 Introduction

Reliable computation of thermodynamic parameters is of utmost importance of adsorption and reaction processes at solid-electrolyte interfaces with atomistic simulation methods. In particular entropic effects ($S$) on solutes involved in surface chemical processes have either been neglected or inaccurately represented using a simplistic gas approximation, assuming an idealized vacuum environment [45, 183, 184, 185, 186, 187]. In electrochemical systems, chemical reactions proceed at solid surfaces in presence of a fluidic solvent, which influences reaction free energies by entropic effects. To estimate the entropy in a solvent phase, theoretical models based on geometric and physical parameters (e.g., Garza [188], Conquest et al. [189]), which are not yet applicable to solid-liquid interfaces, or simulation based methods, such as thermodynamic integration (TI) [190, 191] or post-processing of the velocity autocorrelation function [192, 193, 194] can be applied.

TI requires high computational efforts, due to need for multiple simulations along an integration path [182, 195, 196, 197]. The two phase thermodynamics (2PT) approach is much less computationally demanding and at the same time produces reliable estimates of the entropies of solutes submerged in different solvents [192, 193, 194]. Jung et al. [198] have applied the 2PT method to the Pt(111)-water interface and they have found a significant reduction of entropy of water at the interface, in comparison to the bulk environment. The 2PT method relies on molecular dynamics simulations and Fourier transform of the velocity autocorrelation function and its analysis with a combination of solid-state (e.g., quantum harmonic oscillator) and diffusive gas (e.g., hard sphere model) models of vibrations, to compute thermodynamic properties of condensed, liquid systems.

Here, we apply the 2PT method to simulate entropies of different alcohol species in water and organic solvents and at various aqueous metal interfaces (Pt, Ag, Pb), that are important in electrochemistry. The research has been performed to: (1) compare the performance of the 2PT approach with existing theoretical models as well as experimental data and (2) analyze the impact of solute entropies on chemical reactions at metal-electrolyte interfaces.

In the following section, we will introduce the 2PT method and the computational approach used in this study. The subsequent sections deal with the application of the 2PT method for solute entropies in bulk environment and at metal-electrolyte interfaces, followed by potential limitations of the 2PT method.

## 5.2   Methods

### 5.2.1   2PT Method

The 2PT method has been developed by Lin et al. [193, 192, 194]. It comprises several different steps. In the first step, the total velocity autocorrelation function (VACF), $C(t)$, of the liquid system is computed from velocities extracted along the simulated trajectory. Calculations are done numerically by performing the following integration,

$$C(t) = \sum_{j=1}^{N} \sum_{k=1}^{3} m_j \lim_{\tau \to \infty} \frac{1}{2\tau} \int_{-\tau}^{\tau} v_j^k(t'+t) v_j^k(t') dt', \qquad (5.1)$$

where $m_j$, $v_j^k(t')$ and $\tau$ are the mass of atom $j$, the $k$-th velocity component of an atom $j$ at time $t'$ and the total simulation time, respectively. The total density of states (DOS) in frequency space is obtained via Fourier transform of $C(t)$,

$$DOS(\nu) = \frac{1}{k_b T} \int_{-\tau}^{\tau} C(t) e^{-2\pi i \nu t} dt. \qquad (5.2)$$

The obtained DOS is further decomposed into the translational, rotational and vibrational contributions, as shown in Figure 5.1(c).

The key procedure of the 2PT method is the decomposition of the total DOS into a solid-like component DOS$_{solid}$, which is modeled using harmonic approximation,
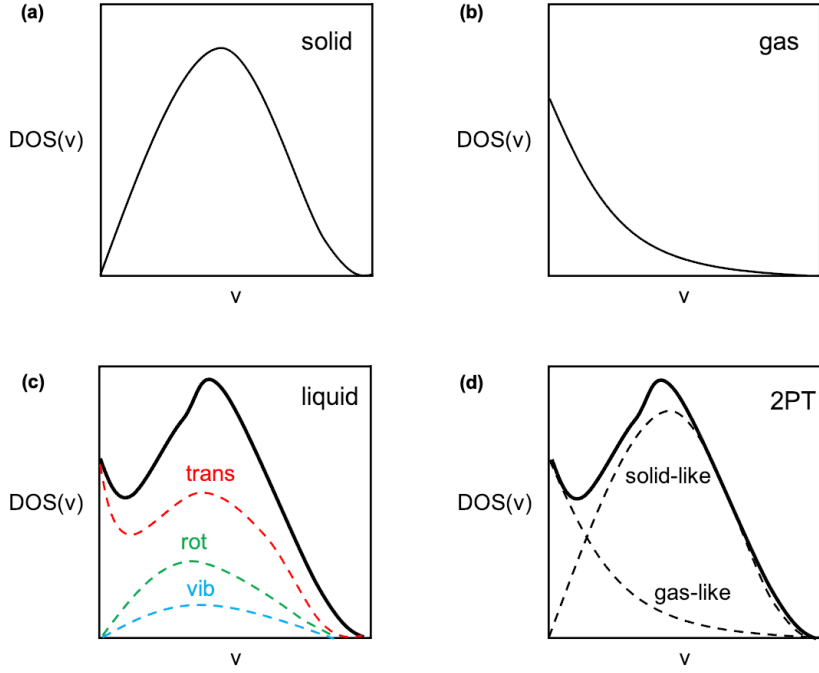
*Figure 5.1: Simplified illustration of density of state (DOS) distribution of a (a) solid, (b) gas, (c) liquid composed of translational, rotational and vibrational contributions and (d) liquid composed of solid-like and gas-like contributions. Reproduced from ref.[193], with the permission of AIP Publishing.*

and a gas-like component, $DOS_{gas}$, which is modeled using the hard sphere model, as illustrated in Figure 5.1(d) and Equation 5.3,

$$DOS(\nu) = (1 - f)DOS_{\text{solid}}(\nu) + fDOS_{\text{gas}}(\nu). \tag{5.3}$$

In order to determine the contributions from the two models, the fluidicity factor, $f$ is introduced and computed in the following way,

$$f = \frac{D(T, \rho)}{D_0^{\text{gas}}(T, \rho)} \tag{5.4}$$

It consists of the ratio of self-diffusivity, $D$, of the liquid system to the gas-like diffusivity, $D_0^{\text{gas}}$. The application of both models to analyze a liquid system is necessary, since low frequency diffusive modes are predominantly modeled using the gas-like model, while high frequency, vibrational modes are predominantly approximated by the static, solid-like model. From the solid- and gas-like DOS, the entropy, $S$, is obtained as

$$S = k \left[ \int_0^\infty DOS_{\text{solid}}(\nu) W_{\text{solid}}(\nu) + \int_0^\infty DOS_{\text{gas}}(\nu) W_{\text{gas}}(\nu) \right] d\nu, \qquad (5.5)$$

where $W_{\text{solid}}(\nu)$ and $W_{\text{gas}}(\nu)$ describe the solid and gas entropy weighing function, respectively. More details on the 2PT method can be found in Lin et al. [193].

## 5.2.2 Theoretical Solvation Model

Recently, Garza [188] introduced a simple theoretical model for computation of entropy of solvated species. The model is based on geometrical and physical arguments. The total entropy of a solute in solution ($S_{\text{tot}}$) is defined as a sum of four contributions: translational entropy $S_{\text{trans}}$, vibrational entropy $S_{\text{vib}}$, rotational entropy $S_{\text{rot}}$ and cavitation entropy $S_{\text{cav}}$,

$$S_{\text{tot}} = S_{\text{trans}} + S_{\text{vib}} + S_{\text{rot}} + S_{\text{cav}}. \qquad (5.6)$$

While the first three terms are standard, and occur also in the description of the entropy of gas phase species, the cavitation entropy considers the entropic contributions arising from reorganization of the solvent environment to form a cavity for the solute. The translational entropy is estimated from the translational partition function, $q_{\text{trans}}$,

$$S_{\text{trans}} = R \left( \ln \left( q_{\text{trans}} \right) + \frac{5}{2} \right), \qquad (5.7)$$

where $q_{\text{trans}}$ is defined as

$$q_{\text{trans}} = \left(\frac{2\pi m k_{\text{b}} T}{h^2}\right)^{\frac{3}{2}} V, \tag{5.8}$$

with $m$, $k_{\text{b}}$, $T$, $h$ and $V$ being the mass of the solute molecule, Boltzmann constant, temperature, Planck constant and the volume to which the solute molecule is confined, respectively. In solution, $V$ is defined as,

$$V = N_{\text{c}} v_{\text{c}}, \tag{5.9}$$

where $N_{\text{c}}$ is the average number of accessible cavities in the solute and $v_{\text{c}}$ is the volume of the solute cavity. The volume of the solute cavity depends on volumes of solute ($V_{\text{M}}$) and solvent molecules ($V_{\text{S}}$), the mass density of the solvent environment ($\rho$), Avogadro number ($N_{\text{A}}$) and the molar mass of solvent molecules ($M_{\text{S}}$),

$$v_{\text{c}} = \left(V_{\text{M}}^{\frac{1}{3}} + \left(\frac{M_{\text{S}}}{N_{\text{A}}\rho} - V_{\text{S}}\right)^{\frac{1}{3}}\right)^3. \tag{5.10}$$

The vibrational entropy contribution in solution is estimated applying the harmonic oscillator approximation,

$$S_{\text{vib}} = R \sum_i \left(\frac{h\nu_i}{k_{\text{b}} T \left(e^{\frac{h\nu_i}{k_{\text{b}} T}} - 1\right)} - \ln\left(1 - e^{\frac{h\nu_i}{k_{\text{b}} T}}\right)\right), \tag{5.11}$$

where $\nu_i$ is the $i$-th vibrational mode of the solute in solution. The rotational entropy in solution is defined as,

$$S_{\text{rot}} = R\left(\ln\left(q_{\text{rot}}\right) + \frac{3}{2}\right) + S_{\text{trans}}(T, r_{\text{c}} - r_{\text{g}}) - S_{\text{trans}}(T, r_{\text{c}}), \tag{5.12}$$

where the first term depends on the rotational partition function ($q_{\text{rot}}$) and the two remaining terms are translational entropy losses due to rotations inside a confined solvation cavity, which depends on the cavity radius ($r_{\text{c}}$) and the radius of gyration

$(r_\mathrm{g})$. The rotational partition function, $q_\mathrm{rot}$, is given by

$$q_\mathrm{rot} = \frac{\pi^{\frac{1}{2}}}{\sigma_\mathrm{r}} \left( \frac{8\pi^2 I k_\mathrm{b} T}{h^2} \right)^{\frac{3}{2}}, \tag{5.13}$$

where $I$ and $\sigma_\mathrm{r}$ represent the moment of inertia and the rotational symmetry number, respectively. The estimation of the cavity entropy, $S_\mathrm{cav}$, as applied here, is based on the scaled particle theory, using the concept of hard spheres. It is given by

$$S_\mathrm{cav} = -\frac{G_\mathrm{cav}}{T}, \tag{5.14}$$

where the free energy of cavity formation $(G_\mathrm{cav})$ is

$$G_\mathrm{cav} = k_\mathrm{b} T \left[ -\ln(1-y) + \frac{3y}{1-y} R_v + \left[ \frac{3y}{1-y} + \frac{9}{2} \left( \frac{y}{1-y} \right)^2 \right] R_v^2 \right], \tag{5.15}$$

with

$$y = \frac{3}{4\pi} \frac{\epsilon_r - 1}{\epsilon_r + 2} \tag{5.16}$$

and

$$R_v = \left( \frac{V_\mathrm{M}}{V_\mathrm{S}} \right)^{\frac{1}{3}}. \tag{5.17}$$

Here, $R_v$ is the ratio of solute and solvent molecule volumes, and $\epsilon_r$ is the relative permittivity of the solvent. More details on this entropy model are provided in Garza [188].

### 5.2.3 Computational Methodology

Periodic density functional theory (DFT) calculations for reaction and adsorption energies have been performed using the VASP package [171, 172, 173]. We applied the PBE exchange-correlation functional [137], the projector augmented wave method to describe the core electrons [138] and the plane wave energy cut-off of 500 eV. For all 3x3 metal surfaces, created using the atomic simulation environment (ASE) [139], we kept the bottom two layers frozen to mimic bulk-like environment, while the other

three top layers were allowed to relax. To avoid interactions between periodically repeated surfaces, we applied a $\sim 20$ Å thick vacuum space in direction perpendicular to the surface. A Monkhorst–Pack 4x4x1 $k$-point grid was used for sampling of Brillouin zone [140]. For implicit solvation calculations we used the VASPsol package [102, 101]. The calculated Pt, Ag and Pb bulk lattice constants of 3.98 Å, 4.15 Å, 5.03 Å, respectively, are in good agreement with measured values [47, 199, 200], as shown in Table 5.1.

*Table 5.1: Comparison of computed and experimental bulk lattice constants of Pt, Ag and Pb fcc metals.*

| Metal | Bulk lattice constant [Å] | |
| --- | --- | --- |
| | This work | Experimental |
| Pt | 3.98 | $3.92^a$ |
| Ag | 4.15 | $4.06^b$ |
| Pb | 5.03 | $4.95^c$ |

[a] Wanjala et al. [199], [b] Haas et al. [200], [c] Fan et al. [47]

Classical molecular dynamics (CMD) simulations have been performed with the LAMMPS software package [133]. Simulated trajectories obtained with CMD simulations are necessary for the application of the 2PT method. Interactions with the metal surfaces have been modeled using the Interface Force Field (IFF) [71], while solute interactions have been modeled using the OPLS AA/L force field [95]. The water environment has been described with the SPC water model [134]. Initial configurations of the water molecules had been generated with the PACKMOL package [135]. For the 2PT analysis, we have initially performed a 200 ps equilibration run in the NPT ensemble, followed by a 20 ps production run in the NVT ensemble. Production runs of 20 ps are sufficient to generate converged entropy values [193].

## 5.3   Results and Discussion

### 5.3.1   Bulk Water

In the first step of the evaluation of the 2PT method we performed simulations of bulk water and compared our findings with results of Jung et al. [198] and Pascal et al. [201], who had used the 2PT method, as well as to the prediction made on the basis of the theoretical model of Garza [188] and existing experimental data [201].

*Table 5.2: Comparison of bulk water molar entropies $S°$ computed with different methods and experimental data.*

| Method | $S°$ [J/mol K] |
|---|---|
| 2PT SPC | $65.4^a$ |
| 2PT ReaxFF | $59.3^b$ |
| 2PT TIP3P | $72.5^c$ |
| Garza | $53.1^d$ |
| Exp. | $69.9^e$ |

$^a$ This work, $^b$ Jung et al. [198], $^c$ Pascal et al. [201], $^d$ Garza [188], $^e$ Pascal et al. [201]

All values are shown in Table 5.2. The bulk water entropy values computed here are in good agreement with the experimental data. We note that we obtained better agreement with measurements than Jung et al. [198], who used different, reactive force field (ReaxFF), and the theoretical model of Garza [188]. On the other hand, the results obtained with the TIP3P water model give the closest agreement with the experiment. This indicates that the quality of the force-field in the water model plays a crucial role for achieving an acceptable accuracy of the prediction for the entropy of solvated species with the 2PT method.

## 5.3.2    Alcohol Molecules in Bulk Aqueous Solution

### 2PT vs. Experimental Data

To test further the performance of the 2PT method, we performed calculations of entropies of a set of simple alcohol molecules immersed in water. Figure 5.2 shows the comparison of computational results with experimental values. In comparison with the values observed in the gas phase, a significant reduction of entropies in the bulk water environment (>100 J/mol K) is observed in all cases. This expected result is owed to the confined space for free motion of solvated particles in solvent environment. The 2PT method reproduces measured molar entropies of simple alcohol species in aqueous solution, with deviations ranging from only 5 J/mol K ($\sim 5\%$) for methanol to 24 J/mol K ($\sim 10\%$) for larger alcohol molecules such as butanol. These results demonstrate the good ability of the 2PT method for calculating entropies of solvated molecules. Unlike previous chapters, here we adopted kJ/mol as the unit for energy instead of eV to ensure consistent comparisons with experimental results.
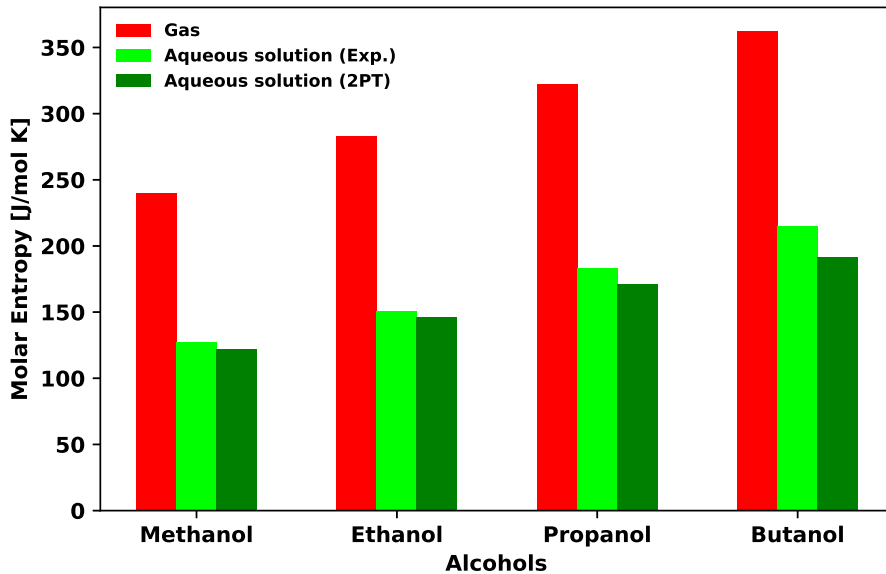
Figure 5.2: Molar entropy of simple alcohol molecules in gas and bulk water solution phase obtained from experiments (Exp.) [202] and using the 2PT method.

**2PT vs. Theoretical Solvation Model**

In Table 5.3 we compare the results obtained with the 2PT method with the prediction of the theoretical model of Garza [188]. Both approaches produce similar values

Table 5.3: Comparison of total bulk entropy, $S_{tot}$, and partial contributions: translational $S_{trans}$, vibrational $S_{vib}$, rotational $S_{rot}$ and cavity $S_{cav}$ entropies computed with the theoretical model of Garza [188], the 2PT method, and the measured values [202].

| Entropic | Methanol | | | Ethanol | | | Propanol | | | Butanol | | |
|---|---|---|---|---|---|---|---|---|---|---|---|---|
| Contribution [J/mol K] | Garza | 2PT | Exp. | Garza | 2PT | Exp. | Garza | 2PT | Exp. | Garza | 2PT | Exp. |
| $S_{trans}$ | 79.73 | 64.74 | - | 89.25 | 68.18 | - | 88.87 | 72.25 | - | 93.93 | 69.46 | - |
| $S_{vib}$ | 7.23 | 6.81 | - | 21.96 | 17.49 | - | 43.38 | 35.25 | - | 73.13 | 56.32 | - |
| $S_{rot}$ | 79.61 | 50.34 | - | 93.47 | 60.73 | - | 101.94 | 63.96 | - | 108.59 | 65.76 | - |
| $S_{cav}$ | -49.41 | - | - | -57.61 | - | - | -64.64 | - | - | -70.82 | - | - |
| $S_{tot}$ | 117.61 | 121.89 | 127.19 | 147.07 | 146.40 | 151.00 | 169.55 | 171.46 | 183.06 | 204.83 | 191.55 | 215.06 |

with deviation <5 J/mol K. Interestingly, similar to the 2PT method, the theoretical model also underestimates entropies in relation to experimental data. Although both approaches produce quantitatively similar entropy values, significant differences arise in the entropic contributions. While the total entropy calculated with the 2PT

method consists of vibrational, rotational and translational entropy contributions, the theoretical model includes an additional cavity entropy contribution, that takes into account the reorganization of the solvent environment to form the cavity for a solute. While this cavity entropy term is not explicitly included in the 2PT method, Persson et al. [203] demonstrated that the cavity formation entropy term is implicitly included in translational and rotational entropy terms of the 2PT method. This is the case because a solute, representing an impenetrable wall for solvent molecules, reduces the solvent diffusion coefficient. The reduction affects the movement of the solute, which results in a reduction of translational and rotational entropies. Consequently, the entropic contributions from rotations and translations, computed with the 2PT method, are consistently lower than translational and rotational entropies predicted by the theoretical model. In the case of methanol, the translational and rotational entropies are reduced by $\sim 15$ J/mol K, and $\sim 29$ J/mol K, respectively. These values sum up to the values similar to the cavity entropy predicted by the theoretical model. Our results thus support the interpretation of Persson et al. [203] that the cavity entropy is equivalent to the reduction of translational and rotational entropy.

### 5.3.3 Entropy of Alcohol Molecules at Metal-Solvent Interface

With promising results for the bulk aqueous phase using the 2PT method, we computed the entropy of alcohol species at three different metal-aqueous solvent interfaces, considering platinum (Pt), silver (Ag) and lead (Pb) metal surfaces. These cases were selected because these metal catalysts play a fundamental role in electrocatalysis [10]. The resulting interfacial entropies of alcohol species are compared to the entropy values computed for bulk water solvent in Figure 5.3. We see a further decrease in entropy at metal-solvent interface, compared to results for bulk water solvent. The largest reduction by $\sim 66$ J/mol K is observed for butanol at Pt surface. The reduction is only slightly smaller for methanol ($\sim 40$ J/mol K). Considering the different entropic contributions, the entropy reduction is largest for translational and rotational contributions. In the case of butanol on Pt, the translational and rotational entropies are decreased by $\sim 25$ J/mol K and $\sim 30$ J/mol K, respectively, while the reduction of vibrational entropy is about half that value ($\sim 11$ J/mol K). Most of
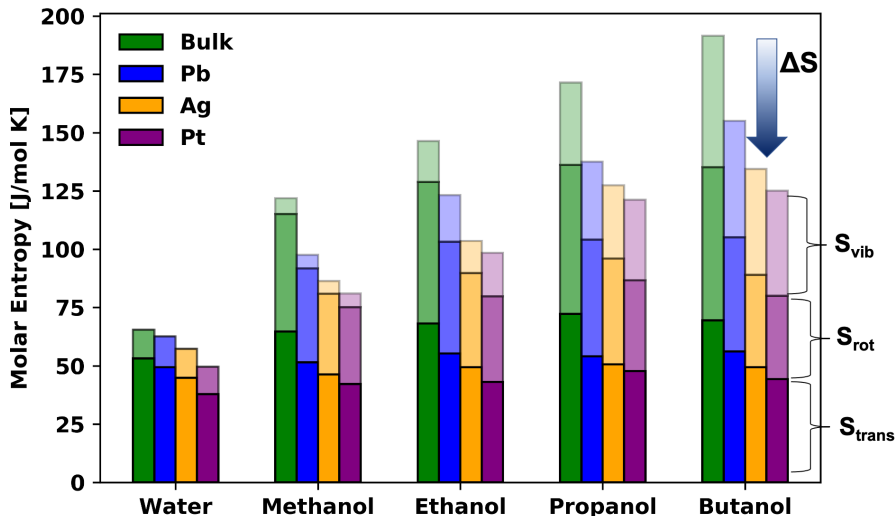
Figure 5.3: Molar entropies of several alcohol molecules in bulk water and at different metal interfaces (Pt, Ag, Pb) computed with the 2PT method. Translational $S_{trans}$, rotational $S_{rot}$ and vibrational $S_{vib}$ entropy contributions are marked with different shades of colors. For water, the vibrational contribution is negligible, $< 0.1$ J/mol/K [198], and not shown.

the entropy reduction is caused by the reduced cavity space at the interface, which reduces further the translational and rotational motion at the metal surface. Due to the stronger interaction of large alcohol molecules with the surface, the entropy reduction effect is greater for butanol than for smaller alcohol species, e.g., methanol. We note that the existence of significant translational entropy at the interface is caused by surface diffusion of the molecular species, as also simulated by Heenen et al. [73] and Kholmurodov et al. [204].

Regarding different metal surfaces, we identify a trend in entropy reduction at Pb, Ag and Pt surfaces. The entropy reduction is highest for Pt, followed by Ag and Pb metal surfaces. For instance, butanol experiences an entropy loss of $\sim 66$ J/mol K at Pt surface, but only $\sim 57$ J/mol K and $\sim 36$ J/mol K at the Ag and Pb surfaces, respectively. This trend is also observed in the molar entropy of water, as seen on the left in Figure 5.3.

In order to obtain a more detailed understanding of differences in entropies of species at different metal surfaces, we evaluate the following descriptors: (1) the water adsorption interaction energy on the metal surface, (2) the water density distribution at the interface and (3) the hydration shell of alcohol species. The water adsorption

*Table 5.4: Adsorption energy of water molecule on Pt(111), Ag(111) and Pb(111) surfaces computed with DFT and IFF methods.*

| Metal surface | H$_2$O adsorption energy [kJ/mol] | |
| | DFT | IFF |
| --- | --- | --- |
| Pt | 26.0 | 23.5 |
| Ag | 12.5 | 19.4 |
| Pb | 7.7 | 10.5 |

energy is computed from

$$E_{\text{ads}} = E_{\text{H}_2\text{O+surface}} - E_{\text{surface}} - E_{\text{H}_2\text{O}}, \tag{5.18}$$

where $E_{\text{H}_2\text{O+surface}}$, $E_{\text{surface}}$, $E_{\text{H}_2\text{O}}$ correspond to the energy of H$_2$O adsorbed on the metal surface, the energy of bare metal surface and the energy of isolated H$_2$O, respectively. Table 5.4 shows the water adsorption energy on Pt, Ag and Pb metal surfaces computed with DFT and IFF methods. The values obtained indicate that water adsorbs most strongly on the Pt surface. The Pb surface is known to have a hydrophobic tendency [142], which is reflected in the low water adsorption energy. As a result, the solvent environment is located at a greater distance from the metal surface, leading to an enlarged cavity confining the solute. On the other hand, for Pt, water molecules are located at closer distance from the surface, decreasing the size of the solute cavity and further reducing the entropy. Figure 5.4 illustrates how the strength of water adsorption affects the solute cavity and thus the entropy of solvated species at the interface. In the bulk phase, water molecules create a cavity around the solute. At close proximity to the metal surface, the number of water molecules surrounding the solute molecule is reduced. As the solute and its surrounding water molecules are located closer to the surface for Pt than for Pb and Ag, the resulting solute cavity is smaller in the former case, as depicted in Figure 5.4, resulting in a more pronounced entropy reduction relative to the bulk solvent.

We further support our argument with the analysis of water density distributions at Pt, Ag and Pb metal surfaces, illustrated in Figure 5.5. The distributions reveal a
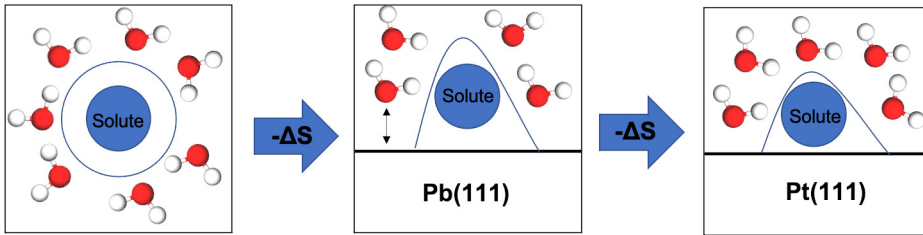
Figure 5.4: Schematic illustration of solute entropy reduction from bulk to Pb and Pt surface due to reduced cavity size.
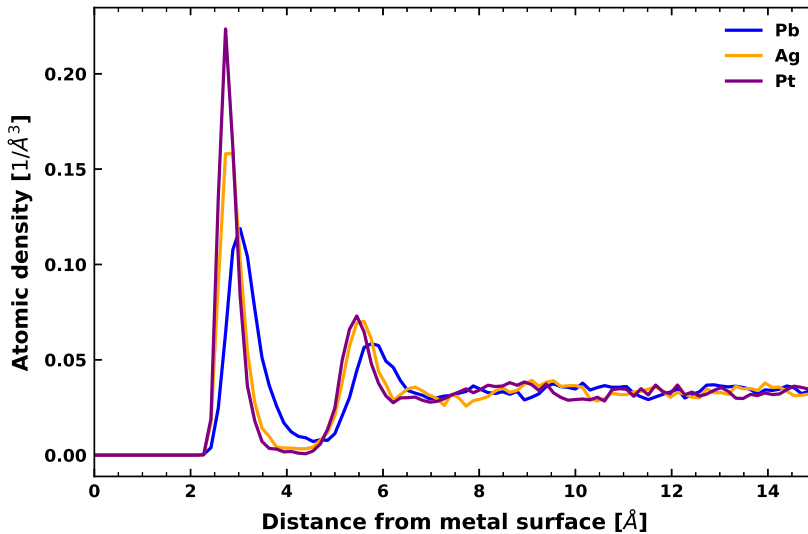


Figure 5.5: Water density distribution at the Pb(111), Ag(111) and Pt(111) surface.

shift and an associated increase in the magnitude of the first peak, that confirms the shorter water-metal distance and stronger water-metal interaction in the case of Pt as compared to the cases of Ag and Pb interfaces.

In order to get a better idea of the solute hydration shell and its effect on the entropy, in Figure 5.6(a) we plotted the radial distribution functions (RDF) of butanol with respect to water oxygen atoms. In the case of RDF for butanol-water oxygen (O-$O_w$), going from Pt to Pb surfaces we observe a shift of the first peak, which

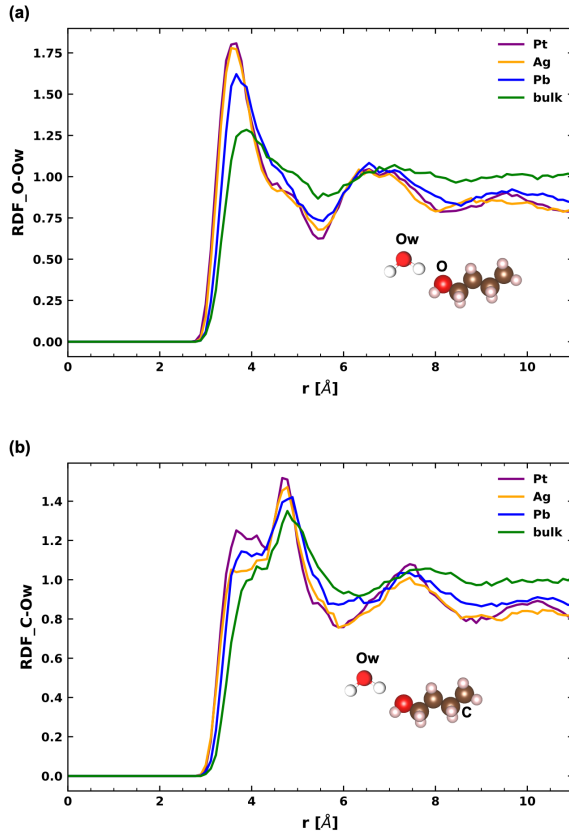*Figure 5.6: RDFs between water oxygen ($O_w$) and (a) butanol oxygen (O) and (b) butanol carbon (C) at bulk solution, Pb surface, Ag surface and Pt surface.*

demonstrates shorter butanol-water distance for the Pt metal case and thus a smaller solute cavity. When comparing with the bulk solution case, we observe an increase in the height of the first RDF peak, with the highest peak observed for Pt. This reveals the correlation between the solute-solvent RDF and the solute entropy. Integrating the first oxygen-oxygen RDF peak provides a qualitative picture of the structure of the first hydration shell of butanol, including the number of water molecules reported in Table 5.5. Interestingly, butanol has the largest number of water molecules in the first hydration shell on Pt, followed by the other metal surfaces and the bulk solution having the smallest number. This indicates that a larger hydration shell translates

Table 5.5: *Number of water molecules in the first hydration shell of butanol obtained from* $O$-$O_w$ *and* $C$-$O_w$ *RDFs for Pt, Ag, Pb surfaces and bulk aqueous solution.*

| Solute environment | No. of water molecules in first hydration shell | |
| --- | --- | --- |
| | $O$-$O_w$ | $C$-$O_w$ |
| Pt | 2.72 | 2.96 |
| Ag | 2.65 | 2.85 |
| Pb | 2.58 | 2.87 |
| bulk | 2.40 | 2.64 |

to a greater reduction in entropy. A similar trend is observed for the RDF of butanol carbon and water oxygen atoms (Table 5.5 & Figure 5.6(b)), where the first peak of the RDF is shifted more towards the surface for Pt case, compared to other metals and the bulk solution.

Summarizing the above findings, we associate the metal-dependent entropy reduction with specific differences in the interaction of water with distinct metal surfaces, which affects the hydration shell of adsorbed solutes. This causes a change in the size of the solute cavity and the value of the entropy.

### 5.3.4 Impact of Solvation Entropy on Surface Chemistry

In order to show the impact of the derived interfacial entropy contributions on the free energies of the interfacial reactions involving alcohol desorption, we have calculated the associated change of the free energies ($T\Delta S$) between species at the interface and in the bulk solvent, at a temperature of 300 K. The results are displayed in Figure 5.7. The effect varies between different metal surfaces and increases with the size of the alcohol molecule. The resulting difference can be of importance when describing interface chemistry, as 20 kJ/mol, the largest observed difference in the free energy, could translate to a change in the rate constant of the reaction by three orders of magnitude.

In order to illustrate the impact of the solvent entropy on thermodynamic parameters of a chemical reaction, we calculated the Gibbs free energy ($G$) of the ethanol adsorption process on Pt(111), considering gas or a solvent environment. Calculations were performed at the DFT level, applying the implicit solvation scheme to compute the enthalpy of solvation.

The results are provided in Table 5.6. We also derived the resulting change in the rate constant of the reaction by applying the Arrhenius equation.
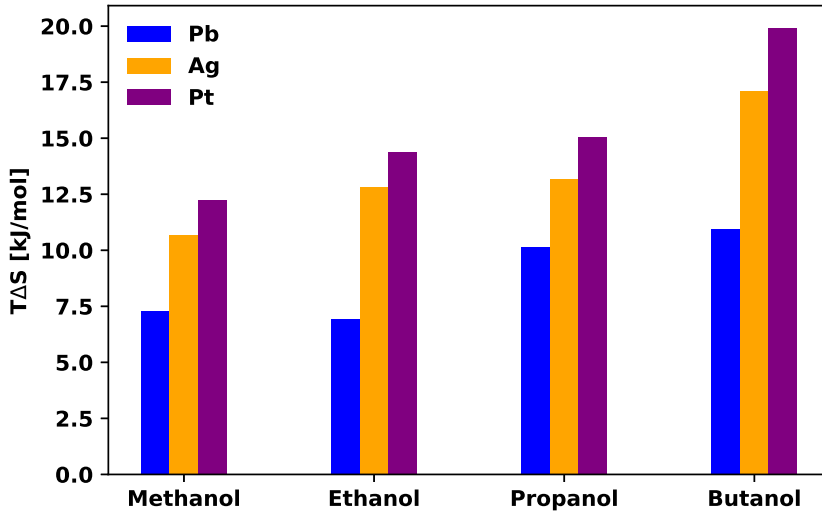
*Figure 5.7: Contributions of solvation entropies of alcohol molecules at different metal surface to the Gibbs free energies, using the values computed for the bulk solvent environment as reference. The results are given for temperature of 300 K.*
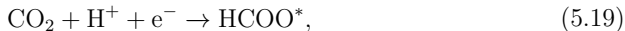
*Table 5.6: Change in Gibbs free energy G and reaction rate constant k (using gas case as reference) for ethanol adsorption on Pt(111) surface in gas and solvent environment. Adsorption process of ethanol is defined as $C_2H_5OH + * \rightarrow C_2H_5OH*$, where * represents the Pt(111) surface. $C_2H_5OH*$ indicates the adsorbed state of ethanol.*

| Case n | Environmental setting | $\Delta$ G [eV] | $\frac{k_n}{k_1}$ |
|--------|----------------------|-----------------|-------------------|
| 1 | $\Delta H_{\mathrm{gas}}, \Delta S_{\mathrm{gas}}$ | 0.54 | - |
| 2 | $\Delta H_{\mathrm{sol}}, \Delta S_{\mathrm{gas}}$ | 0.28 | $>10^5$ |
| 3 | $\Delta H_{\mathrm{sol}}, \Delta S_{\mathrm{sol}}$ | -0.40 | $>10^{15}$ |

Using the gas environment as the reference, the solvation effects on enthalpy reduces $\Delta G$ of reaction by 0.26 eV. When we additionally consider the impact of solvent environment on the entropy, $\Delta G$ is reduced by 0.94 eV. Such a large number leads to a fifteen orders of magnitude change in the reaction constant. This clearly shows that the solvation effects on enthalpy and entropy have a huge influence on the reaction rate. The change in Gibbs free energy is primarily influenced by the

solvation entropy effect.

In the next step, we have applied the same analysis to a reaction process, i.e., $CO_2$ reduction reaction towards HCOO* (reaction intermediate) on the Pb(100) surface,

$$CO_2 + H^+ + e^- \rightarrow HCOO^*, \tag{5.19}$$

where $CO_2$ and a proton react to adsorbed HCOO.

The results are shown in Table 5.7. We observe the same trend as in the case of

Table 5.7: Change in Gibbs free energy G and reaction rate constant, k, (using gas phase values as the reference) for $CO_2$ reduction reaction towards HCOO* on the Pb(100) surface. The reaction pathway is given in Eq.(4.11). The subscripts "gas" and "sol" indicate enthalpy (H) and entropy (S) contributions computed assuming gas and solvent environments.

| Case n | Environmental setting | $\Delta$ G [eV] | $\frac{k_n}{k_1}$ |
|--------|-----------------------|-----------------|-------------------|
| 1 | $\Delta H_{gas}$, $\Delta S_{gas}$ | 0.49 | - |
| 2 | $\Delta H_{sol}$, $\Delta S_{gas}$ | 0.31 | $>10^4$ |
| 3 | $\Delta H_{sol}$, $\Delta S_{sol}$ | -0.53 | $>10^{17}$ |

ethanol adsorption. The Gibbs energy of reaction decreases by 1.02 eV from case 1 to case 3, increasing the reaction rate by many orders of magnitude. This further demonstrates the importance of solvation effects for chemistry on metal surfaces.

## 5.3.5 Alcohol Molecules in Bulk Toluene

In order to test the applicability of 2PT approach to other solvents than water we applied the method to alcohol molecules in toluene solution. The results for the bulk solvent phase are shown in Figure 5.8. The agreement with experimental data is not as good as in the case of water as solvent (Fig. 5.2). The 2PT method underestimates the solvent entropy by $\sim 20\%$, predicting a stronger reduction in bulk toluene as found in the experiment. However, the trend of an increasing entropy with increasing size of the alcohol molecule is consistent with experimental data. The poorer performance of the 2PT method for toluene used as a solvent may reflect the quality of the force field used in the description of the solute-solvent system. The force fields applied to describe aqueous solutions have a long history of developments, with the applied SPC water model being specifically designed for simulation of water and thus quite accurately predicting various structural and thermodynamic properties
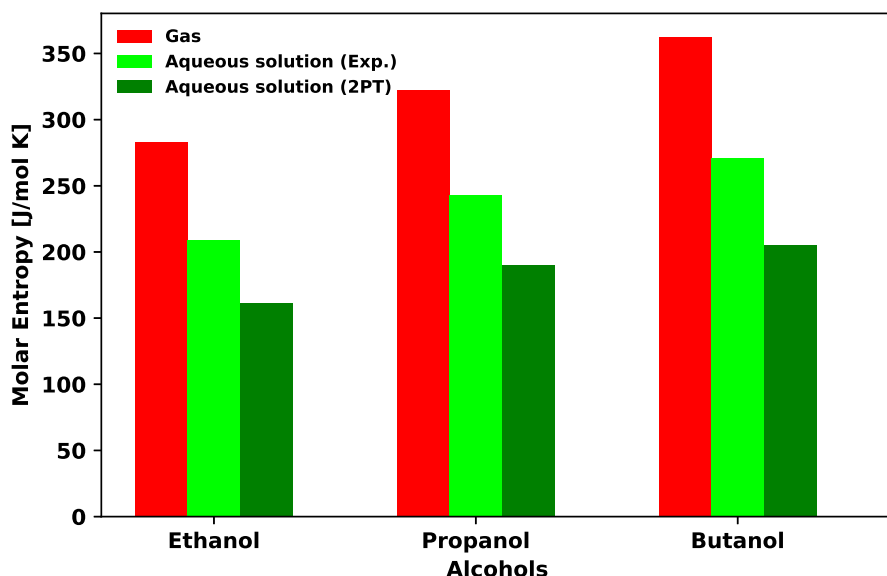
*Figure 5.8: Molar entropies of different alcohols in gas or bulk toluene solution phases, obtained from experiments (Exp.) and using the 2PT method.*

[192, 205], including water bulk entropy as discussed in Section 5.3.2. The force-field applied here for the to toluene-based solution is a general OPLS AA/L force field [95], not specifically designed to model that system. In order to assess the sensitivity of predictions made on the basis of the 2PT method to the force field parametrization, we performed simulations with other force fields: the generalized Amber force field (GAFF) [206], flexible OPLS [207], TraPPE [208] and KBFF [209]. We note that while GAFF as well as OPLS AA/L are all-atom force fields, where parameters are provided for each single atom, the remaining three force fields (flexible OPLS, TraPPE and KBFF) are united-atom force fields that represent groups of atoms by pseudo-atoms, enabling a reduced effort of parametrization of the force field and a faster computation time. Table 5.8 shows the molar entropies of ethanol in toluene computed using the 2PT method for the considered force fields. We notice a large spread of resulting values. While the KBFF, GAFF and OPLS AA/L force fields underestimate the molar entropy of ethanol in toluene, the flexible OPLS and TraPPE force fields overestimate the values, with TraPPE force field giving best match to the measured values. On the

Table 5.8: Molar entropies of ethanol in bulk toluene solvent computed using different force field methods. Exp. is the experimental entropy value.

| Method | $S$ [J/mol K] |
|---|---|
| OPLS AA/L | 161.38 |
| GAFF | 160.36 |
| Flexible OPLS | 343.06 |
| TraPPE | 212.60 |
| KBFF | 148.25 |
| Exp. | 209.00 |

other hand, both all-atom force fields result in very similar entropy values, while the united-atom force fields show spread in a range of 200 J/mol K. These results clearly shows a sensitivity of the 2PT method to the quality of the force field, indicating that either system-design specific force field model, like in the case of water, or *ab initio* molecular dynamics simulations should be performed to obtain accurate values of the entropy of solutes in a solvent system.

Realizing that the OPLS AA/L force field applied here is not specifically designed to simulate the toluene system, we also check what modifications of force field parameters are required for the 2PT method to match experimental data for the entropy of ethanol in toluene. In the OPLS AA/L force field, the main part of the non-bounding interaction between atoms is described by the Lennard-Jones and Coulomb interaction potentials. We assumed standard definitions of these interactions, for the Lennard-Jones interaction,

$$V_{LJ}(r) = 4\epsilon \left[ \left( \frac{\sigma}{r} \right)^{12} - \left( \frac{\sigma}{r} \right)^{6} \right], \tag{5.20}$$

where $\sigma$ and $\epsilon$ are the standard Lennard-Jones parameters and $r$ is the distance between the interacting particles, and the Coulomb potential,

$$V_{Coulomb}(r) = \frac{q_i q_j}{\epsilon_a r} \tag{5.21}$$

where $q_{i/j}$ are the charges of interacting particles $i$ and $j$, and $\epsilon_a$ is the dielectric constant.

Figure 5.9 shows the sensitivity of entropy values obtained with the 2PT method to the parameters $\sigma$, $\epsilon$ and $q$. First, we note that an increase or decrease in $\sigma$ decreases

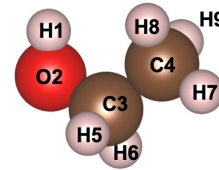| Case | $\epsilon$ [kcal/mol] | $\sigma$ [Å] | $q$ [C] | S [J/mol K] |
|------|------------------------|----------------|----------|-------------|
| Ref. | $\epsilon_2$=0.17 | $\sigma_2$=3.12 | $q_1$=+0.407, $q_2$=-0.6915 | 161.38 |
| 1 | - | $\sigma_2$=5.12 | - | 161.18 |
| 2 | - | $\sigma_2$=1.12 | - | 132.15 |
| 3 | $\epsilon_2$=0.07 | - | - | 167.13 |
| 4 | - | - | $q_1$=+0.001, $q_2$=-0.001 | 172.25 |
| 5 | $\epsilon_{1-9}$=0.0001 | - | $q_1$=+0.001, $q_2$=-0.001, $q_{3-9}$=0 | 204.83 |
| Exp. | - | - | - | 209.00 |



*Figure 5.9: Force field parameters for ethanol in toluene solvent environment. Ref. case is the original case shown in Figure 5.8 and changes in the parameters are made from cases 1-5. Exp. indicates the experimentally measured entropy of ethanol in toluene. Number in the subscripts represents the type of atom for which an interaction parameter has been modified, using right figure as a reference.*

the entropy. On the other hand, a simultaneous decrease in $\epsilon$ and $q$ parameters increases the entropy, bringing it closer to the experimental value. The latter implies that a stronger repulsive interaction between ethanol and toluene, and thus formation of bigger solute cavities is required to quantitatively match experimental data. This points towards the force-field parametrization as a main factor determining the accuracy of simulations of entropies in a solute-solvent system with the 2PT method.

## 5.4  Summary

In this work, we have tested the feasibility of the 2PT method to predict the entropies of alcohol molecules in aqueous and organic solvents. Calculations have been performed for bulk solvent as well as solvent-metal interfaces. Combining the 2PT method with computationally efficient CMD simulations, we have been able to reproduce measured entropies of alcohol molecules submerged in bulk water with high accuracy. We have noticed that when these alcohol molecules are placed at the metal-electrolyte interface, molar entropies can undergo a significant decrease by more than 30% relative to the values obtained for bulk water. We attribute this decrease to the lowering of the translational and rotational entropies of molecular species at metal-solvent interfaces. The largest reduction in entropy has been observed for the case of the Pt surface, which we explain by this surface having the strongest interaction with

water molecules, relative to the Pb and Ag surfaces. The strong interaction results in a smaller solute cavity and thus reduced entropy. We have shown the non-negligible effect of the entropy change on the Gibbs energy of alcohol adsorption and on the $CO_2$ reduction reaction pathway at the metal-water interface, which can lead to a drastic change in the reaction rate by several orders of magnitude.

We have also evaluated the performance of the 2PT method for toluene, an organic liquid solvent. For this solvent, larger differences from measured values are observed and these are attributed to the inaccuracy of OPLS AA/L force field used to describe interactions between alcohol molecules and toluene. To scrutinize this effect, we have tested different available force-fields, observing a significant spread in computed solvation entropies. These results underpin the need using force-field parameters specifically determined for the compounds of interest to accurately calculate solvation entropies.

Our study clearly shows that the 2PT method in combination with classical molecular dynamics simulations provides a computationally sound approach to calculating entropies of solvated species, as long as accurate force fields are available. When compared with the prediction of the independent theoretical models, the approach yields valuable and reliable information on entropy changes in bulk as well as at metal-solution interfaces; it can help validate theoretical models. As solvation effects have been usually neglected in modeling of electrochemical interfaces, the presented results are anticipated to pave the way for more realistic and accurate simulations of chemical processes at electrochemical interfaces.

# Chapter 6

# Conclusions and Outlook

In this thesis, I have computationally studied the impact of solvation phenomena at metal-electrolyte interfaces. Since many electrocatalytic reactions, i.e., $CO_2$ reduction reactions, occur at the metal-electrolyte interface, an efficient and complete description to model the interface is required in order to save time and costs in improving existing energy materials and finding new energy materials. Due the existence of significant knowledge gaps of metal-electrolyte interface modeling, I have addressed various research questions which had remained unanswered with respect to incorporating solvation models at the metal-electrolyte interface.

In Chapter 3, I have compared interface force field (IFF)-based classical molecular dynamics (CMD) simulations with *ab initio* molecular dynamics (AIMD) simulations of water structures at Pb(100) and (111) metal surface. While AIMD is known to be more accurate than CMD simulations, water structures obtained using the IFF are in good agreement with AIMD simulations. In addition, CMD simulations are capable of running for a much longer time than AIMD (ns and longer vs. ps), obtaining equilibrated water structures that cannot be obtained using the more computationally expensive AIMD approach. With this work, I have demonstrated the potential of using IFF-based CMD simulations for realistic equilibration and sampling of water structures on metal surfaces.

In Chapter 4, a systematic study on the role of different solvation models of $CO_2$ reduction reaction on Pb(100) and Ag(100) catalyst towards HCOOH and CO products is performed. Explicit solvation impacts the adsorption energy of crucial reaction intermediates on a much greater scale than implicit solvation. This is due to the ability of explicit solvation to account for H-bonding effects, which I have identified as

the primary factor influencing the adsorption energy. Applying explicit solvation onto the $CO_2$ reduction reaction on Pb(100) and Ag(100) catalyst, I was able to identify CO as the main product for Ag and HCOOH as the main product for Pb catalyst. To my knowledge, this is the first computational demonstration of accurately predicting the primary products of the $CO_2$ reduction reaction on both Ag and Pb catalysts while accounting for solvation effects. These findings indicate that explicit solvation is an important tool for accurately describing $CO_2$ reduction reactions occurring at metal-electrolyte interfaces. However, incorporating explicit solvation comes along with a certain amount of sensitivity and requires careful consideration to yield correct predictions.

In Chapter 5, I have applied the Two Phase Thermodynamic (2PT) model to assess the accuracy and computational efficiency of solute entropies in solvent bulk environment as well as in metal-electrolyte environment. The 2PT method not only yields quantitative agreement with experimental data (assuming a suitable force field is used), but also demonstrates that a mere 20 ps of CMD simulation is sufficient to obtain this level of agreement. The solute entropy decreases in the vicinity of the metal surface compared the bulk environment, which can be attributed to the reduction in both translational and rotational entropy. Considering the accuracy and computational efficiency of the 2PT method, further investigation of the impact of solvent entropies on the calculation of Gibbs free energies and its respective reaction rates for certain adsorption/reaction processes, i.a. $CO_2$ reduction reaction, is performed. The examination of the $CO_2$ reduction reaction on Pb(100) demonstrated that the use of solvent models with entropy values calculated from the 2PT method can cause the reaction rate to vary by up to $10^{17}$ compared to commonly-used gas models. Thus, this work has shown that the 2PT method can be used to efficiently and accurately obtain solvent entropies, which are crucial for an accurate description of Gibbs free energies at metal-electrolyte interfaces.

Summarizing all three works, significant contributions in advancing computational understanding of how to incorporate solvation effects for a more efficient and complete description of the metal-electrolyte interface have been made. Nevertheless, all three works have highlighted certain aspects that need more attention for further advancements in the realm of computational electrocatalysis in solvent environment.

With the application of IFF-based CMD simulations of water structures on metal surfaces, I have shown the potential of using classical methods to analyze struc-

tural properties at the complex interface compared to the computationally demanding AIMD method. Especially, with more attention shifting towards computation of solvent effects, an advancement in the classical force field development for the electrode-electrolyte interface, such as incorporating polarization effects or employing machine-learning techniques for force field parameterization, is highly desirable and has the potential to transform CMD from a mere sampling tool into a valuable tool for conducting complex analyses.

In the second project, the significance of using explicit solvation for reactions at the metal-electrolyte interface is demonstrated using a combined multiscale modeling approach. Correct computational predictions of $CO_2$ reduction reaction products underline the importance of including solvent moleules explicitly, but the results also show the limitations of applying implicit solvation models for reactions at the interface. Thus, for an accurate application of implicit solvation at the metal-electrolyte interface, further improvements of implicit solvent models are desirable. Future works should include additional computations at the metal-electrolyte interface comparing implicit solvation methods with explicit solvation methods, given the scarcity of such important benchmark studies. This will shed additional light on whether using solely implicit solvation is unnecessary and can be disregarded, or if greater emphasis should instead be placed on how implicit solvation in combination with explicit solvation can act as a versatile tool to represent counter charges for constant potential calculations. With the above work, I have also stressed the importance of using a multiscale modeling approach to predict product selectivites more accurately. Hence, future computational works at metal-electrolyte interfaces should extend beyond pure DFT computations, which oftentimes only yield qualitative predictions. It should include microkinetic modeling in combination with parameters obtained from DFT calculations to achieve a more quantitative comparison with experimental data.

Lastly, in the third project, the significance of solvent entropy effects on adsorption/reaction processes is stressed. By including entropic contributions, reaction rates can vary up to several orders of magnitude compared to the simplified gas model. Thus, in the future more attention needs to be paid to solvent entropy contributions towards computation of the Gibbs free energy of reactions at the metal-electrolyte interface. As the presented 2PT method in combination with CMD simulation has shown to be computationally efficient in predicting adsorbate entropies at the metal-electrolyte interface, this method should be employed and extended to other existing

computational works dealing with $CO_2$ reduction at the metal-solvent interface, in order to further evaluate the applicability of the 2PT method across various metal-solvent interfaces.

With that being said, applying solvation effects to the electrode-electrolyte interface is not a straightforward task and more efforts need to be undertaken to establish consensus on what solvation model is the most appropriate one to use at the electrochemical interface considering factors such as accuracy, computational cost, and applicability. In the distant future, as supercomputing power continuously increase, AIMD computations of larger and more complex systems are expected to be the preferred approach. However, in the meantime, the importance of other more computationally efficient solvation methods, as presented in this thesis, remains just as crucial for a more reliable atomistic modeling of the electrochemical interface.

From a theoretical standpoint, solvation only plays one crucial part of the complete computational understanding of the metal-electrolyte interface. Future theoretical works could also include the additional incorporation of charged interfaces to further improve the simulation of realistic experimental electrochemical conditions, i.a, electrochemical reactions under constant potential conditions. Furthermore, experimental collaboration is highly desired in order to validate and asses our simulation results on a more quantitative level. With the continuously increasing computational power of supercomputers, simulations of larger and more complex system become possible, further narrowing the gap between experimental observations and atomistic simulations.

# Bibliography

[1] European Commission, Directive (EU) 2018/2001 of the European Parliament and of the Council of 11 December 2018 on the promotion of the use of energy from renewable sources (recast), 2018.

[2] T. P. Barnett, J. C. Adam, D. P. Lettenmaier, Potential impacts of a warming climate on water availability in snow-dominated regions, Nature 438 (7066) (2005) 303–309.

[3] C. Mora, B. Dousset, I. R. Caldwell, F. E. Powell, R. C. Geronimo, C. R. Bielecki, C. W. W. Counsell, B. S. Dietrich, E. T. Johnston, L. V. Louis, M. P. Lucas, M. M. McKenzie, A. G. Shea, H. Tseng, T. W. Giambelluca, L. R. Leon, E. Hawkins, C. Trauernicht, Global risk of deadly heat, Nat. Clim. Change 7 (7) (2017) 501–506.

[4] IPCC, Global Warming of 1.5°C: IPCC Special Report on Impacts of Global Warming of 1.5°C above Pre-industrial Levels in Context of Strengthening Response to Climate Change, Sustainable Development, and Efforts to Eradicate Poverty, Cambridge University Press, 1 edn., 2022.

[5] Paris Agreement, UN Treaty, Treaty No. XXVII-7-d, 2015.

[6] E. Commission, D.-G. for Energy, J. Yearwood, L. Korteweg, T. Smit, K. Rademaekers, D. Seebach, A. Hermann, J. Dieroff, T. Stojanovic, M. Wingenbach, C. Timpe, V. Bürger, K. Hennenberg, M. Altmann, M. Zerta, P. Schmidt, T. Gleiter, Technical assistance for assessing options to establish an EU-wide green label with a view to promote the use of renewable energy coming from new installations : final report, Publications Office, 2021.

[7] J. Wilcox, Carbon Capture, Springer Science & Business Media, ISBN 978-1-4614-2215-0, 2012.

[8] J. R. Fanchi, C. J. Fanchi, Energy in the 21st Century, World Scientific, ISBN 978-981-314-477-4, 2016.

[9] S. Nitopi, E. Bertheussen, S. B. Scott, X. Liu, A. K. Engstfeld, S. Horch, B. Seger, I. E. L. Stephens, K. Chan, C. Hahn, J. K. Nørskov, T. F. Jaramillo, I. Chorkendorff, Progress and Perspectives of Electrochemical $CO_2$ Reduction on Copper in Aqueous Electrolyte, Chem. Rev. 119 (12) (2019) 7610–7672.

[10] Y. Hori, Electrochemical $CO_2$ Reduction on Metal Electrodes, in: C. G. Vayenas, R. E. White, M. E. Gamboa-Aldeco (Eds.), Modern Aspects of Electrochemistry, vol. 42, Springer New York, 89–189, 2008.

[11] Y. Hori, K. Kikuchi, S. Suzuki, Production of CO and $CH_4$ in electrochemical reduction of $CO_2$ at metal electrodes in aqueous hydrogencarbonate solution, Chem. Lett. 14 (1985) 1695–1698.

[12] IEA, The Future of Hydrogen, https://www.iea.org/reports/the-future-of-hydrogen, license: CC BY 4.0, 2019.

[13] M. Jouny, W. Luc, F. Jiao, General Techno-Economic Analysis of $CO_2$ Electrolysis Systems, Ind. Eng. Chem. Res. 57 (6) (2018) 2165–2177.

[14] Z. Yang, F. E. Oropeza, K. H. L. Zhang, P-block metal-based (Sn, In, Bi, Pb) electrocatalysts for selective reduction of $CO_2$ to formate, APL Mater. 8 (6) (2020) 060901.

[15] Y. Ma, J. Wang, J. Yu, J. Zhou, X. Zhou, H. Li, Z. He, H. Long, Y. Wang, P. Lu, J. Yin, H. Sun, Z. Zhang, Z. Fan, Surface modification of metal materials for high-performance electrocatalytic carbon dioxide reduction, Matter 4 (3) (2021) 888–926.

[16] M. Fan, S. Garbarino, G. A. Botton, A. C. Tavares, D. Guay, Selective electroreduction of $CO_2$ to formate on 3D [100] Pb dendrites with nanometer-sized needle-like tips, J. Mater. Chem. A 5 (39) (2017) 20747–20756.

[17] X. An, S. Li, A. Yoshida, T. Yu, Z. Wang, X. Hao, A. Abudula, G. Guan, Bi-Doped SnO Nanosheets Supported on Cu Foam for Electrochemical Reduction of $CO_2$ to HCOOH, ACS Appl. Mater. Interfaces 11 (45) (2019) 42114–42122.

[18] T. T. H. Hoang, S. Verma, S. Ma, T. T. Fister, J. Timoshenko, A. I. Frenkel, P. J. A. Kenis, A. A. Gewirth, Nanoporous Copper–Silver Alloys by Additive-Controlled Electrodeposition for the Selective Electroreduction of $CO_2$ to Ethylene and Ethanol, J. Am. Chem. Soc. 140 (17) (2018) 5791–5797.

[19] J. K. Nørskov, T. Bligaard, J. Rossmeisl, C. H. Christensen, Towards the computational design of solid catalysts, Nat. Chem 1 (1) (2009) 37–46.

[20] T. Germann, P. Lomdahl, Recent advances in large-scale atomistic materials simulations, Comput Sci Eng 1 (2) (1999) 10–11.

[21] W. Zheng, Research trend of large-scale supercomputers and applications from the TOP500 and Gordon Bell Prize, Sci. China Inf. Sci. 63 (7) (2020) 171001.

[22] J. K. Nørskov, J. Rossmeisl, A. Logadottir, L. Lindqvist, J. R. Kitchin, T. Bligaard, H. Jónsson, Origin of the Overpotential for Oxygen Reduction at a Fuel-Cell Cathode, J. Phys. Chem. B 108 (46) (2004) 17886–17892.

[23] J. K. Nørskov, F. Abild-Pedersen, F. Studt, T. Bligaard, Density functional theory in surface chemistry and catalysis, Proceedings of the National Academy of Sciences 108 (3) (2011) 937–943.

[24] J. K. Nørskov, T. Bligaard, A. Logadottir, J. R. Kitchin, J. G. Chen, S. Pandelov, U. Stimming, Trends in the Exchange Current for Hydrogen Evolution, J. Electrochem. Soc. 152 (3) (2005) J23.

[25] J. S. Yoo, R. Christensen, T. Vegge, J. K. Nørskov, F. Studt, Theoretical Insight into the Trends that Guide the Electrochemical Reduction of Carbon Dioxide to Formic Acid, ChemSusChem 9 (4) (2016) 358–363.

[26] A. J. Medford, A. Vojvodic, J. S. Hummelshøj, J. Voss, F. Abild-Pedersen, F. Studt, T. Bligaard, A. Nilsson, J. K. Nørskov, From the Sabatier principle to a predictive theory of transition-metal heterogeneous catalysis, J. Catal. 328 (2015) 36–42.

[27] J. T. Feaster, C. Shi, E. R. Cave, T. Hatsukade, D. N. Abram, K. P. Kuhl, C. Hahn, J. K. Nørskov, T. F. Jaramillo, Understanding Selectivity for the Electrochemical Reduction of Carbon Dioxide to Formic Acid and Carbon Monoxide on Metal Electrodes, ACS Catal. 7 (7) (2017) 4822–4827.

[28] S. Ringe, N. G. Hörmann, H. Oberhofer, K. Reuter, Implicit Solvation Methods for Catalysis at Electrified Interfaces, Chem. Rev. 122 (12) (2022) 10777–10820.

[29] K. P. Kuhl, T. Hatsukade, E. R. Cave, D. N. Abram, J. Kibsgaard, T. F. Jaramillo, Electrocatalytic Conversion of Carbon Dioxide to Methane and Methanol on Transition Metal Surfaces, J. Am. Chem. Soc. 136 (40) (2014) 14107–14113.

[30] P. Quaino, F. Juarez, E. Santos, W. Schmickler, Volcano plots in hydrogen electrocatalysis – uses and abuses, Beilstein J. Nanotechnol. 5 (2014) 846–854.

[31] A. A. Peterson, J. K. Nørskov, Activity Descriptors for $CO_2$ Electroreduction to Methane on Transition-Metal Catalysts, J. Phys. Chem. Lett. 3 (2) (2012) 251–258.

[32] N. Karmodak, S. Vijay, G. Kastlunger, K. Chan, Computational Screening of Single and Di-Atom Catalysts for Electrochemical $CO_2$ Reduction, ACS Catal. 12 (9) (2022) 4818–4824.

[33] B. Xiong, Y. Yang, J. Liu, Z. Hua, Y. Yang, Electrocatalytic reduction of $CO_2$ to C1 products over bimetal catalysts: A DFT screening study, Fuel Process. Technol. 233 (2022) 107315.

[34] A. Bagger, W. Ju, A. S. Varela, P. Strasser, J. Rossmeisl, Electrochemical $CO_2$ Reduction: A Classification Problem, ChemPhysChem 18 (22) (2017) 3266–3273.

[35] H. Jing, P. Zhu, X. Zheng, Z. Zhang, D. Wang, Y. Li, Theory-oriented screening and discovery of advanced energy transformation materials in electrocatalysis, Advanced Powder Materials 1 (1) (2022) 100013.

[36] F. Li, Q. Tang, Understanding trends in the activity and selectivity of bi-atom catalysts for the electrochemical reduction of carbon dioxide, J. Mater. Chem. A 9 (13) (2021) 8761–8771.

[37] J. K. Pedersen, T. A. A. Batchelor, A. Bagger, J. Rossmeisl, High-Entropy Alloys as Catalysts for the $CO_2$ and CO Reduction Reactions, ACS Catal. 10 (3) (2020) 2169–2176.

[38] X. Nie, M. R. Esopi, M. J. Janik, A. Asthagiri, Selectivity of $CO_2$ Reduction on Copper Electrodes: The Role of the Kinetics of Elementary Steps, Angew. Chem. 125 (9) (2013) 2519–2522.

[39] L. Li, A. Ozden, S. Guo, F. Arquer, C. Wang, M. Zhang, J. Zhang, H. Jiang, W. Wang, H. Dong, D. Sinton, E. Sargent, M. Zhong, Stable, active $CO_2$ reduction to formate via redox-modulated stabilization of active sites, Nat. Commun. 12 (2021) 5223.

[40] I. Chiorescu, J. Arce-Ramos, W.-q. Li, A. Genest, N. Rösch, $CO_2$ reduction by $H_2$ to CHO on Ru(0001): DFT evaluation of three pathways, Surf. Sci. 681 (2019) 54–58.

[41] A. J. Garza, A. T. Bell, M. Head-Gordon, Mechanism of $CO_2$ Reduction at Copper Surfaces: Pathways to C2 Products, ACS Catal. 8 (2) (2018) 1490–1499.

[42] W. Ju, A. Bagger, X. Wang, Y. Tsai, F. Luo, T. Möller, H. Wang, J. Rossmeisl, A. S. Varela, P. Strasser, Unraveling Mechanistic Reaction Pathways of the Electrochemical $CO_2$ Reduction on Fe–N–C Single-Site Catalysts, ACS Energy Lett. 4 (7) (2019) 1663–1671.

[43] M. Neurock, S. A. Wasileski, D. Mei, From first principles to catalytic performance: tracking molecular transformations, Chem. Eng. Sci. 59 (22) (2004) 4703–4714.

[44] M. Garcia-Ratés, R. García-Muelas, N. López, Solvation Effects on Methanol Decomposition on Pd(111), Pt(111), and Ru(0001), J. Phys. Chem. C 121 (25) (2017) 13803–13809.

[45] C. X. Zhao, Y. F. Bu, W. Gao, Q. Jiang, $CO_2$ Reduction Mechanism on the Pb(111) Surface: Effect of Solvent and Cations, J. Phys. Chem. C 121 (36) (2017) 19767–19773.

[46] X. Nie, W. Luo, M. J. Janik, A. Asthagiri, Reaction mechanisms of $CO_2$ electrochemical reduction on Cu(111) determined with density functional theory, J. Catal. 312 (2014) 108–122.

[47] M. Fan, M. J. Eslamibidgoli, X. Zhu, S. Garbarino, A. C. Tavares, M. Eikerling, D. Guay, Understanding the Improved Activity of Dendritic $Sn_1Pb_3$ Alloy for the $CO_2$ Electrochemical Reduction: A Computational–Experimental Investigation, ACS Catal. 10 (18) (2020) 10726–10734.

[48] D. L. Doering, T. E. Madey, The adsorption of water on clean and oxygen-dosed Ru(011), Surf. Sci. 123 (2) (1982) 305 – 337.

[49] S. Schnur, A. Groß, Properties of metal–water interfaces studied from first principles, New J. Phys. 11 (12) (2009) 125003.

[50] X. Lin, A. Groß, First-principles study of the water structure on flat and stepped gold surfaces, Surf. Sci. 606 (11) (2012) 886–891.

[51] Y. Gohda, S. Schnur, A. Groß, Influence of water on elementary reaction steps in electrocatalysis, Faraday Discuss. 140 (2009) 233–244.

[52] S. Nie, P. J. Feibelman, N. C. Bartelt, K. Thürmer, Pentagons and Heptagons in the First Water Layer on Pt(111), Phys. Rev. Lett. 105 (2) (2010) 026102.

[53] P. J. Feibelman, Partial Dissociation of Water on Ru(0001), Science 295 (5552) (2002) 99–102.

[54] S. Sakong, A. Groß, Water structures on a Pt(111) electrode from *ab initio* molecular dynamic simulations for a variety of electrochemical conditions, Phys. Chem. Chem. Phys. 22 (19) (2020) 10431–10437.

[55] O. M. Magnussen, A. Groß, Toward an Atomic-Scale Understanding of Electrochemical Interface Structure and Dynamics, J. Am. Chem. Soc. 141 (12) (2019) 4777–4790.

[56] A. Groß, F. Gossenberger, X. Lin, M. Naderian, S. Sakong, T. Roman, Water Structures at Metal Electrodes Studied by Ab Initio Molecular Dynamics Simulations, J. Electrochem. Soc. 161 (8) (2014) E3015–E3020.

[57] X. Lin, F. Evers, A. Groß, First-principles study of the structure of water layers on flat and stepped Pb electrodes, Beilstein J. Nanotechnol. 7 (2016) 533–543.

[58] M. T. Darby, C. S. Cucinotta, The role of water at electrified metal-water interfaces unravelled from first principles, Curr Opin Electrochem 36 (2022) 101118.

[59] G. Cicero, A. Calzolari, S. Corni, A. Catellani, Anomalous Wetting Layer at the Au(111) Surface, J. Phys. Chem. Lett. 2 (20) (2011) 2582–2586.

[60] T. Ludwig, J. A. Gauthier, K. S. Brown, S. Ringe, J. K. Nørskov, K. Chan, Solvent–Adsorbate Interactions and Adsorbate-Specific Solvent Structure in Carbon Dioxide Reduction on a Stepped Cu Surface, J. Phys. Chem. C 123 (10) (2019) 5999–6009.

[61] K. Vanommeslaeghe, E. Hatcher, C. Acharya, S. Kundu, S. Zhong, J. Shim, E. Darian, O. Guvench, P. Lopes, I. Vorobyov, A. D. MacKerell, CHARMM General Force Field (CGenFF): A force field for drug-like molecules compatible with the CHARMM all-atom additive biological force fields, J Comput Chem 31 (4) (2010) 671–690.

[62] W. D. Cornell, P. Cieplak, C. I. Bayly, I. R. Gould, K. M. Merz, D. M. Ferguson, D. C. Spellmeyer, T. Fox, J. W. Caldwell, P. A. Kollman, A Second Generation Force Field for the Simulation of Proteins, Nucleic Acids, and Organic Molecules, J. Am. Chem. Soc. 117 (19) (1995) 5179–5197.

[63] C. Oostenbrink, A. Villa, A. E. Mark, W. F. Van Gunsteren, A biomolecular force field based on the free enthalpy of hydration and solvation: The GROMOS force-field parameter sets 53A5 and 53A6, J. Am. Chem. Soc. 25 (13) (2004) 1656–1676.

[64] Nobel Prizes 2013 M. Karplus, M. Levitt, A. Warshel, Angew. Chem. Int. Ed. 52 (46) (2013) 11972–11972.

[65] D. Golze, M. Iannuzzi, M.-T. Nguyen, D. Passerone, J. Hutter, Simulation of Adsorption Processes at Metallic Interfaces: An Image Charge Augmented QM/MM Approach, J. Chem. Theory Comput. 9 (11) (2013) 5086–5097.

[66] G. A. Bramley, O. T. Beynon, P. V. Stishenko, A. J. Logsdail, The application of QM/MM simulations in heterogeneous catalysis, Phys. Chem. Chem. Phys. 25 (9) (2023) 6562–6585.

[67] Q. Cui, T. Pal, L. Xie, Biomolecular QM/MM Simulations: What Are Some of the "Burning Issues"?, J. Phys. Chem. B 125 (3) (2021) 689–702.

[68] X. Liao, R. Lu, L. Xia, Q. Liu, H. Wang, K. Zhao, Z. Wang, Y. Zhao, Density Functional Theory for Electrocatalysis, Energy Environ. Mater. 5 (1) (2022) 157–185.

[69] S. A. Hollingsworth, R. O. Dror, Molecular Dynamics Simulation for All, Neuron 99 (6) (2018) 1129–1143.

[70] S. N. Steinmann, R. Ferreira De Morais, A. W. Götz, P. Fleurat-Lessard, M. Iannuzzi, P. Sautet, C. Michel, Force Field for Water over Pt(111): Development, Assessment, and Comparison, J. Chem. Theory Comput. 14 (6) (2018) 3238–3251.

[71] H. Heinz, T.-J. Lin, R. Kishore Mishra, F. S. Emami, Thermodynamically Consistent Force Fields for the Assembly of Inorganic, Organic, and Biological Nanostructures: The INTERFACE Force Field, Langmuir 29 (6) (2013) 1754–1765.

[72] P. Clabaut, B. Schweitzer, A. W. Götz, C. Michel, S. N. Steinmann, Solvation Free Energies and Adsorption Energies at the Metal/Water Interface from Hybrid Quantum-Mechanical/Molecular Mechanics Simulations, J. Chem. Theory Comput. 16 (10) (2020) 6539–6549.

[73] H. H. Heenen, J. A. Gauthier, H. H. Kristoffersen, T. Ludwig, K. Chan, Solvation at metal/water interfaces: An *ab initio* molecular dynamics benchmark of common computational approaches, J. Chem. Phys. 152 (14) (2020) 144703.

[74] Y. Mei, N. A. Deskins, An evaluation of solvent effects and ethanol oxidation, Phys. Chem. Chem. Phys. 23 (30) (2021) 16180–16192.

[75] K. Schwarz, R. Sundararaman, The electrochemical interface in first-principles calculations, Surf. Sci. Rep. 75 (2) (2020) 100492.

112

[76] R. Tesch, P. M. Kowalski, M. H. Eikerling, Properties of the Pt(111)/electrolyte electrochemical interface studied with a hybrid DFT–solvation approach, J. Phys.: Condens. Matter 33 (44) (2021) 444004.

[77] D. Sholl, J. Steckel, Density Functional Theory: A Practical Introduction, Wiley, 2011.

[78] W. Koch, M. C. Holthausen, A Chemist's Guide to Density Functional Theory, Wiley, 1 edn., 2001.

[79] M. Born, R. Oppenheimer, Zur Quantentheorie der Molekeln, Ann Phys 389 (20) (1927) 457–484.

[80] J. C. Slater, A Simplification of the Hartree-Fock Method, Phys. Rev. 81 (3) (1951) 385–390.

[81] W. Pauli, Über den Zusammenhang des Abschlusses der Elektronengruppen im Atom mit der Komplexstruktur der Spektren, Einführ. Orig 229 (1925) 765–783.

[82] P. Hohenberg, W. Kohn, Inhomogeneous Electron Gas, Phys. Rev. 136 (3) (1964) B864–B871.

[83] W. Kohn, L. J. Sham, Self-Consistent Equations Including Exchange and Correlation Effects, Phys. Rev. 140 (4) (1965) A1133–A1138.

[84] J. P. Perdew, A. Ruzsinszky, J. Tao, V. N. Staroverov, G. E. Scuseria, G. I. Csonka, Prescription for the design and selection of density functional approximations: More constraint satisfaction with fewer fits, J. Chem. Phys. 123 (6) (2005) 062201.

[85] J. P. Perdew, K. Burke, M. Ernzerhof, Generalized Gradient Approximation Made Simple, Phys. Rev. Lett. 77 (18) (1996) 3865–3868.

[86] P. J. Stephens, F. J. Devlin, C. F. Chabalowski, M. J. Frisch, Ab Initio Calculation of Vibrational Absorption and Circular Dichroism Spectra Using Density Functional Force Fields, J. Phys. Chem. 98 (45) (1994) 11623–11627.

[87] J. P. Perdew, Y. Wang, Accurate and simple analytic representation of the electron-gas correlation energy, Phys. Rev. B 45 (23) (1992) 13244–13249.

[88] J. Tao, J. P. Perdew, V. N. Staroverov, G. E. Scuseria, Climbing the Density Functional Ladder: Nonempirical Meta–Generalized Gradient Approximation Designed for Molecules and Solids, Phys. Rev. Lett. 91 (14) (2003) 146401.

[89] K. Lee, D. Murray, L. Kong, B. I. Lundqvist, D. C. Langreth, Higher-accuracy van der Waals density functional, Phys. Rev. B 82 (8) (2010) 081101.

[90] D. Rappoport, N. R. M. Crawford, F. Furche, K. Burke, Approximate Density Functionals: Which Should I Choose?, in: Encyclopedia of Inorganic and Bioinorganic Chemistry, John Wiley & Sons, Ltd, 2011.

[91] A. L. Magalhães, Gaussian-Type Orbitals versus Slater-Type Orbitals: A Comparison, J. Chem. Educ. 91 (12) (2014) 2124–2127.

[92] F. Bloch, Über die Quantenmechanik der Elektronen in Kristallgittern, Z. Physik 52 (7) (1929) 555–600.

[93] W. L. Jorgensen, J. Chandrasekhar, J. D. Madura, R. W. Impey, M. L. Klein, Comparison of simple potential functions for simulating liquid water, J. Chem. Phys. 79 (2) (1983) 926–935.

[94] E. Braun, J. Gilmer, H. B. Mayes, D. L. Mobley, J. I. Monroe, S. Prasad, D. M. Zuckerman, Best Practices for Foundations in Molecular Simulations, LiveCoMS 1 (1).

[95] W. L. Jorgensen, J. Tirado-Rives, The OPLS [optimized potentials for liquid simulations] potential functions for proteins, energy minimizations for crystals of cyclic peptides and crambin, J. Am. Chem. Soc. 110 (6) (1988) 1657–1666.

[96] M. González, Force fields and molecular dynamics simulations, JDN 12 (2011) 169–200.

[97] J. P. Ewen, C. Gattinoni, F. M. Thakkar, N. Morgan, H. A. Spikes, D. Dini, A Comparison of Classical Force-Fields for Molecular Dynamics Simulations of Lubricants, Materials (Basel) 9 (8) (2016) 651.

[98] M. P. Allen, D. J. Tildesley, Computer simulation of liquids, Oxford University Press, second edition edn., 2017.

[99] D. J. Evans, B. L. Holian, The Nose–Hoover thermostat, J. Chem. Phys. 83 (1985) 4069.

[100] O. Andreussi, I. Dabo, N. Marzari, Revised self-consistent continuum solvation in electronic-structure calculations, J. Chem. Phys. 136 (6) (2012) 064102.

[101] K. Mathew, R. Sundararaman, K. Letchworth-Weaver, T. A. Arias, R. G. Hennig, Implicit solvation model for density-functional study of nanocrystal surfaces and reaction pathways., J. Chem. Phys. 140 (2014) 084106.

[102] K. Mathew, V. S. C. Kolluru, S. Mula, S. N. Steinmann, R. G. Hennig, Implicit self-consistent electrolyte model in plane-wave density-functional theory., J. Chem. Phys. 151 (2019) 234101.

[103] M. Cossi, V. Barone, R. Cammi, J. Tomasi, Ab initio study of solvated molecules: a new implementation of the polarizable continuum model, Chem. Phys. Lett. 255 (4) (1996) 327–335.

[104] G. Fisicaro, L. Genovese, O. Andreussi, S. Mandal, N. N. Nair, N. Marzari, S. Goedecker, Soft-Sphere Continuum Solvation in Electronic-Structure Calculations, J. Chem. Theory Comput. 13 (8) (2017) 3829–3845.

[105] M. Saleheen, M. Zare, M. Faheem, A. Heyden, Computational Investigation of Aqueous Phase Effects on the Dehydrogenation and Dehydroxylation of Polyols over Pt(111), J. Phys. Chem. C 123 (31) (2019) 19052–19065.

[106] A. Rendón-Calle, S. Builes, F. Calle-Vallejo, Substantial improvement of electrocatalytic predictions by systematic assessment of solvent effects on adsorption energies, Appl. Catal. B 276 (2020) 119147.

[107] O. Björneholm, M. H. Hansen, A. Hodgson, L.-M. Liu, D. T. Limmer, A. Michaelides, P. Pedevilla, J. Rossmeisl, H. Shen, G. Tocci, E. Tyrode, M.-M. Walz, J. Werner, H. Bluhm, Water at Interfaces, Chem. Rev. 116 (13) (2016) 7698–7726.

[108] A. Michaelides, Density functional theory simulations of water–metal interfaces: waltzing waters, a novel 2D ice phase, and more, Appl. Phys. A 85 (4) (2006) 415–425.

[109] M. J. Gillan, D. Alfè, A. Michaelides, Perspective: How good is DFT for water?, J. Chem. Phys. 144 (13) (2016) 130901.

[110] A. C. Dávila López, T. Eggert, K. Reuter, N. G. Hörmann, Static and dynamic water structures at interfaces: A case study with focus on Pt(111), J. Chem. Phys. 155 (19) (2021) 194702.

[111] Q. Zhang, A. Asthagiri, Solvation effects on DFT predictions of ORR activity on metal surfaces, Catal. Today 323 (2019) 35–43.

[112] H. C. Herbol, J. Stevenson, P. Clancy, Computational Implementation of Nudged Elastic Band, Rigid Rotation, and Corresponding Force Optimization, J. Chem. Theory Comput. 13 (7) (2017) 3250–3259.

[113] D. Sheppard, R. Terrell, G. Henkelman, Optimization methods for finding minimum energy paths, J. Chem. Phys 128 (13) (2008) 134106.

[114] G. Henkelman, H. Jónsson, Improved tangent estimate in the nudged elastic band method for finding minimum energy paths and saddle points, J. Chem. Phys 113 (22) (2000) 9978–9985.

[115] Z. Tian, C. Priest, L. Chen, Recent Progress in the Theoretical Investigation of Electrocatalytic Reduction of $CO_2$, Adv. Theory Simul. 1 (5) (2018) 1800004.

[116] I. Ledezma-Yanez, W. D. Z. Wallace, P. Sebastián-Pascual, V. Climent, J. M. Feliu, M. T. M. Koper, Interfacial water reorganization as a pH-dependent descriptor of the hydrogen evolution rate on platinum electrodes 2 (4) (2017) 17031.

[117] A. Berg, C. Peter, K. Johnston, Evaluation and Optimization of Interface Force Fields for Water on Gold Surfaces, J. Chem. Theory Comput. 13 (11) (2017) 5610–5623.

[118] M. Tatarkhanov, D. F. Ogletree, F. Rose, T. Mitsui, E. Fomin, S. Maier, M. Rose, J. I. Cerdá, M. Salmeron, Metal- and Hydrogen-Bonding Competition during Water Adsorption on Pd(111) and Ru(0001), J. Am. Chem. Soc. 131 (51) (2009) 18425–18434.

[119] G. Held, D. Menzel, Isotope effects in structure and kinetics of water adsorbates on Ru(001), Surf. Sci. 327 (3) (1995) 301–320.

[120] F. McBride, A. Omer, C. M. Clay, L. Cummings, G. R. Darling, A. Hodgson, Strain relief and disorder in commensurate water layers formed on Pd(111), J. Phys.: Condens. Matter 24 (12) (2012) 124102.

[121] M. Naderian, A. Groß, From single molecules to water networks: Dynamics of water adsorption on Pt(111), J. Chem. Phys. (2016) 8.

[122] A. Groß, Theory of Solid/Electrolyte Interfaces, Surface and Interface Science, WILEY-VCH Verlag GmbH & Co., 471–515, 2020.

[123] J. Carrasco, A. Hodgson, A. Michaelides, A molecular perspective of water at metal interfaces, Nat. Mater. 11 (8) (2012) 667–674.

[124] C. Peter, K. Kremer, Multiscale simulation of soft matter systems – from the atomistic to the coarse-grained level and back, Soft Matter 5 (22) (2009) 4357.

[125] S. Nishihara, M. Otani, Hybrid solvation models for bulk, interface, and membrane: Reference interaction site methods coupled with density functional theory, Phys. Rev. B 96 (2017) 115429.

[126] J. Huang, S. Chen, M. Eikerling, Grand-Canonical Model of Electrochemical Double Layers from a Hybrid Density–Potential Functional, J. Chem. Theory Comput. 17 (4) (2021) 2417–2430.

[127] C. H. Lee, M. W. Kanan, Controlling $H^+$ vs $CO_2$ Reduction Selectivity on Pb Electrodes, ACS Catal. 5 (1) (2015) 465–469.

[128] S. Y. Choi, S. K. Jeong, H. J. Kim, I.-H. Baek, K. T. Park, Electrochemical Reduction of Carbon Dioxide to Formate on Tin–Lead Alloys, ACS Sustainable Chem. Eng. 4 (3) (2016) 1311–1318.

[129] C. Cui, H. Wang, X. Zhu, J. Han, Q. Ge, A DFT study of $CO_2$ electrochemical reduction on Pb(211) and Sn(112), Sci. China Chem. 58 (4) (2015) 607–613.

[130] A. K. Singh, S. Singh, A. Kumar, Hydrogen energy future with formic acid: a renewable chemical hydrogen storage system, Catal. Sci. Technol. 6 (1) (2016) 12–40.

[131] J. Klankermayer, S. Wesselbaum, K. Beydoun, W. Leitner, Selective Catalytic Synthesis Using the Combination of Carbon Dioxide and Hydrogen: Catalytic Chess at the Interface of Energy and Chemistry, Angew. Chem. Int. Ed. 55 (26) (2016) 7296–7343.

[132] J. Hietala, A. Vuori, P. Johnsson, I. Pollari, W. Reutemann, H. Kieczka, Formic Acid, in: Wiley-VCH Verlag GmbH & Co. KGaA (Ed.), Ullmann's Encyclopedia of Industrial Chemistry, Wiley-VCH Verlag GmbH & Co. KGaA, 1–22, 2016.

[133] S. Plimpton, Fast Parallel Algorithms for Short-Range Molecular Dynamics, J. Comput. Phys. 117 (1) (1995) 1 – 19.

[134] H. J. C. Berendsen, J. R. Grigera, T. P. Straatsma, The missing term in effective pair potentials, J. Phys. Chem. 91 (24) (1987) 6269–6271.

[135] L. Martínez, R. Andrade, E. G. Birgin, J. M. Martínez, PACKMOL: A package for building initial configurations for molecular dynamics simulations, J. Comput. Chem. 30 (13) (2009) 2157–2164.

[136] P. Giannozzi, S. Baroni, N. Bonini, M. Calandra, R. Car, C. Cavazzoni, D. Ceresoli, G. L. Chiarotti, M. Cococcioni, I. Dabo, A. D. Corso, S. de Gironcoli, S. Fabris, G. Fratesi, R. Gebauer, U. Gerstmann, C. Gougoussis, A. Kokalj, M. Lazzeri, L. Martin-Samos, N. Marzari, F. Mauri, R. Mazzarello, S. Paolini, A. Pasquarello, L. Paulatto, C. Sbraccia, S. Scandolo, G. Sclauzero, A. P. Seitsonen, A. Smogunov, P. Umari, R. M. Wentzcovitch, QUANTUM ESPRESSO: a modular and open-source software project for quantum simulations of materials, J. Phys.: Condens. Matter 21 (39) (2009) 395502.

[137] J. P. Perdew, K. Burke, M. Ernzerhof, Generalized Gradient Approximation Made Simple, Phys. Rev. Lett. 77 (1996) 3865–3868.

[138] P. E. Blöchl, Projector augmented-wave method, Phys. Rev. B 50 (24) (1994) 17953–17979.

[139] A. Hjorth Larsen, J. Jørgen Mortensen, J. Blomqvist, I. E. Castelli, R. Christensen, M. Dułak, J. Friis, M. N. Groves, B. Hammer, C. Hargus, E. D. Hermes,

P. C. Jennings, P. Bjerre Jensen, J. Kermode, J. R. Kitchin, E. Leonhard Kols-bjerg, J. Kubal, K. Kaasbjerg, S. Lysgaard, J. Bergmann Maronsson, T. Max-son, T. Olsen, L. Pastewka, A. Peterson, C. Rostgaard, J. Schiøtz, O. Schütt, M. Strange, K. S. Thygesen, T. Vegge, L. Vilhelmsen, M. Walter, Z. Zeng, K. W. Jacobsen, The atomic simulation environment—a Python library for working with atoms, J. Phys.: Condens. Matter 29 (27) (2017) 273002.

[140] H. J. Monkhorst, J. D. Pack, Special points for Brillouin-zone integrations, Phys. Rev. B 13 (12) (1976) 5188–5192.

[141] J. P. Perdew, A. Ruzsinszky, G. I. Csonka, O. A. Vydrov, G. E. Scuseria, L. A. Constantin, X. Zhou, K. Burke, Restoring the Density-Gradient Expansion for Exchange in Solids and Surfaces, Phys. Rev. Lett. 100 (13) (2008) 136406.

[142] J. H. Park, N. R. Aluru, Diffusion of water submonolayers on hydrophilic sur-faces, Appl. Phys. Lett. 93 (25) (2008) 253104.

[143] J. Matt, spatialgraph2D (https://www.mathworks.com/matlabcentral/fileexchange/ 73630-spatialgraph2d), MATLAB Central File Exchange .

[144] P. J. Feibelman, Using Ar adsorption to estimate the van der Waals contribution to the wetting of Ru(0001), Phys. Rev. B: Condens. Matter Mater. Phys. (2005) 3.

[145] I. L. Geada, H. Ramezani-Dakhel, T. Jamil, M. Sulpizi, H. Heinz, Insight into induced charges at metal surfaces and biointerfaces using a polarizable Lennard–Jones potential, Nat. Commun. (2018) 14.

[146] S. N. Steinmann, P. Sautet, C. Michel, Solvation free energies for periodic sur-faces: comparison of implicit and explicit solvation models, Phys. Chem. Chem. Phys. 18 (46) (2016) 31850–31861.

[147] F. Calle-Vallejo, R. F. de Morais, F. Illas, D. Loffreda, P. Sautet, Affordable Es-timation of Solvation Contributions to the Adsorption Energies of Oxygenates on Metal Nanoparticles 123 (9) (2019) 5578–5582.

[148] S. K. Iyemperumal, N. A. Deskins, Evaluating Solvent Effects at the Aque-ous/Pt(111) Interface, ChemPhysChem 18 (16) (2017) 2171–2190.

[149] A. Bagger, L. Arnarson, M. H. Hansen, E. Spohr, J. Rossmeisl, Electrochemical CO Reduction: A Property of the Electrochemical Interface, J. Am. Chem. Soc. 141 (4) (2019) 1506–1514.

[150] M. Valter, B. Wickman, A. Hellman, Solvent Effects for Methanol Electrooxidation on Gold, J. Phys. Chem. C 125 (2) (2021) 1355–1360.

[151] M. Zare, M. Saleheen, S. K. Kundu, A. Heyden, Dependency of solvation effects on metal identity in surface reactions, Commun Chem 3 (1) (2020) 187.

[152] J. Santatiwongchai, K. Faungnawakij, P. Hirunsit, Comprehensive Mechanism of $CO_2$ Electroreduction toward Ethylene and Ethanol: The Solvent Effect from Explicit Water–Cu(100) Interface Models, ACS Catal. 11 (15) (2021) 9688–9701.

[153] O. Cheong, M. H. Eikerling, P. M. Kowalski, Water structures on Pb(100) and (111) surface studied with the Interface force field, Appl. Surf. Sci. 589 (2022) 152838.

[154] H. Papp, M. Baerns, Chapter 10 Industrial Application of Co Chemistry for The Production of Specialty Chemicals, in: L. Guczi (Ed.), New Trends in Coactivation, vol. 64 of *Studies in Surface Science and Catalysis*, Elsevier, 430–461, 1991.

[155] N. J. Firet, W. A. Smith, Probing the Reaction Mechanism of $CO_2$ Electroreduction over Ag Films via Operando Infrared Spectroscopy, ACS Catal. 7 (1) (2017) 606–612.

[156] J. Hussain, H. Jónsson, E. Skúlason, Calculations of Product Selectivity in Electrochemical $CO_2$ Reduction, ACS Catal. 8 (6) (2018) 5240–5249.

[157] A. R. T. Morrison, M. Ramdin, L. J. P. van der Broeke, W. de Jong, T. J. H. Vlugt, R. Kortlever, Surface Coverage as an Important Parameter for Predicting Selectivity Trends in Electrochemical $CO_2$ Reduction, J. Phys. Chem. C 126 (29) (2022) 11927–11936.

[158] D. Bohra, I. Ledezma-Yanez, G. Li, W. deJong, E. A. Pidko, W. A. Smith, Lateral Adsorbate Interactions Inhibit HCOO while Promoting CO Selectivity

for $CO_2$ Electrocatalysis on Silver, Angew. Chem. Int. Ed. 58 (5) (2019) 1345–1349.

[159] X.-G. Zhang, X. Jin, D.-Y. Wu, Z.-Q. Tian, Selective Electrocatalytic Mechanism of $CO_2$ Reduction Reaction to CO on Silver Electrodes: A Unique Reaction Intermediate, J. Phys. Chem. C 122 (44) (2018) 25447–25455.

[160] A. Seifitokaldani, C. M. Gabardo, T. Burdyny, C.-T. Dinh, J. P. Edwards, M. G. Kibria, O. S. Bushuyev, S. O. Kelley, D. Sinton, E. H. Sargent, Hydronium-Induced Switching between $CO_2$ Electroreduction Pathways, J. Am. Chem. Soc. 140 (11) (2018) 3833–3837.

[161] I. Shyjumon, M. Gopinadhan, O. Ivanova, M. Quaas, H. Wulff, C. A. Helm, R. Hippler, Structural deformation, melting point and lattice parameter studies of size selected silver clusters, Eur. Phys. J. D 37 (3) (2006) 409–415.

[162] P. Giannozzi, O. Andreussi, T. Brumme, O. Bunau, M. B. Nardelli, M. Calandra, R. Car, C. Cavazzoni, D. Ceresoli, M. Cococcioni, N. Colonna, I. Carnimeo, A. D. Corso, S. d. Gironcoli, P. Delugas, R. A. DiStasio, A. Ferretti, A. Floris, G. Fratesi, G. Fugallo, R. Gebauer, U. Gerstmann, F. Giustino, T. Gorni, J. Jia, M. Kawamura, H.-Y. Ko, A. Kokalj, E. Küçükbenli, M. Lazzeri, M. Marsili, N. Marzari, F. Mauri, N. L. Nguyen, H.-V. Nguyen, A. Otero-de-la Roza, L. Paulatto, S. Poncé, D. Rocca, R. Sabatini, B. Santra, M. Schlipf, A. P. Seitsonen, A. Smogunov, I. Timrov, T. Thonhauser, P. Umari, N. Vast, X. Wu, S. Baroni, Advanced capabilities for materials modelling with Quantum ESPRESSO, J. Phys.: Condens. Matter 29 (46) (2017) 465901, publisher: IOP Publishing.

[163] S. Grimme, J. Antony, S. Ehrlich, H. Krieg, A consistent and accurate *ab initio* parametrization of density functional dispersion correction (DFT-D) for the 94 elements H-Pu, J. Chem. Phys. 132 (15) (2010) 154104.

[164] J. VandeVondele, F. Mohamed, M. Krack, J. Hutter, M. Sprik, M. Parrinello, The influence of temperature and density functional models in *ab initio* molecular dynamics simulation of liquid water, J. Chem. Phys. 122 (1) (2005) 014515.

[165] J. Carrasco, J. Klimeš, A. Michaelides, The role of van der Waals forces in water adsorption on metals, J. Chem. Phys. 138 (2) (2013) 024708.

[166] H. Chen, M. A. Blatnik, C. L. Ritterhoff, I. Sokolović, F. Mirabella, G. Franceschi, M. Riva, M. Schmid, J. Čechal, B. Meyer, U. Diebold, M. Wagner, Water Structures Reveal Local Hydrophobicity on the In$_2$O$_3$ (111) Surface, ACS Nano 16 (12) (2022) 21163–21173.

[167] E. Romeo, F. Illas, F. Calle-Vallejo, Evaluating Adsorbate–Solvent Interactions: Are Dispersion Corrections Necessary?, J. Phys. Chem. C 127 (21) (2023) 10134–10139.

[168] A. A. Peterson, Global Optimization of Adsorbate–Surface Structures While Preserving Molecular Identity, Top Catal 57 (1) (2014) 40–53.

[169] G. Henkelman, B. Uberuaga, H. Jonsson, A Climbing Image Nudged Elastic Band Method for Finding Saddle Points and Minimum Energy Paths, J. Chem. Phys. 113 (2000) 9901–9904.

[170] P. M. Kowalski, T. Bornhake, O. Cheong, N. Dohrmann, A. L. Koch Liston, S. K. Potts, A. Shad, R. Tesch, Y.-Y. Ting, Fundamentals of energy storage from first principles simulations: Challenges and opportunities, Front. Energy Res. 10 (2023) 1096190.

[171] G. Kresse, J. Hafner, *Ab initio* molecular dynamics for liquid metals, Phys. Rev. B 47 (1) (1993) 558–561.

[172] G. Kresse, J. Furthmüller, Efficiency of ab-initio total energy calculations for metals and semiconductors using a plane-wave basis set, Comput. Mater. Sci. 6 (1) (1996) 15–50.

[173] G. Kresse, J. Furthmüller, Efficient iterative schemes for *ab initio* total-energy calculations using a plane-wave basis set, Phys. Rev. B 54 (16) (1996) 11169–11186.

[174] X. Lin, A. Shao, M. Hua, X. Tian, A first-principles study of water adsorbed on flat and stepped silver surfaces, Phys. Chem. Chem. Phys. 24 (11) (2022) 6803–6810.

[175] M. Van den Bossche, C. Rose-Petruck, H. Jónsson, Competing HCOOH and CO Pathways in CO$_2$ Electroreduction at Copper Electrodes: Calculations of

Voltage-Dependent Activation Energy, J. Phys. Chem. C 125 (25) (2021) 13802–13808.

[176] J. A. Gauthier, M. Fields, M. Bajdich, L. D. Chen, R. B. Sandberg, K. Chan, J. K. Nørskov, Facile Electron Transfer to $CO_2$ during Adsorption at the Metal|Solution Interface, J. Phys. Chem. C 123 (48) (2019) 29278–29283.

[177] H. Noda, S. Ikeda, Y. Oda, K. Imai, M. Maeda, K. Ito, Electrochemical Reduction of Carbon Dioxide at Various Metal Electrodes in Aqueous Potassium Hydrogen Carbonate Solution, BCSJ 63 (9) (1990) 2459–2462.

[178] T. Hatsukade, K. P. Kuhl, E. R. Cave, D. N. Abram, T. F. Jaramillo, Insights into the electrocatalytic reduction of $CO_2$ on metallic silver surfaces, Phys. Chem. Chem. Phys. 16 (27) (2014) 13814–13819.

[179] X. Zhu, J. Huang, M. Eikerling, Electrochemical $CO_2$ Reduction at Silver from a Local Perspective, ACS Catal. 11 (23) (2021) 14521–14532.

[180] J. Huang, X. Zhu, M. Eikerling, The rate-determining term of electrocatalytic reactions with first-order kinetics, Electrochim. Acta 393 (2021) 139019.

[181] X. Zhu, J. Huang, M. Eikerling, pH Effects in a Model Electrocatalytic Reaction Disentangled, JACS Au 3 (4) (2023) 1052–1064.

[182] X. Zhang, R. S. DeFever, S. Sarupria, R. B. Getman, Free Energies of Catalytic Species Adsorbed to Pt(111) Surfaces under Liquid Solvent Calculated Using Classical and Quantum Approaches, J. Chem. Inf. Model. 59 (5) (2019) 2190–2198.

[183] A. Klinkova, P. De Luna, C.-T. Dinh, O. Voznyy, E. M. Larin, E. Kumacheva, E. H. Sargent, Rational Design of Efficient Palladium Catalysts for Electroreduction of Carbon Dioxide to Formate, ACS Catal. 6 (12) (2016) 8115–8120.

[184] P. Hirunsit, Electroreduction of Carbon Dioxide to Methane on Copper, Copper–Silver, and Copper–Gold Catalysts: A DFT Study, J. Phys. Chem. C 117 (16) (2013) 8262–8268.

[185] A. A. Peterson, F. Abild-Pedersen, F. Studt, J. Rossmeisl, J. K. Nørskov, How copper catalyzes the electroreduction of carbon dioxide into hydrocarbon fuels, Energy Environ. Sci. 3 (9) (2010) 1311.

[186] K. Chang, X. Jian, H. M. Jeong, Y. Kwon, Q. Lu, M.-J. Cheng, Improving $CO_2$ Electrochemical Reduction to CO Using Space Confinement between Gold or Silver Nanoparticles, J. Phys. Chem. Lett. 11 (5) (2020) 1896–1902.

[187] W. Ma, S. Xie, X.-G. Zhang, F. Sun, J. Kang, Z. Jiang, Q. Zhang, D.-Y. Wu, Y. Wang, Promoting electrocatalytic $CO_2$ reduction to formate via sulfur-boosting water activation on indium surfaces, Nat. Commun. 10 (1) (2019) 892.

[188] A. J. Garza, Solvation Entropy Made Simple, J. Chem. Theory Comput. 15 (5) (2019) 3204–3214.

[189] O. J. Conquest, T. Roman, A. Marianov, A. Kochubei, Y. Jiang, C. Stampfl, Calculating Entropies of Large Molecules in Aqueous Phase, J. Chem. Theory Comput. 17 (12) (2021) 7753–7771.

[190] C. Peter, C. Oostenbrink, A. van Dorp, W. F. van Gunsteren, Estimating entropies from molecular dynamics simulations, J. Chem. Phys. 120 (6) (2004) 2652–2661.

[191] J. G. Kirkwood, Statistical Mechanics of Fluid Mixtures, J. Chem. Phys. 3 (5) (1935) 300–313.

[192] S.-T. Lin, P. K. Maiti, W. A. Goddard, Two-Phase Thermodynamic Model for Efficient and Accurate Absolute Entropy of Water from Molecular Dynamics Simulations, J. Phys. Chem. B 114 (24) (2010) 8191–8198.

[193] S.-T. Lin, M. Blanco, W. A. Goddard, The two-phase model for calculating thermodynamic properties of liquids from molecular dynamics: Validation for the phase diagram of Lennard-Jones fluids, J. Chem. Phys. 119 (22) (2003) 11792–11805.

[194] T. A. Pascal, S.-T. Lin, W. A. Goddard III, Thermodynamics of liquids: standard molar entropies and heat capacities of common solvents from 2PT molecular dynamics, Phys. Chem. Chem. Phys. 13 (1) (2011) 169–181.

[195] C. L. Freeman, J. H. Harding, Entropy of Molecular Binding at Solvated Mineral Surfaces, J. Phys. Chem. C 118 (3) (2014) 1506–1514.

[196] N. Homeyer, H. Gohlke, Free Energy Calculations by the Molecular Mechanics Poisson-Boltzmann Surface Area Method, Mol Inform 31 (2) (2012) 114–122.

[197] R. Réocreux, C. Michel, P. Fleurat-Lessard, P. Sautet, S. N. Steinmann, Evaluating Thermal Corrections for Adsorption Processes at the Metal/Gas Interface, J. Phys. Chem. C 123 (47) (2019) 28828–28835.

[198] C. K. Jung, L. Braunwarth, A. Sinyavskiy, T. Jacob, Thermodynamic Description of Interfaces Applying the 2PT Method on ReaxFF Molecular Dynamics Simulations, J. Phys. Chem. C 125 (44) (2021) 24663–24670.

[199] B. N. Wanjala, J. Luo, B. Fang, D. Mott, C.-J. Zhong, Gold-platinum nanoparticles: alloying and phase segregation, J. Mater. Chem. 21 (12) (2011) 4012–4020.

[200] P. Haas, F. Tran, P. Blaha, Calculation of the lattice constant of solids with semilocal functionals, Phys. Rev. B 79 (8) (2009) 085104.

[201] T. A. Pascal, D. Schärf, Y. Jung, T. D. Kühne, On the absolute thermodynamics of water from computer simulations: A comparison of first-principles molecular dynamics, reactive and empirical force fields, J. Chem. Phys. 137 (24) (2012) 244507.

[202] P. Linstrom, W. Mallard, NIST Chemistry WebBook, NIST Standard Reference Database Number 69 .

[203] R. A. X. Persson, V. Pattni, A. Singh, S. M. Kast, M. Heyden, Signatures of Solvation Thermodynamics in Spectra of Intermolecular Vibrations, J. Chem. Theory Comput. 13 (9) (2017) 4467–4481.

[204] K. Kholmurodov, E. Dushanov, K. Yasuoka, H. Khalil, A. Galal, S. Ahmed, N. Sweilam, H. Moharram, Molecular dynamics study of ethanol solvated by water on the Pt (111) surface, Chem. Phys. 402 (2012) 41–47.

[205] P. Mark, L. Nilsson, Structure and Dynamics of the TIP3P, SPC, and SPC/E Water Models at 298 K, J. Phys. Chem. A 105 (43) (2001) 9954–9960.

[206] J. Wang, R. M. Wolf, J. W. Caldwell, P. A. Kollman, D. A. Case, Development and testing of a general amber force field, J Comput Chem. 25 (9) (2004) 1157–1174.

[207] W. L. Jorgensen, J. D. Madura, C. J. Swenson, Optimized intermolecular potential functions for liquid hydrocarbons, J. Am. Chem. Soc. 106 (22) (1984) 6638–6646.

[208] B. Chen, J. J. Potoff, J. I. Siepmann, Monte Carlo Calculations for Alcohols and Their Mixtures with Alkanes. Transferable Potentials for Phase Equilibria. 5. United-Atom Description of Primary, Secondary, and Tertiary Alcohols, J. Phys. Chem. B 105 (15) (2001) 3093–3104.

[209] E. A. Ploetz, P. E. Smith, A Kirkwood-Buff Force Field for the Aromatic Amino Acids, Phys. Chem. Chem. Phys. 13 (40) (2011) 18154–18167.

# Appendix A

# Supporting Information for Chapter 3
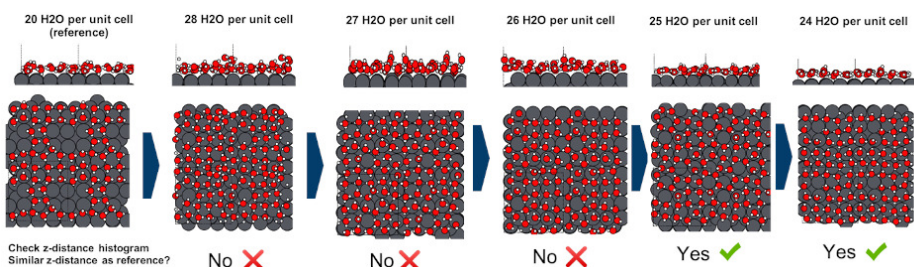


Figure A.1: *Illustration of the procedure of filling up the water cavity. From the water cavity configuration, we add water molecules to the cavity until the Pb-water distance exceeds the Pb-water distance of the reference water cavity structure. In this case for the 4x4 Pb(100) surface 25 water molecules are sufficient to fill up the first layer.*

# Appendix B

# Supporting Information for Chapter 4

(a)

| Molecule | ZPE | TS |
|:---:|:---:|:---:|
| $H_2O$ | 0.56 | 0.67 |
| $CO_2$ | 0.31 | 0.66 |
| $H_2$ | 0.27 | 0.43 |
| CO | 0.13 | 0.67 |
| HCOOH | 0.89 | 1.05 |

(b)

| Ag(100) surface | ZPE | TS |
|:---:|:---:|:---:|
| COOH* | 0.58 | 0.29 |
| HCOO* | 0.60 | 0.24 |
| CO* | 0.17 | 0.21 |
| HCOOH* | 0.90 | 0.31 |

(c)

| Pb(100) surface | ZPE | TS |
|:---:|:---:|:---:|
| COOH* | 0.58 | 0.27 |
| HCOO* | 0.61 | 0.17 |
| CO* | 0.16 | 0.21 |
| HCOOH* | 0.91 | 0.29 |

*Figure B.1: Zero-point energy (ZPE) and entropy (TS) correction terms for (a) different gas phase molecules and adsorbates at (b) Ag(100) surface and (c) Pb(100) surface given in eV. Gas phase correction values are taken from ref[184].*

(a) **HCOO\***

**0.20 eV stabilization**

(b) **COOH\***

**0.19 eV stabilization**
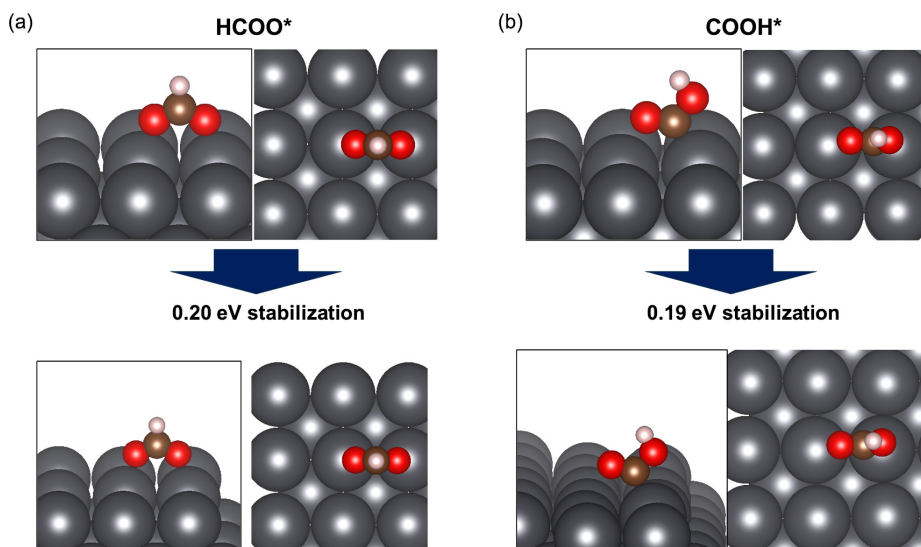
Figure B.2: Illustration of configurational change from vacuum to implicit solvation for (a) HCOO* adsorbate and (b) COOH* adsorbate. As discussed in Chapter 4.3.1, both configuration in implicit solvation do not change significantly compared to the vacuum case configurations.



$HCOO + 8H_2O$

$E_{ads,HCOO} = -1.11$ eV

$HCOO + 9H_2O$

$E_{ads,HCOO} = -1.42$ eV
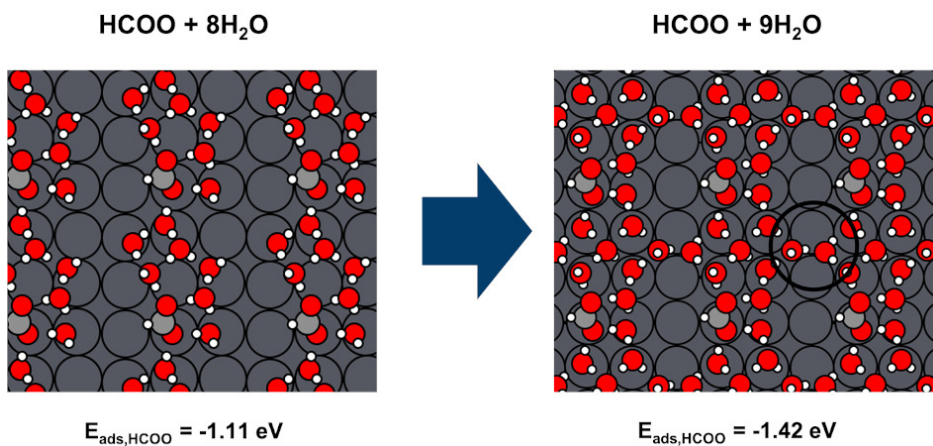
Figure B.3: HCOO adsorbate in the presence of eight and nine explicit water molecules. Adsorption energy $(E_{ads,HCOO})$ increases from eight to nine water molecules due to additional H-bonding caused by periodic boundary conditions.
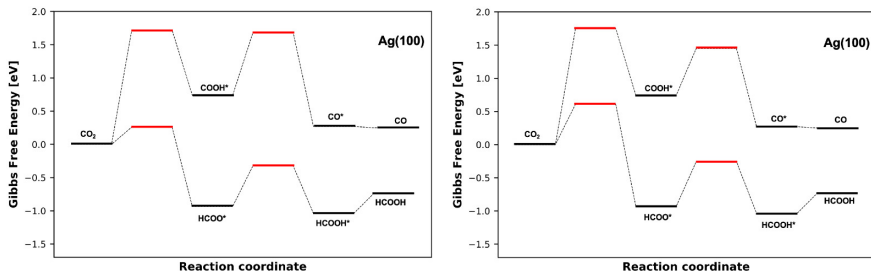
*Figure B.4: Free energy diagram for CO₂ reduction towards CO and HCOOH via HCOO\**
*and COOH\* reaction intermediate under implicit solvation environment on Ag(100) surface*
*using a) single point (SP) calculation method and b) nudged elastic band (NEB) method to*
*calculate the activation energies (indicated in red).*

As shown in Figure B.4, we have compared two different implicit solvation methods to calculate the reaction pathway on the Ag(100) surface. The implicit nudged elastic band (NEB) method performs a series of energy minimizations along the reaction pathway under implicit solvation, while the implicit single point (SP) method uses the same reaction pathway as the vacuum case. During the implicit SP method, implicit single point calculations are applied to the vacuum reaction pathway to calculate the activation barriers under implicit solvation. The SP method is computationally more efficient since only single point calculations are performed. Our results in Figure B.4 show similar reaction energy trends among these methods. Regardless of the implicit solvation method used, the HCOO* pathway is favored over the COOH* pathway, leading to HCOOH formation on Ag(100). In both cases, microkinetic modeling results in selectivities of $s_{CO} \approx 0$ and $s_{HCOOH} \approx 1$ on the Ag(100) surface, confirming the previous findings observed in the vacuum case.

During implicit NEB method calculations, we encountered some convergence difficulties. To bypass this, we increased the $\alpha$ parameter from 1.18 up to 1.9. The $\alpha$ parameter in the Environ package corresponds to the homogeneous scaling factor of the solvent radii. Increasing the $\alpha$ parameter creates a bigger distance between solute cavity and implicit solvation. For implicit SP calculations, we experienced no convergence issues even for $\alpha$ values of 1.18.
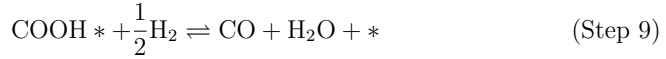
In order to validate the findings obtained from our implicit solvation calculations on the Ag(100) surface, we have performed similar implicit NEB calculations using

the VASPsol package [101, 102]. As shown in Figure B.5, the HCOO* activation energy is significantly lower than the COOH* activation energy, favoring the HCOO* pathway over the COOH* pathway. Also here, HCOOH formation is favored over CO, supporting the aforementioned observations. Quantitative differences between VASPsol and Environ arise due to variations in the dielectric functions utilized to describe the implicit solvation environment. Despite these differences, here the microkinetic modeling also demonstrates selectivities of $s_{CO} \approx 0$ and $s_{HCOOH} \approx 1$ on the Ag(100) surface, indicating that CO cannot be predicted as the primary product on the Ag(100) surface, regardless of the implicit solvation method used.
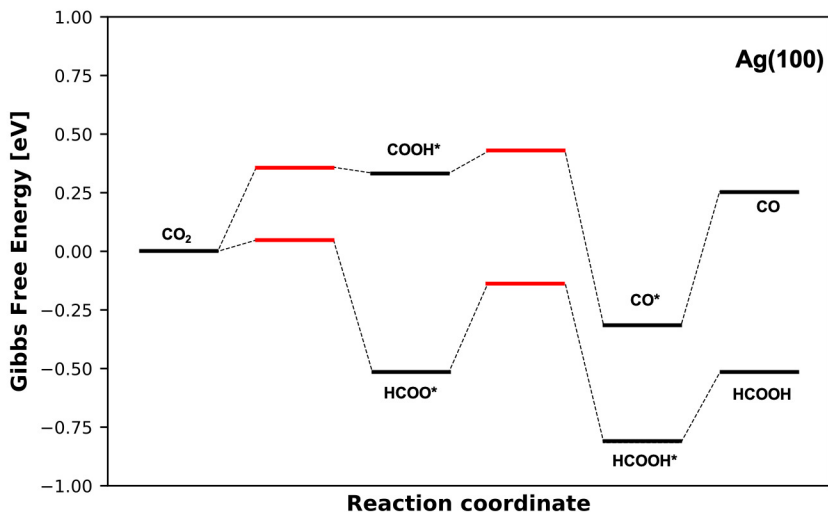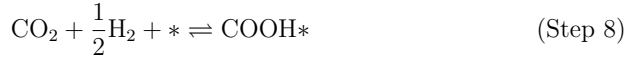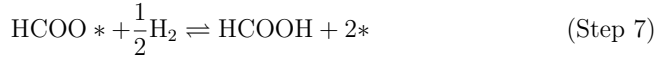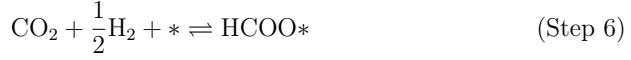


Figure B.5: *Free energy diagram for $CO_2$ reduction towards CO and HCOOH via HCOO\* and COOH\* reaction intermediate under implicit solvation environment on Ag(100) surface using VASPsol.*

# Microkinetic Modeling

When taking into account explicit solvation effects, we examine the following mechanism for the microkinetic model:

$$\text{CO}_2 + * \rightleftharpoons \text{CO}_2* \qquad \text{(Step 5)}$$

$$\text{CO}_2 + \frac{1}{2}\text{H}_2 + * \rightleftharpoons \text{HCOO}* \qquad \text{(Step 6)}$$

$$\text{HCOO} * + \frac{1}{2}\text{H}_2 \rightleftharpoons \text{HCOOH} + 2* \qquad \text{(Step 7)}$$

$$\text{CO}_2 + \frac{1}{2}\text{H}_2 + * \rightleftharpoons \text{COOH}* \qquad \text{(Step 8)}$$

$$\text{COOH} * + \frac{1}{2}\text{H}_2 \rightleftharpoons \text{CO} + \text{H}_2\text{O} + * \qquad \text{(Step 9)}$$

In the same logic as in the vacuum case (Section 4.3.2), we solve the rate equations at steady state

$$\frac{d\theta_{\text{CO}_2*}}{dt} = \nu_5 - \nu_6 - \nu_8 = 0 \qquad (10)$$

$$\frac{d\theta_{\text{HCOO}*}}{dt} = \nu_6 - \nu_7 = 0 \qquad (11)$$

$$\frac{d\theta_{\text{COOH}*}}{dt} = \nu_8 - \nu_9 = 0 \qquad (12)$$

For $\nu_i$, we have the following relations

$$\nu_5 = k_5 c_{\text{CO}_2}\theta_0 - k_{-5}\theta_{\text{CO}_2*} \qquad (13)$$

$$\nu_6 = k_6 \theta_{\text{CO}_2*} c_{\text{H}^+}\theta_0 - k_{-6}\theta_{\text{HCOO}*} \qquad (14)$$

$$\nu_7 = k_7 \theta_{\text{HCOO}*} c_{\text{H}^+} \qquad (15)$$

$$\nu_8 = k_8 \theta_{\text{CO}_2*} c_{\text{H}^+} - k_{-8} \theta_{\text{COOH}*} \tag{16}$$

$$\nu_9 = k_9 \theta_{\text{COOH}*} c_{\text{H}^+} \tag{17}$$

with $c_{\text{CO}_2} = 0.034$ M and $c_{\text{H}^+} = 1$ M , corresponding to $p_{\text{CO}_2} = 1$ atm and pH $= 0$. The selectivities of CO and HCOOH are given by

$$s_{CO} = \frac{\nu_9}{\nu_7 + \nu_9} \tag{18}$$

$$s_{HCOOH} = \frac{\nu_7}{\nu_7 + \nu_9} \tag{19}$$

Given the activation barriers in Figure 4.6, we obtain $s_{CO} \approx 1$ and $s_{HCOOH} \approx 0$ for Ag(100) and $s_{CO} \approx 0$ and $s_{HCOOH} \approx 1$ for Pb(100).

# Appendix C

# Supporting Information for Chapter 5
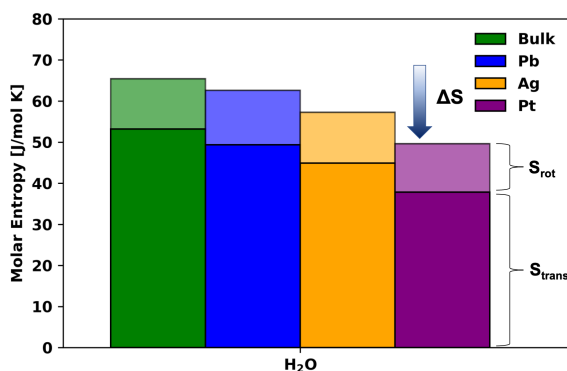


*Figure C.1: Molar entropies of water in bulk and at different metal surfaces (Pt, Ag, Pb) using the 2PT method including translational $S_{trans}$ and rotational $S_{rot}$ entropic contribution. Vibrational entropic contribution $S_{vib}$ is not accounted for as rigid water model is used during MD simulation.*

While the water bulk entropy value of 65.45 J/mol K is in good agreement with experimental data (69.95 J/mol K), we observe entropy reduction of water at all three metal surfaces. At Pb, Ag and Pt surface we obtain water molar entropies of 62.61 J/mol K, 57.25 J/mol K and 49.62 J/mol K, respectively. Most of the entropic

reduction is attributed to the translational entropic reduction when going from bulk to the metal surface environment, as illustrated in Figure S1. This phenomenon is the consequence of reduced solute cavity when moving from the bulk to the metal surface, decreasing the space in which the solute can reside and the translational entropy term.

# Arrhenius equation

The Arrhenius equation describes the reaction rate constant k as the following

$$k = A * \exp\left(\frac{-E_a}{RT}\right) \tag{1}$$

where $A$, $E_a$, $R$ and $T$ represent the pre-exponential factor, the activation energy of the reaction, the gas constant (8.314 J/mol K) and the temperature in K. Assuming that a Brønsted-Evans-Polanyi (BEP) relation between the Gibbs free energy of a reaction, $G$, and the activation energy, $E_a$, exists, the Gibbs free energy of a reaction can be used to calculate the reaction rate constant, $k$.

# Appendix

# List of Publications

1. **O. Cheong**, F. Tipp, M. H. Eikerling, P. M. Kowalski, "Entropy effects on reactive processes at metal-solvent interfaces", accepted in J. Phys. Chem. C (2024).

2. **O. Cheong**, J. Pasel, J. Häusler, R. Peters, M. H. Eikerling, P. M. Kowalski, "Rationalizing the Mechanism of Ethanol Dehydrogenation on Pt/C", Surf. Sci., 739, 122396 (2023).

3. **O. Cheong**, T. Bornhake, X. Zhu, M. H. Eikerling, "Stay hydrated! Impact of solvation phenomena on the $CO_2$ reduction reaction at Pb(100) and Ag(100) surfaces", ChemSusChem, e202300885 (2023).

4. P. M. Kowalski, T. Bornhake, **O. Cheong**, N. Dohrmann, A. Liston, S. Potts, A. Shad, R. Tesch, Y. Ting, "Fundamentals of energy storage from first principles simulations: Challenges and opportunities", Front. Energy Res. 10, 1096190 (2023).

5. **O. Cheong**, M. H. Eikerling, P. M. Kowalski, "Water structures on Pb(100) and (111) surface studied with the Interface force field", Appl. Surf. Sci. 589, 152838 (2022).

6. T. Connor, **O. Cheong**, T. Bornhake, A. C. Shad, R. Tesch, M. Sun, Z. He, A. Bukayemsky, V. Vinograd, S. C. Finkeldei, P. M. Kowalski, "Pyrochlore Compounds From Atomistic Simulations", Front. Chem. 9, 733321 (2021).

7. P. M. Kowalski, Z. He, **O. Cheong**, "Electrode and Electrolyte Materials From Atomistic Simulations: Properties of LixFEPO4 Electrode and Zircon-Based Ionic Conductors", Front. Energy Res. 9, 653542 (2021).

# Appendix

# Conference Contributions

**Talks**

1. 2022 MRS Fall Meeting & Exhibit, 11/2022, Boston, USA, "Effect of solvent on chemistry at the electrochemical interface"

2. 2022 EMRS Fall Meeting, 09/2022, Warsaw, Poland, "Strengths and Limitations of Using the Interface Force Field (IFF) to Assess Water Structures at Metal Surfaces"

3. HITEC Symposium, 06/2022, Jülich, Germany, "From bits to MOFs: deciphering surface chemistry to accelerate the clean energy transition"

4. 31st ISE Topical Meeting, 05/2022, Aachen, Germany, "Using the Interface Force Field (IFF) to Evaluate Water Structures at Metal Surfaces: Potential and Limitations"

**Posters**

1. NIC Symposium 2022, 09/2022, Jülich, Germany, "Application of the Interface Force Field (IFF) for Simulation of Water Structures at Pb(100)"

2. Electrochemistry 2022, 09/2022, Berlin, Germany, "An experimental investigation of Bi-based MOFs as a performance booster of $SnO_2$ electrocatalyst for $CO_2$ reduction"

3. 2022 EMRS Fall Meeting, 09/2022, Warsaw, Poland, "Combining Ab Initio Calculations and Experiments to Study the Ethanol Dehydrogenation Reaction on Pt-based Catalyst"

4. 31st ISE Topical Meeting, 05/2022, Aachen, Germany, "Combining Ab Initio Calculations and Experiments to Study the Ethanol Dehydrogenation Reaction on Pt-based Catalyst"

5. 2021 EMRS Fall Meeting, 09/2021, Aachen, Germany, "A DFT study of the impact of explicit and implicit solvation on the HCOOH/CO selectivity of $CO_2$ reduction reaction on Pb(100) surface"

6. 72nd Annual Meeting ISE, 08/2021, virtual, "A combined DFT/CMD study of water structure and adsorption of solvated HCOO on Pb(100) surface"

7. 748. WE-Heraeus-Seminar, 05/2021, virtual, "Ethanol dehydrogenation on supported platinum-based catalyst studied by ab initio calculations"

8. DPG-Frühjahrstagung des Fachverbandes Oberflächenphysik, 03/2021, virtual, "Water structure at Pb(100) and (111) surfaces studied with the interface force field"

9. NIC Symposium 2022, 09/2022, Jülich, Germany, "Determining the $CO_2$ Photoreduction Mechanism over $TiO_2$ Surfaces using Density Functional Theory"

**Prizes**

1. 31st ISE Topical Meeting, 05/2022, Aachen, Germany, Best Poster Presentation

2. 2021 MRS Fall Meeting, 09/2021, virtual, 2nd place Best Poster Presentation

# Appendix

# Contribution to Co-Author Publications

During my research time, I was engaged in other research projects, which are indirectly related to the main thesis topic, leading to first and co-author contributions on multiple publications, as indicated in the List of Publications. In the following I have summarized my contributions as a first and co-author for the following publications:

- **O. Cheong**, J. Pasel, J. Häusler, R. Peters, M. H. Eikerling, P. M. Kowalski, "Rationalizing the Mechanism of Ethanol Dehydrogenation on Pt/C", accepted in Surf. Sci. (2023): In this accepted manuscript, we performed a DFT study on the mechanism of ethanol dehydrogenation on Pt/C to provide computational support to our experimental colleagues from the Electrochemical Process Engineering Institute (IEK-14). Our DFT results not only align well with experimental observations, but it also enables us to propose a novel mechanism that reconciles the experimentally observed CO desorption. Here, I took on a lead role in performing adsorption energy calculations of various reaction intermediates of the ethanol deyhdrogenation reaction as well as performing NEB calculations for the extraction of activation energies of the ethanol dehydrogenation reaction on Pt/C.

- P. M. Kowalski, T. Bornhake, **O. Cheong**, N. Dohrmann, A. Liston, S. Potts, A. Shad, R. Tesch, Y. Ting, "Fundamentals of energy storage from first principles simulations: Challenges and opportunities", Front. Energy Res. 10, 1096190 (2023): In this publication I contributed to two main topics. For the

first topic I performed DFT calculations for $CO_2$ reduction on Pb(100) surface under different solvation environments, showing the significant impact of explicit solvation on $CO_2$ reduction pathways to HCOOH and CO. These preliminary results contributed to Section 4.3.1 of Chapter 4. The second topic deals with preliminary calculations of solute entropies at metal-electrolyte interfaces. We have shown the significant impact of accounting for solvation entropy effects for reactions at the electrode/electrolyte-interface.

- T. Connor, **O. Cheong**, T. Bornhake, A. C. Shad, R. Tesch, M. Sun, Z. He, A. Bukayemsky, V. Vinograd, S. C. Finkeldei, P. M. Kowalski, "Pyrochlore Compounds From Atomistic Simulations", Front. Chem. 9, 733321 (2021): In this publication I contributed to the understanding of ionic conductivity trends of different lanthanide-pyrochlore compounds. By calculating activation energy barriers associated with oxygen diffusion in various pyrochlore compounds, we were able to identify the emergence of the so-called split vacancy state as the underlying reason for the significant drop in ionic conductivity for heavier lanthanides.

- P. M. Kowalski, Z. He, **O. Cheong**, "Electrode and Electrolyte Materials From Atomistic Simulations: Properties of LixFEPO4 Electrode and Zircon-Based Ionic Conductors", Front. Energy Res. 9, 653542 (2021): In this publication I contributed to the understanding of ionic conductivity for yttria-stabilized zirconia ($YO_{1.5}$ $ZrO_2$), a commonly used solid state electrolyte. By calculating activation energy barriers associated with oxygen diffusion along the Y-Zr and Zr-Zr edge, we are capable of computing temperature and Y-content dependent ionic conductivities in agreeement with experiments.

Band / Volume 618
**Na$_5$YSi$_4$O$_{12}$-type Na$^+$ superionic conductors for solid-state batteries**
A. Yang (2023), X, 150 pp
ISBN: 978-3-95806-731-8

Band / Volume 619
**Development of industry-scalable processes for nanocrystalline
silicon oxide in silicon heterojunction solar cells**
D. Qiu (2023), 202 pp
ISBN: 978-3-95806-734-9

Band / Volume 620
**Photonic Sintering of Garnet-Based Solid-State Batteries**
W. S. Scheld (2024), XII, 153 pp
ISBN: 978-3-95806-737-0

Band / Volume 621
**Ceria-based composites for application in Oxygen transport membranes**
L. Fischer (2024), xiii, 216 pp
ISBN: 978-3-95806-739-4

Band / Volume 622
**Investigations of Air Quality Aspects with the Urban Climate Model
PALM4U**
R. Wegener, U. Javed, R. Dubus, and D. Klemp (2024), 93 pp
ISBN: 978-3-95806-741-7

Band / Volume 623
**The Chemical Budget of Radicals and Reaction Mechanisms
of the Atmospheric Oxidation of Monoterpenes Investigated
in the Atmospheric Simulation Chamber SAPHIR**
Y. S. Pang (2024), VI, 158 pp
ISBN: 978-3-95806-742-4

Band / Volume 624
**Optimizing spectral electrical impedance tomography technology for
improved subsurface characterization**
H. Wang (2024), xxix, 113 pp
ISBN: 978-3-95806-744-8

Band / Volume 625
**On a multi-spectral method for measuring aerosol properties,
suitable for operation on iagos passenger aircraft**
P. Weber (2024), ca 123 pp
ISBN: 978-3-95806-746-2

Schriften des Forschungszentrums Jülich
Reihe Energie & Umwelt / Energy & Environment

Weitere *Schriften des Verlags im Forschungszentrum Jülich* unter
http://wwwzb1.fz-juelich.de/verlagextern1/index.asp

JÜLICH
Forschungszentrum